Fall 1986

An Investigation of Overvoltage Effects on a Gas-Blown Spark Gap

Michael Steven Mazzola
Old Dominion University

AN INVESTIGATION OF OVERVOLTAGE EFFECTS ON A GAS-BLOWN SPARK GAP

by

Michael Steven Mazzola
BSEE, December 1984, Old Dominion University

A Thesis Submitted to the Faculty of
Old Dominion University in Partial Fulfillment of the
Requirements for the Degree of

MASTER OF ENGINEERING

ELECTRICAL ENGINEERING

OLD DOMINION UNIVERSITY
December 1986

Approved by:

G. Marshall Molen (Director)

Linda L. Vahala

V. Lakdawala

ABSTRACT

This experimental investigation addresses the anomalous overvoltage breakdown and subsequent recovery characteristics observed in gas-blown spark gaps. Previous investigations have reported a two-stage recovery process in self-break, pulse-charged, gas-blown spark gaps in which the spark gap recovers first to an intermediate breakdown strength before recovering to the undisturbed breakdown voltage. The recovery process has been explained in terms of two different characteristic times. The first is that required to obtain initial recovery in which the spark gap regains its intrinsic breakdown strength. The second time is that required to obtain final recovery in which the pulse-charged spark gap regains the overvoltage breakdown strength associated with the voltage increase during the statistical delay. In this interval, the spark gap operates on the "plateau" (a region of constant, highly stable breakdown strength) which has been correlated with the intrinsic breakdown strength of the pulse-charged spark gap when suitably preionized.

Both the time to initial recovery and final recovery have been found to be functions of gas velocity. Initial recovery is controlled by the gas density in the interelectrode volume. After an initial breakdown the resulting hot arc debris precludes the spark gap from exhibiting its full intrinsic strength. By convecting this debris downstream, the electrodes are cleared of the arc debris much faster

than the gas naturally recovers. As a result, this investigation has demonstrated a 10 kHz repetition rate (two-pulse) at 100% of the spark gap's intrinsic breakdown strength with a gas velocity of 360 m/s (Mach 1).

The velocity dependence of final recovery has also been studied. It is clear that final recovery occurs when the statistical delay before breakdown is no longer precluded by the effects of the first pulse. Two mechanisms have been proposed to explain the reduction of the statistical delay on the plateau. The first is thermionic emission of electrons from the hot electrodes. The second is boundary layer entrapment of easily ionized impurities. The consequences of gas flow on each mechanism have been estimated and compared to experiment. At this time, only the boundary layer impurity hypothesis correctly predicts the observed inverse relationship between the time to final recovery and the gas velocity.

ACKNOWLEDGEMENTS

I would like to thank my friend and thesis adviser, Dr. G. Marshall Molen, for his trust and guidance without which this work would not have taken place.

I would also like to thank the other members of my commitee, Dr. V. Lakdawala and Dr. L. Vahala, for their careful consideration and encouragement.

Finally, I give special thanks to my wife, Janice, for her love and understanding when I needed it most.

TABLE OF CONTENTS

TABLE OF CONTENTS - Concluded

LIST OF TABLES

LIST OF FIGURES

LIST OF FIGURES - Continued

LIST OF FIGURES - Continued

LIST OF FIGURES - Concluded

LIST OF SYMBOLS

A	gas constant [see Eq. (II-1)] or Area (as denoted in text)
B	gas constant [see Eq. (II-1)]
C	constant [see Eq. (III-12)]
C_0	modulator capacitance
C_1	switch chassis capacitance
CF	clearing factor
D_1	modulator diode stack
d	gap spacing
d_c	avalanche length
E	magnitude of the electric field
E_{dc}	maximum electric field at dc breakdown
E_{max}	maximum electric field
E_{mean}	mean electric field [see Eq. (III-2)]
f	field enhancement factor
h	convection coefficient
K	gas constant [see Eq. (III-7)]
k	thermal conduction coefficient
L	characteristic length
N	number density
N_t	total electron population
n	gas constant [see Eq. (III-7)]
p	pressure
p_{stag}	stagnation pressure

Q	total charge transfer
R	rate of rise of the voltage
R_{eff}	effective radius [see Eq. (III-4)]
r	radius
s	path length
T	temperature
T^*	normalized temperature per unit volume
T_∞	ambient temperature
t	time
t^*	boundary layer clearing factor
t_{eff}	effective time [see Eq. (III-7)]
t_f	formative delay time
t_p	characteristic purging time
t_r	time to final recovery
t_s	streamer transit time
U	free-stream gas velocity
u	local gas velocity
V	voltage
V_{bk}	pulse-charged breakdown voltage in a non-uniform electric field
$\overline{V}_{bk}$	mean value of V_{bk}
V_{dc}	dc breakdown voltage in a non-uniform electric field
V_f	formatively-delayed breakdown voltage
V_m	minimum breakdown voltage
V_o	reference voltage [see Eq. (VI-3)]
V_s	breakdown voltage in a uniform electric field

$\overline{V}_s$	mean statistically-delayed breakdown voltage
V_1	first-pulse breakdown voltage
V_2	second-pulse breakdown voltage
v	volume
$\overline{v}$	volume flow rate
w	boundary layer width
x	position along the x-axis
x_c	boundary layer thickness
y	position along the y-axis
z	position along the z-axis
α	primary ionization coefficient
β	geometry correction factor
γ	cathode emission coefficient
ΔV_f	voltage increase due to formative delay
ΔV_s	voltage increase due to statistical dispersion
Δv	volume exchanged by gas purging
η	velocity profile proportionality constant
κ	thermal diffusivity
ρ	mass density
ρ_o	ambient mass density
τ	time to initial recovery
$\overline{\tau}$	mean delay time
ω	generalized secondary coefficient

CHAPTER I

INTRODUCTION

The scope of this thesis is the identification and description of the critical parameters that govern the recovery of a high-power, gas-flow spark gap switch. An appropriate model is developed from experimental studies conducted at the Gas Flow Switch Laboratory (GFSL) at Old Dominion University. However, it should be noted that the resulting model is not based solely on data reported here, but was originally motivated by extensive work done at this facility by other researchers. A thorough review of the experimental facility was reported in a thesis by Barrett [1], and previous experimental results appear in a report by Molen and Kuhlman [2]. Before continuing with this report, however, it is appropriate to briefly examine the motivation for studying high-power spark gaps: their use in pulsed power systems.

Pulsed power systems are used to provide large power amplification while carefully controlling the temporal characteristics of an electrical pulse. Devices and applications that require mega, giga, and terawatt electrical pulses have become more common over the last few years [3]. Because the typical prime power source (dc source or ac mains) is not capable of satisfying the peak power or risetime requirements of many electrical loads, an intermediate stage is often

used to condition the electrical energy provided to such loads. The pulsed power system provides power amplification by storing energy from the prime power source over a long period of time and then releasing this energy relatively quickly. Therefore, energy is conserved, but the short delivery time results in high peak power. Oftentimes, power amplification is accompanied by careful control of the temporal "shape" of the electrical pulse so that the load receives high peak currents and voltages that have been conditioned to the requirements of that load.

Typical applications that use this technology fall into several categories. First, there are a variety of radiation sources, including lasers, x-ray sources, electromagnetic pulse (EMP) generators, and microwave tubes. Another important area is in particle-beam accelerator technology. Many linear and closed-loop accelerator facilities rely on pulsed power devices to drive the essential components of the facility, such as klystrons (a microwave tube), electrostatic accelerating cavities, and particle beam diodes. Weapons, such as rail guns and directed energy systems (lasers, particle beam accelerators), have significant pulsed power needs as well. Finally, one should note that pulsed power applications are not confined to massive machines; for example, the flash lamps that pump small solid state lasers can be considered as a pulsed power load.

The typical pulsed power system is illustrated in the block diagram shown in Fig. I-1. The diagram represents a voltage-fed, line-type pulser in which a low-power, prime source charges an energy storage element over a lengthy period of time. When sufficiently charged, a switch between the energy storage element and the load is closed, thus

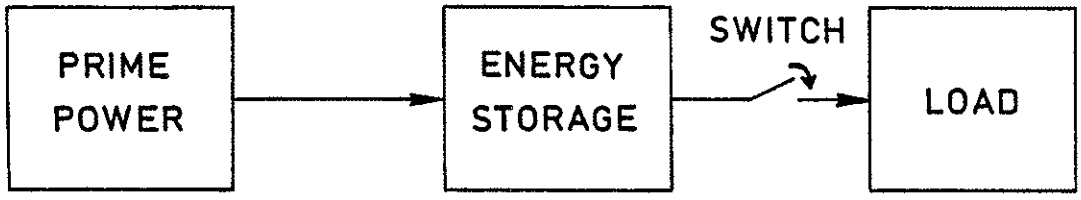

Fig. I-1 Block diagram of a voltage-fed, line-type pulsed power system.

discharging the stored energy into the load. Often a transmission line is used to combine the energy storage system with the power conditioning system, hence the name line-type pulser. The transmission line provides power conditioning by passively controlling the temporal shape of the pulse.

In a line-type pulser, the switch is required to function as an "ideal" switch (e.g., zero "on" resistance, infinite "off" resistance) because the pulse shape is controlled by the circuit inductance, capacitance, and resistance. This is in contrast to the other generic type of system, called the hard-tube pulser, in which the switch controls the temporal shape of the pulse by varying its conductance. In a hard-tube pulser, no other circuit component, besides the load, plays an active role in the resulting pulse shape. While these two different types of pulsers have completely different switch requirements, perhaps the preponderance of attention is devoted to switches used in line-type pulsers because they are most often used in pulsed power applications. Regardless of the pulser type, however, the critical component of most pulsed power systems remains the switch.

Switch Characteristics

The switch requirements are demanding. In general, it must hold off large potentials during the energy storage phase and conduct substantial currents during the discharge phase. Many switches have been designed to meet these two basic requirements; however, other switch characteristics (e.g., forward voltage drop, current polarity restrictions, and repetition rate) tend to limit switches to certain applications. A very important consideration for a switch used in a

pulsed power system is its repetition rate, since the repetition rate governs the maximum average power that may be output.

The repetition rate is the number of pulses per unit of time and is often specified in pulses per second (pps) or hertz. If the device is producing a continuous stream of pulses, then the repetition rate is the inverse of the time between pulses. However, switches are often operated in a burst mode. Burst mode consists of a group of two or more pulses produced over a short time interval, an interval of no pulses, and then another group of pulses. Each group is referred to as a "burst" of pulses. This distinction is illustrated in Fig. I-2. The repetition rate of the switch is the inverse of the time between the pulses forming any one burst, while the burst repetition rate is the inverse of the time between bursts.

The maximum repetition rate of the switch is governed by the recovery time of the switch. Switch recovery occurs when the switch no longer freely conducts to the extent that it can once again hold off large potential voltages. Numerous factors govern this transition from a good conductor back to a good insulator. In low-pressure gas switches, it may be deionization of the conducting plasma, but in high pressure switches it is a combination of deionization and cooling of the heated gas, with cooling being the dominant factor. In practical terms, recovery is usually defined as the ratio of the voltage amplitude of a second pulse with respect to a preceding initial pulse. The switch recovery time is the minimum time required between these two pulses so that the switch is able to withstand the second pulse at

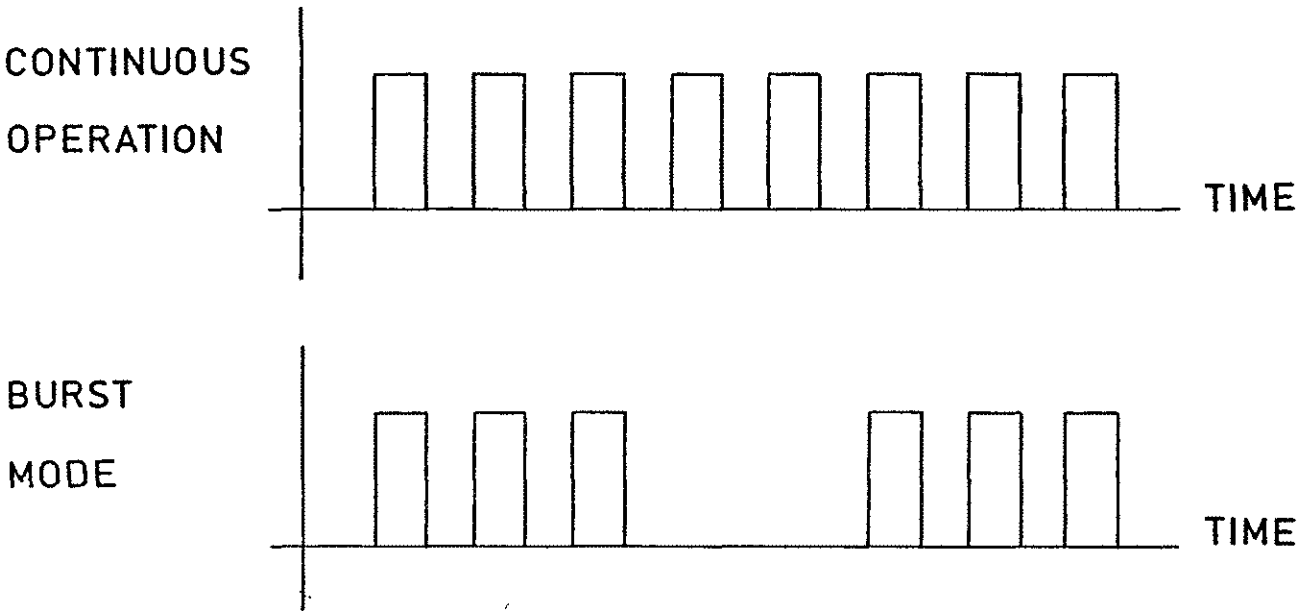

Fig. I-2 Continuous operation versus burst mode.

nearly 100% of the voltage amplitude of the initial pulse. These definitions of switch recovery and recovery time are illustrated in Fig. I-3.

Of the many switches designed for pulsed power applications, some of the more common include the ignitron which is a mercury-filled metal vapor switch, the thyratron, the gas-filled triode, and, of late, semiconductor switches principally represented by thyristors. However, for the highest power applications the gas spark gap is still the dominant switch type. The gas spark gap generally consists of an arrangement of metallic electrodes separated by a space (the "gap") which is filled with a gas. This gas is capable of exhibiting high dielectric strength before it is "broken down" by the high electric fields and is transformed into an excellent conductor of electrical current. The breakdown usually takes the form of a transient arc, called a spark, which spans the gap between the electrodes and allows current to flow through the spark gap switch and hence through the external circuit. While spark gaps can be operated over a wide range of gas pressures, for the purposes of this thesis a high-pressure spark gap switch is defined as one that operates at pressures significantly above the Paschen minimum [4].

Spark Gap Switching

The gas spark gap has many advantages compared to its available competition. These advantages include ruggedness and economy resulting from their simplicity of construction, wide operating ranges of voltages and currents reaching into the megavolts and megaamperes for high-pressure spark gaps, reasonably good triggering characteristics, nanosecond current risetimes, and bipolar current conduction. However,

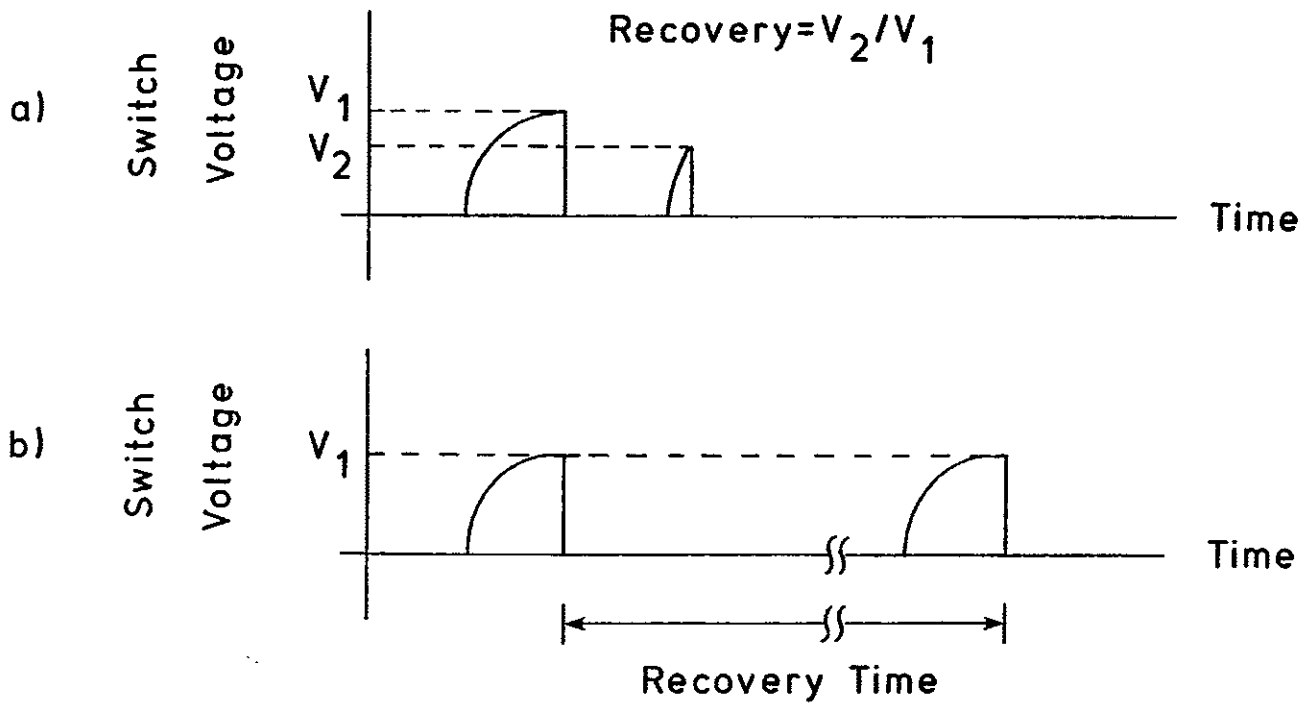

Fig. I-3 An illustration of a) the partial recovery of a switch and b) the recovery time.

the disadvantages of the spark gap have resulted in its replacement in many of its former low and medium power applications.

Two of the limiting features of the spark gap are its repetition rate and its lifetime. Pulsed power technology has progressed to a point where high repetition rate is a critical design specification. High-pressure spark gap switches suffer from low pulsed repetition rates primarily because of the lengthy time required for the thermal energy dumped into the gas by the spark to be removed. The use of conventional spark gaps for high power switching at repetition rates greater than 100 Hz is infrequent, 10 Hz or less being more common [5].

Compounding the repetition rate problem is the relatively short life exhibited by the typical spark gap. One important variable controlling the lifetime of a spark gap is the total charge transfer, Q, through the gap [5]. The lifetimes of high-power, large-Q spark gaps seldom exceed 10^5 shots [6], but smaller, low-Q spark gaps can last for 10^7 shots or more. Even so, 10^7 shots can be reached very quickly in a high-repetition-rate, continuously-operated mode, indicating that lifetimes on the order of 10^8 shots and above are needed.

On the other hand, the advantages of the gas spark gap suggest that it is desirable and, in some cases, necessary to use such switches. There have been various methods proposed for overcoming some of the disadvantages of spark gap switching. For improved triggering and cooling of electrodes, low-velocity gas replenishment is already used [5]. By upgrading the concept of gas replenishment to high-velocity gas replacement, referred to as gas flow in this thesis, it is proposed that a significant improvement in spark gap recovery may

be realized. The difference between gas replenishment and gas replacement is in their respective goals. Gas replenishment seeks to remove the unwanted chemical byproducts formed in the gas during an arc. This removal, and the resulting replenishment of the spark gap volume with fresh gas, occurs long after the spark gap has recovered. Gas replacement seeks to remove the heated arc debris on a time scale faster than normal free recovery in order to increase the repetition rate of the spark gap.

The reduction of the dielectric strength of spark gaps at high repetition rates is widely believed to be caused by the decreased density of the interelectrode gas after the occurrence of a spark in the gap. A gas flow switch removes the bulk of this unwanted thermal energy downstream and out of the interelectrode volume by maintaining a continuous stream of high velocity gas through the electrode region. In such a way, it is believed that a 10 kHz repetition rate can be achieved, which is at least an order of magnitude above the state of the art.

The chief limitation of gas flow switching is the added expense and complexity of the equipment required to produce the high-velocity gas flow. In addition, the significant mechanical energy required to propel the gas at high velocity could reduce the intrinsic efficiency of the spark gap significantly. However, it seems likely that a clear trade-off between added expense, size, and efficiency may be compatible with repetition rate, thus allowing gas flow switching to be economical within a certain range of specifications.

The principal applications of gas flow switching are high peak power, high repetition rate pulsed power modulators for particle beam accelerators and lasers. Improvement in the repetition rate of such accelerators and lasers is important for the success of inertial confinement fusion. In addition, repetition rate has been a limiting factor in such diverse applications as pulsed radars, directed energy weapons, and linear accelerators for scientific research. Clearly, an order of magnitude improvement in the repetition rate of such a high power switch may advance these technologies significantly.

Scope and Organization

This thesis reports on the successful operation of a gas flow switch capable of a 10 kHz repetition rate and presents a two-stage model of gas flow spark gap recovery that explains the anomalous "plateau" effect observed in previous experiments at the Gas Flow Switch Laboratory [2]. The model augments previous work done at Old Dominion University.

A discussion of the basic theory of breakdown in spark gaps as well as a review of applicable past work on pulsed, self-breakdown phenomena and spark gap recovery will be presented in Chapter II. The self-breakdown and recovery process for pulse charged gas flow switches will be more thoroughly discussed in Chapter III, where the previously mentioned model of gas flow recovery will be presented. The experimental apparatus and methods will be described in Chapter IV. This description will include an overview of the Gas Flow Switch Laboratory at Old Dominion University as well as an outline of the experiments used to support the proposed model of gas flow recovery. Chapter V will report experimental results covering a series of gas

flow recovery experiments spanning a large velocity range. An interpretation of these results will be offered in Chapter VI to show how the results relate to and support the proposed recovery model. Finally, Chapter VII will summarize the important conclusions of this work and how they relate to the study of gas flow switching.

CHAPTER II

REVIEW OF BREAKDOWN AND RECOVERY PHENOMENA

High-pressure gas spark gaps have been widely used in pulsed power applications. With increasing requirements on repetition rate, the need to improve the recovery of sparks gaps has become important. It is widely known that the repetition rate of spark gap switches can be improved by use of gas flow to "flush" the electrode region of arc debris [6]. In a review of gas blown switches by Kuhlman [7], it was found that most such switches were designed for a specific application with little attention to optimizing or even identifying the important parameters controlling the performance of the switch.

Nevertheless, some interesting models of the thermal and electrical recovery of gas blown switches have been developed, as will be reported in this chapter. In addition, descriptions of the typical geometries used in gas blown switches and a discussion of the more successful examples of these geometries from previous work will be presented. But first, it is appropriate to review past and current work on spark gap breakdown so that the foundations for a model of spark gap recovery can be established.

Breakdown Models

The first model of electrical breakdown in gases was developed by Townsend at the beginning of the Twentieth century [8] and is

appropriately called the Townsend breakdown theory. This theory recognizes that charged particles (electrons) introduced into a gaseous region containing a sufficiently strong electric field can multiply through collisions with neutral gas molecules. The multiplication is exponential in nature because newly liberated electrons may themselves go on to liberate others so that an ever increasing swarm or avalanche is formed. However, loss mechanisms tend to remove these electrons from the gap. In order to sustain the avalanche process the lost electrons must be replaced, either by gas and electrode mechanisms or by external excitation (e.g., UV illumination). There are secondary processes that result from the primary electron avalanche, including collisional ionization by positive ions, electron emission by positive ion bombardment of the cathode, photoemission of electrons from the cathode, and photoionization in the gas volume. Under the proper conditions of gap spacing, electric field, and gas density these secondary mechanisms may be significant enough that electron losses are replaced and a self-sustaining glow or arc discharge formed. Such an event is called a breakdown because the gas has transitioned from a dielectric to a conductor.

In a uniform electric field, the primary avalanche process is described by the first Townsend coefficient, denoted as α, that gives the average number of ionizations per incident electron per unit length. The ionization process is a very sensitive function of the electron energy distribution as well as the density of the background gas because non-elastic, electron-neutral collisions produce the bulk of the electron-ion pairs formed. Since the electron energy comes from the applied electric field and the number of neutrals is described by

their number density N, then α is a strong function of the reduced electric field strength, E/N.

The secondary process is described by a generalized secondary coefficient, ω/α, which is formed of coefficients describing the various secondary processes. The generalized coefficient is often simplified by assuming that a single mechanism, such as positive ion bombardment of the cathode, dominates the others in producing secondary electrons. Since electron emission from ion bombardment is often dominant, ω/α is reduced to a single coefficient, γ, which gives the average number of electrons liberated by an ion incident on the cathode. The lower the work function of the cathode material, the greater the efficiency of electron emission from the incident ion flux. Thus γ is a function of the cathode material.

Together, α and γ can be used to generate a breakdown criterion which leads to an expression for the breakdown voltage in a gas subjected to a uniform field [8]. As a result, the Townsend avalanche theory was quickly used to explain the experimentally determined Paschen law, which states that the breakdown voltage is only a function of the product of the pressure, p, and the gap spacing, d, for a given gas and cathode material. It can be shown that if the dominant secondary mechanism is cathode bombardment by positive ions, then the breakdown voltage, V_s, of the gap can be written explicitly as a function of pd [4]

$$V_s = Bpd/\ln[Apd/\ln(1/\gamma)] \qquad \text{(II-1)}$$

where A and B are gas constants and γ is the secondary coefficient previously described.

Thus, the Townsend avalanche theory successfully explained a physical law that preceded it. Furthermore, the Paschen curve, a curve relating the breakdown voltage to pd, was shown to go through a minimum V_s for a well defined pd. This minimum is a definite function of the cathode material [9], in accordance with the importance of the cathode secondary processes. While the Townsend breakdown theory was successful in explaining observed breakdown phenomena at lower values of pd (< 200 torr•cm), problems occurred when experiments exceeded this limit.

As pd was increased above 200 torr•cm, and non-uniform electric fields were considered, substantial deviations from initial expectations occurred. First, the formative time lag (the time required for breakdown to occur) was oftentimes orders of magnitude shorter than what would be expected from the relatively slow movement of positive ions. In fact, breakdown was sometimes measured to occur so fast that even the highly mobile electrons would be unable to cross the gap [8]. This, coupled with the seeming lack of cathode participation in the breakdown process [8], suggested that breakdown could occur in a fundamentally different manner than that predicted by the Townsend theory. Therefore, several researchers proposed a new mechanism generally called the streamer theory.

The streamer theory's major premise is that at higher values of pd large concentrations of positive space charge may accumulate which distort the externally applied electric field and cause significant departures from the Townsend mechanism. The omission of space charge

buildup was a major discrepancy in the original Townsend theory before the theory was generalized by later researchers. In the typical formulation of the streamer theory, the process begins when an avalanche propagating across the gap goes "critical" [10], that is, its electron population reaches a critical value of about 10^9 electrons. This value is determined by one of two different criterions. The Raether criterion [9] requires that the critical density be determined by the avalanche head size necessary for self-propagation of the streamer, as determined by experimental measurements of the conditions in the gap when breakdown occurs. It has been found that the product of α and the length of the avalanche, d_c, when the streamer forms is a constant of about 20 [9]. The critical density can be calculated from this experimentally determined constant if it is assumed that the avalanche forms from a single electron, which yields

$$\exp(\alpha d_c) = N_t \cong 10^9 \quad . \qquad \text{(II-2)}$$

On the other hand, Meek suggested that the space charge formed by the primary avalanche becomes critical when the radial electric field due to that residual charge is on the order of the applied electric field [10]. Since the streamer theory depends on the effect of space charge fields on local values of α (a strong function of E/N), the Meek criterion is advantageous because it describes the streamer initiation in terms of a field distortion factor. The point where the space charge field successfully competes with the applied field, arbitrarily assumed to be when they are equal, can be selected to give a better fit with experimental data [9].

Coupled with the formation of a critical or primary avalanche is the emission of photons from the excited molecules invariably created by the passage of the avalanche head. The photons escape the avalanche head in all directions and are absorbed by the gas, where at least some photoionizations occur. The electrons liberated by the photons create new avalanches in the space charge enhanced electric field. These auxiliary avalanches "feed" into the channel created by the primary avalanche, increasing the level of conductivity of the channel and extending it toward the cathode (positive streamers) and the anode (negative streamers) [10]. Eventually, auxiliary avalanches created by photoelectrons cause the highly conductive channel to span the gap between the electrodes, thus producing breakdown. Because of the luminous and filamentary nature of this process, it is called a streamer breakdown.

Fast formative times are a natural consequence of streamer breakdown because of the use of radiation to produce new avalanches and the increased electron amplification caused by the enhanced electric field, thus agreeing well with experimental measurements. In addition, cathode processes are not needed to cause breakdown after the primary avalanche goes critical because auxiliary avalanches are created in the gas by photoionization, rather than at the cathode by Townsend secondary processes. Finally, the theoretical prediction that streamers can be initiated virtually anywhere in the gap seems to corroborate many streak photographs, which show a luminous filament initiated in the gap region and then quickly moving toward both electrodes, where breakdown then occurs [9].

The streamer theory has not gained universal acceptance, however. Many reseachers consider the Townsend mechanism to remain valid, even at high pd, and claim that experimental deviations from the Townsend mechanism are based in technique not physics. Improvements in experimental measurements and the inclusion of space charge effects in models of Townsend breakdown lead to the elimination of some of the previous discrepancies [11]. In addition, considerable disagreement exists in the interpretation of the experimental evidence, especially streak photographs that record the temporal development of breakdown [8]. Nevertheless, there seems to be an acceptance of the proposal that the Townsend mechanism is valid at low and medium values of pd and overvoltages of less than 20%, while the streamer theory applies for overvoltages greater than 20% [11]. An overdue attempt to unify these two competing theories has been made by Kunhardt and Byszewski [12] in which they suggest that fast "runaway" electrons produce the secondary volume ionization rather than photoionization.

Empirical Models

There is a third school of thought, apart from the controversy over breakdown theory. A group of researchers has quietly pursued empirical studies designed to make the effort of engineering large, high-power devices less costly and more successful. The goal has been to generate empirical relations based on representative data. These empirical relations are used to estimate breakdown voltages, current risetimes, and losses in spark gap switches as well as the dc and impulse dielectric strength of power distribution equipment. The need for this kind of work is clear because those studying breakdown physics have not generated models that are easily transportable to practical switch

parameters, such as high electric fields, unsymmetric geometries, and a variety of gases (e.g., SF_6, air, N_2, etc.).

A common example of this latter work is the sphere gap standards that allow the measurement of high voltages to within 3% accuracy. The standards are based on the breakdown voltage between spheres of specified radius and gap spacing measured during controlled tests at a variety of pressures, temperatures, and humidities. The standard breakdown voltages can be found in either equation form (Ref. [9], p. 540) or tabular form (Ref. [4], p. 586) for line-frequency or impulse voltages. However, the sphere gap standards are not of great value in switch design because of the prescribed geometry.

C. Martin and colleagues at the Atomic Weapons Research Establishment (AWRE) in Aldermaston, England have developed equations for dc breakdown [13] that are quite accurate and include geometry considerations such as field enhancement. In addition, Martin has produced equations that allow the resistance and the inductance of the arc to be estimated, as well as the breakdown formation time of the spark gap. All of these equations use variables that are typically within the grasp of the engineer: pressure, electrode radius, gap spacing, breakdown field and the like. The equations are all reasonably accurate if applied to the appropriate conditions.

Unfortunately, the conditions for which the empirical relations hold are not always known without a physical understanding of the origin of the equations. In an effort to correct this fundamental problem, theorists have either attempted to derive, as special cases, the empirical equations from known models or to develop models that give physical significance to the equations. The work by Carrara and

Thione [14] is an example of the latter that has relevance to this thesis. They proposed that the impulse breakdown voltage of various rod-plane gap geometries can be predicted by knowing the minimum breakdown voltage of specific sphere-plane gaps, V_m, and the amount of time it takes for a leader to traverse the gap (formative time, t_f). According to their model, the impulse breakdown voltage can be expressed as

$$V_{bk} = V_m + \Delta V_f + \Delta V_s \qquad \text{(II-3)}$$

where ΔV_f is the voltage increase during the formative delay and ΔV_s is the voltage increase due to the statistical variation of V_m and ΔV_f. Both t_f and ΔV_s are measured experimentally, and good agreement is reported.

A more recent and very similar model was suggested by T. Martin in 1985 [15]. In this model, a streamer is launched at or near the time an impulse voltage reaches the dc breakdown strength of the gap. The streamer transit time determines the amount the voltage across the gap increases before the gap breaks down, similar to Eq. (II-3) above. However, the streamer transit time is calculated from a modified J. C. Martin equation so that the dependence of the transit time on overvoltage, pressure, gas, and gap spacing may be taken into account. In addition, prefire probabilities and trigatron characteristics can be predicted from additional information, making the model a truly useful engineering tool for designing high-power spark gaps. While T. Martin has only presented results based on SF_6, the transportability of the streamer transit equation to other gases is known, and it will be used

to explain breakdown data presented in Chapter III for air and nitrogen.

Gas Blown Spark Gaps

In this section spark gap recovery will be discussed as well as the resulting models that have been put forth to explain this process. In addition, the generic forms of gas blown switches will be reviewed along with examples of their typical performance.

Recovery Models

A substantial amount of work has been done to measure the recovery of spark gaps without gas flow, often called free recovery. Typical recovery times for spark gap switches fall in the range of 1 ms to 10 ms, depending on the geometry of the gap and the gas [2], [16]; however, this is an overestimate of the actual continuous repetition rate possible with such a switch because of the cumulative effects of the high average power dissipated in the switch. As a result, there is wide spread agreement that high-pressure switch recovery is ultimately controlled by the temperature decay of the electrodes and the gas to near initial values. It is assumed that deionization processes generally occur at a much faster rate. In other words, the unrecovered spark gap is equivalent to an undisturbed gap operated at a lower gas density (because of the higher local gas temperature). Thus, Paschen's law indicates the gap will breakdown at a lower voltage than with the initial pulse. This model requires that the gap has deionized to such a degree that it may once again undergo the complete breakdown process. At the higher pressures (above the Paschen minimum) this is almost always the case [16].

Consequently, the key to fast recovery time is the ability to rapidly remove the thermal energy deposited in the gas and the electrodes by the previous arc. Attempts at modeling the heat transfer characteristics of spark gaps have been made, both analytically and numerically. An example is the work by Edels, et al. [17], who presented simplified heat transfer calculations that included the electrodes and the surrounding gas regions. A unique feature of this work was that impressive gas flow recovery data was presented, including recovery times of less than 200 μs with gas velocities of 110 m/s; however, the current was rather modest (less than 50 A). Unfortunately, the calculations did not consider the convection of the arc debris in detail, but they did seem to explain the relative shape of the recovery curves, especially the fast increase of the breakdown voltage that tapered off to a slow asymptotic approach to the full dielectric strength of the gap. The calculations indicated that the differences in the slopes of the recovery curve were apparently caused by a difference in the cooling rates of the gas and the electrodes.

More recent attempts to model gas flow recovery have invoked clearing factors, which have various definitions but often takes the form of [5]

$$CF = \Delta v/v \qquad \text{(II-4)}$$

in which Δv is the gas volume exchanged between pulses and v is the total switch volume. Ideally, a specific spark gap should achieve full recovery for a unique value of CF; however, as Kuhlman and Molen pointed out [18], the clearing factor is often misleading because it neglects the influence of turbulence and boundary layers on gas flow recovery.

In the same paper, Kuhlman and Molen proposed a new model that is capable of explaining the observations reported by several authors [17], [19], [20] in which the second arc in a two-pulse burst often does not follow in the same channel as the first, even if the first channel is the least distance between the electrodes. The model proposes that full recovery does not occur until the integrated incremental product of density and distance over all possible paths is greater than the product of the ambient density and the gap spacing. In mathematical form this condition is expressed as

$$\int_C \rho(s) \cdot ds > \rho_0 d \quad . \qquad \text{(II-5)}$$

This criterion is only quantitatively useful in a uniform electric field because it implies that breakdown is spatially dependent only on density. In the more general case of non-uniform fields, this criterion is not correct. However, it could be a useful and simple way of predicting behaviour in nearly uniform gas-blown spark gaps, such as those using the slowly converging-diverging nozzle electrode geometry.

The interpretation of this model was originally clouded by anomalies in both gas flow and static recovery data. The anomaly was called the "plateau" because the spark gap, under pulsed conditions, would recover first to an intermediate breakdown voltage which was less than the first pulse breakdown strength of the gap. Considerably later in time, the gap would recover to the full overvoltage strength exhibited by the first pulse. It was suggested at the time by Molen, et al. [21] and Moran and Hairfield [20] that the gap was initially recovering to the static or dc breakdown voltage and later returned to

the statistically delayed overvoltage regime. As the results of this thesis will attempt to show, this explanation is for the most part accurate.

Switch Geometries

There are two primary gas flow geometries frequently used in spark gaps: coaxial and linear. The first to be discussed is the coaxial geometry, which most often uses a cylindrical electrode configuration in which the gas is injected radially into the gap region from outside and is exhausted axially through holes in the center of each electrode. An important consideration when using this geometry is the nature of the flow in the gap, that is, whether the flow is directed radially into the electrode region only or is given an angular component as well. The former is called straight-line flow and is illustrated in Fig. II-1, while Fig. II-2 illustrates the latter which is called vortex flow.

Straight-line flow has the advantage that higher gas velocities can be reached for less blower power; however, arc debris caught in the slower boundary layers can lessen this advantage. The turbulent "swirl" of vortex flow will sweep out the boundary layers much more quickly and enhance the mixing and cooling process, but the lower velocities typically obtained may ultimately limit this techinque to medium and low repetition rates.

The supersonic, straight-line flow, coaxial spark gap reported by Rabe [22] is a good example of this type. The switch is very similar to the general illustration shown in Fig. II-1. It is reported that typical gas velocities are in the range of Mach 1.5 (540 m/s) and

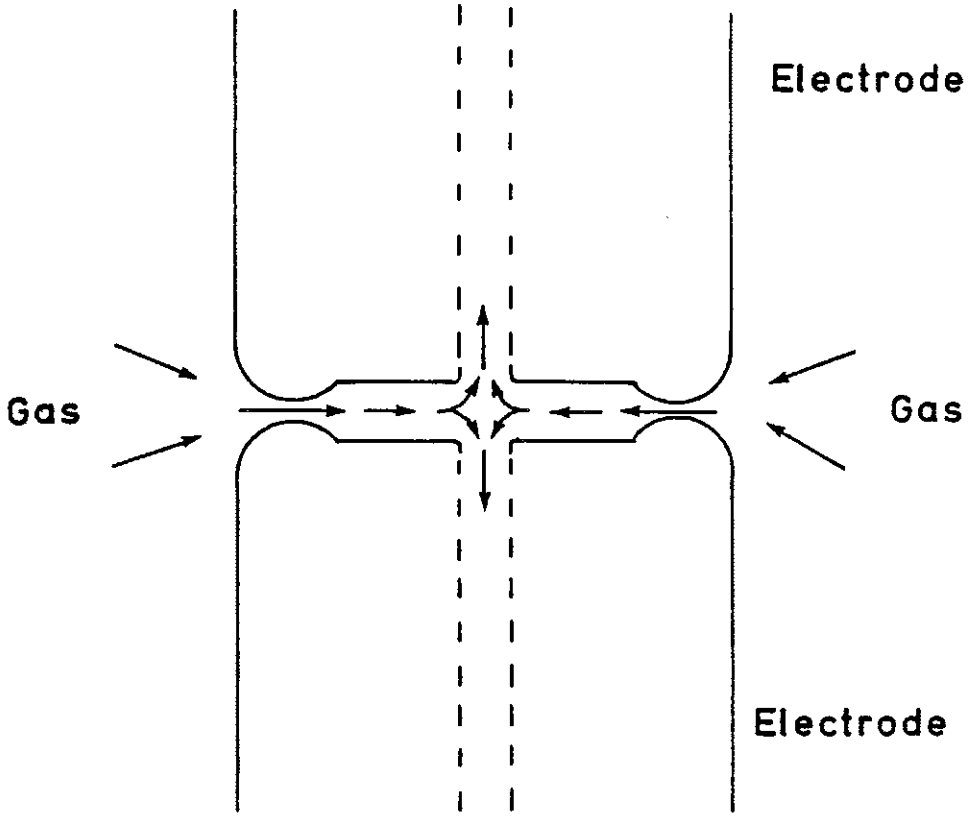

Fig. II-1 Straight-line flow in a coaxial geometry.

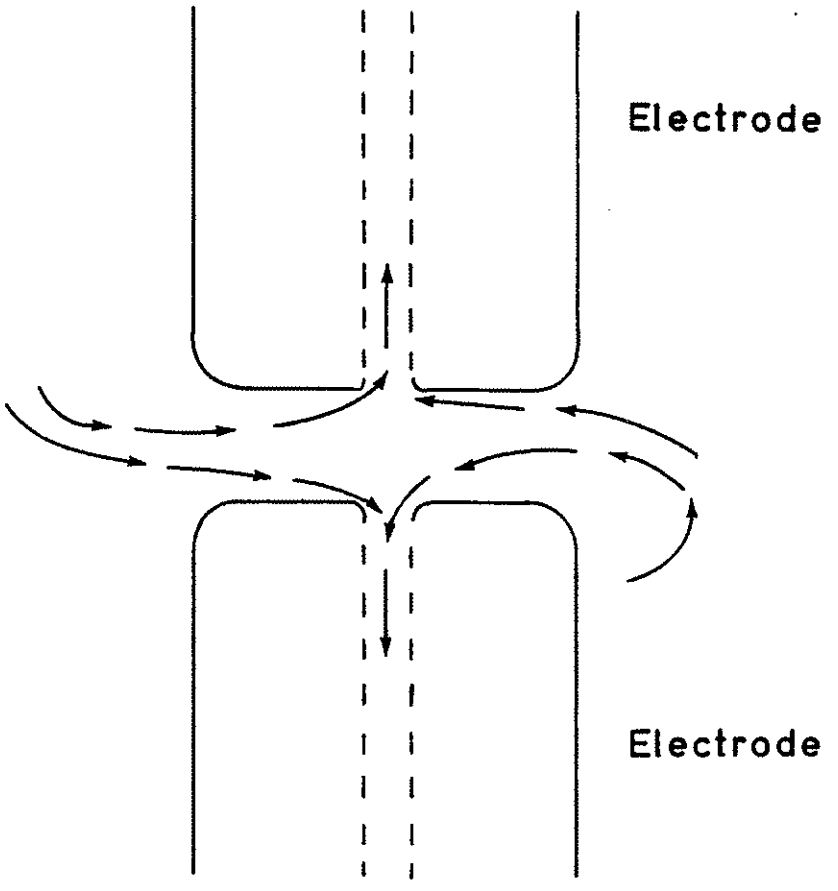

Fig. II-2 Turbulent vortex flow in a coaxial geometry.

recovery occurs in approximately 350 μs at 20 kV, but repetition rates of 500 Hz or less are claimed [22].

A higher power switch using an altered geometry was built by Faltens, et al. [23]. The switch consists of a cylindrical anode centered inside of an annular cathode in a coaxial configuration. Gas enters through an annular chamber on the front of the gap, is directed down the switch axis between the electrodes, and exits through an annular chamber on the opposite end of the switch. An impressive repetition rate of 1 kHz at 220 kV and 42 kA in 5 pulse bursts was achieved with estimated gas velocities of 50 m/s. The use of an SF_6-N_2 mixture may have also improved the recovery rate.

A turbulence-generating, vortex-flow switch built at Avco Everett Research Laboratory was used to replace a bank of thyratrons in an existing pulsed power modulator [24]. This is a departure from the trend to use thyratrons in place of spark gaps in many high repetition rate applications. The switch is reportedly capable of 150 kV operation at an unspecified repetition rate above 200 Hz. The gas is injected into the switch by circular groups of nozzles at the outer ends that give the flow an angular velocity as well as a radial component. As a result the flow swirls into the gap region formed by cylindrically symmetric electrodes, as shown in Fig. II-2, and is exhausted through holes in the electrodes.

The other major gas flow switch geometry is the linear type. In this geometry gas flow is directed along an axis transverse to the electrode axis. Thus the gas enters the electrode region on one side and exists on the other. Typically, the gas flow is first directed through a converging-diverging nozzle in order to increase the gas

velocity to the desired value. Oftentimes, the electrodes are included in the converging-diverging nozzle itself, as illustrated in Fig. II-3, because the maximum velocity occurs in this region.

One advantage of the linear geometry is the improved aerodynamic structure of the switch that makes mating to a closed-circuit gas circulation system easier. Good aerodynamic coupling to the remainder of the wind tunnel, particularly the diffuser sections, is critical for efficient gas flow. In addition, spark gap and flow axes are perpendicular so that flow and optical diagnostics can be performed along an axis normal to the plane containing the gap and flow axes. This geometry has the disadvantage of not being as compact as the coaxial switch and frequently has a correspondingly larger inductance. In addition, it may be necessary to use electrode shapes that are aerodynamically acceptable, but not electrically optimum. However, scaling the gas velocity to higher values (corresponding to higher repetition rates) is probably more likely to be achieved with a linear geometry.

An example of the linear geometry is the rail gap switch built at Spectra Technology (formerly Mathematical Sciences Northwest, Inc.) [25]. The electrodes are contained in a 2-D converging-diverging nozzle connected to a closed circuit blower. The cathode is flush with the nozzle walls, but the anode has a curious wing shape and extends into the nozzle throat to form a 0.5 cm gap. With flow speeds ranging from 35 m/s to 67 m/s, a 1250 Hz continuous repetition rate was reported. The switch could hold off voltages as great as 60 kV in N_2 and rare gas laser mixtures.

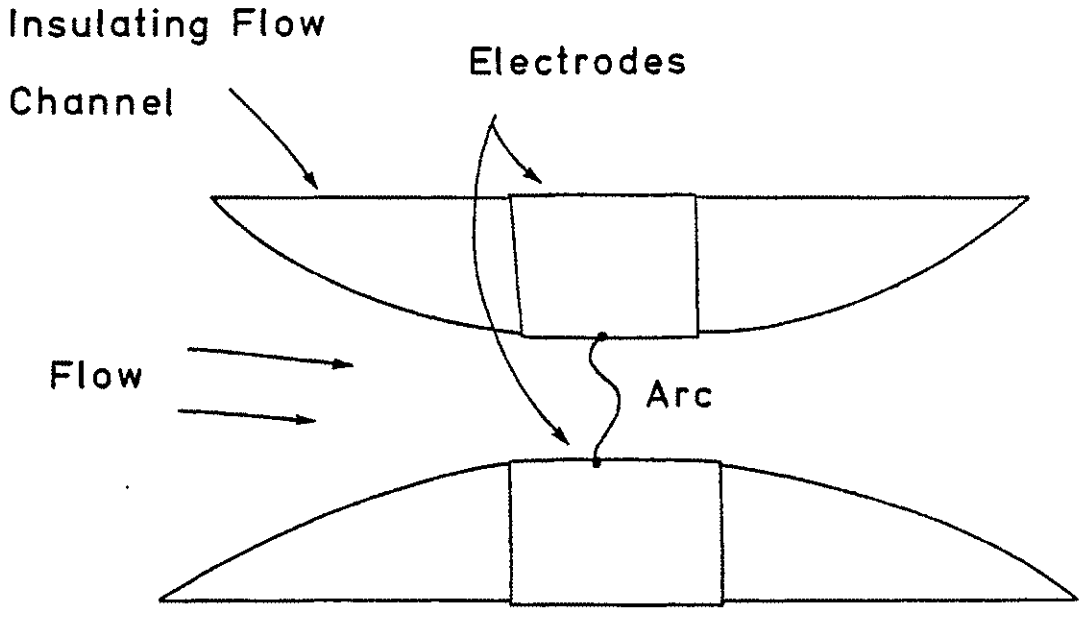

Fig. II-3 Gas flow in a linear geometry switch.

Finally, the Gas Flow Switch Laboratory at Old Dominion University uses linear configurations in which the electrodes and the nozzle are separate, although experiments in the past have used electrode-nozzle combinations [19]. The facility is capable of generating subsonic and supersonic gas flow with switches capable of up to 250 kV, 50 kA operation. A considerable body of results from the laboratory has already been published [2], [18], [21], [26], and this thesis will present new data to support a model developed with the help of this previous work.

CHAPTER III

BREAKDOWN AND RECOVERY MECHANISMS

Anomalous recovery results, in which a "plateau" is observed such that at lower pressures the gap recovers in two distinct phases, has been reported in previous investigations at the Gas Flow Switch Laboratory [21], as well as in other investigations [20], [25]. This two-stage recovery of a spark gap can be explained by correlating recovery data with a more exact description of the breakdown process. It is appropriate, then, to begin this chapter by reporting and interpreting the breakdown characteristics of the spark gaps used in this investigation.

DC Spark Gap Breakdown

When a slowly increasing voltage is applied to a pair of large flat electrodes, the theory of uniform electric field breakdown can give a good prediction of the resulting static or dc breakdown voltage. Quite often, Paschen's law may be used, as quantitatively described by Eq. (II-1), to calculate the breakdown voltage. In the equation

$$V_s = Bpd/\ln[Apd/\ln(1/\gamma)] \qquad \text{(II-1)}$$

the constants A, B, and γ can be found in the literature for specific

gases and cathode materials; however, better results are often obtained by modifying the constants to fit a representative set of data. To insure that acceptable results will be obtained, the constants found empirically may be checked against those reported in the literature for reasonable agreement.

When non-uniform electrodes are used, as is often the case in application, Eq. (II-1) is no longer valid. One approach to calculating the breakdown voltage for such geometries is to assume that the maximum electric field, E_{max}, in the gap controls the breakdown process. Since E_{max} occurs near the electrodes in typical spark gap geometries, the assumption that breakdown begins in this region of high field intensity near the electrodes is reasonable. When E_{max} exceeds a critical value, the gap then breaks down.

The dc voltage across the non-uniform gap at breakdown, V_{dc}, can be calculated by introducing a field enhancement factor that relates E_{max} to the mean electric field. The field enhancement factor is defined as

$$f = E_{max}/E_{mean} \qquad \text{(III-1)}$$

while the mean electric field is defined as

$$E_{mean} = V/d \quad . \qquad \text{(III-2)}$$

Since the value of E_{max} at breakdown is equal to some critical value of electric field called E_{dc}, then V_{dc} can be expressed as

$$V_{dc} = E_{dc} \cdot d/f \quad . \qquad \text{(III-3)}$$

The field enhancement factor is calculated in terms of geometric parameters alone by using electrostatics, and for simple geometries an analytical solution is possible.

The critical field strength is a function of electrode geometry [4]. C. Martin has developed an empirical relation that gives the critical breakdown field strength as a function of pressure and geometry in air or N_2 for sphere-sphere gaps [27]. The equation gives the field in kV/cm as follows

$$E_{dc} = 24.5\ p + 6.7\ \beta \sqrt{p/R_{eff}} \qquad \text{(III-4)}$$

where p is the pressure in atmospheres, β is a geometry correction factor, and R_{eff} is 0.115 r (r = electrode radius in centimeters) for spheres. The geometry correction factor is a function of d/r and is shown in Fig. III-1. In order to make dc breakdown field calculations using Eq. (III-4), the electrode geometry will now be considered.

Two electrode configurations were used in the work reported here, they have been given the names "nipple-rod" electrodes and "hemispherical" electrodes. The nipple-rod electrodes are illustrated in Fig. III-2(a). The actual breakdown occurs between the relatively small radius tips that form the gap spacing. The hemispherical electrodes are illustrated in Fig. III-2(b). The field distribution between these electrodes is a function of the entire spherically shaped tips.

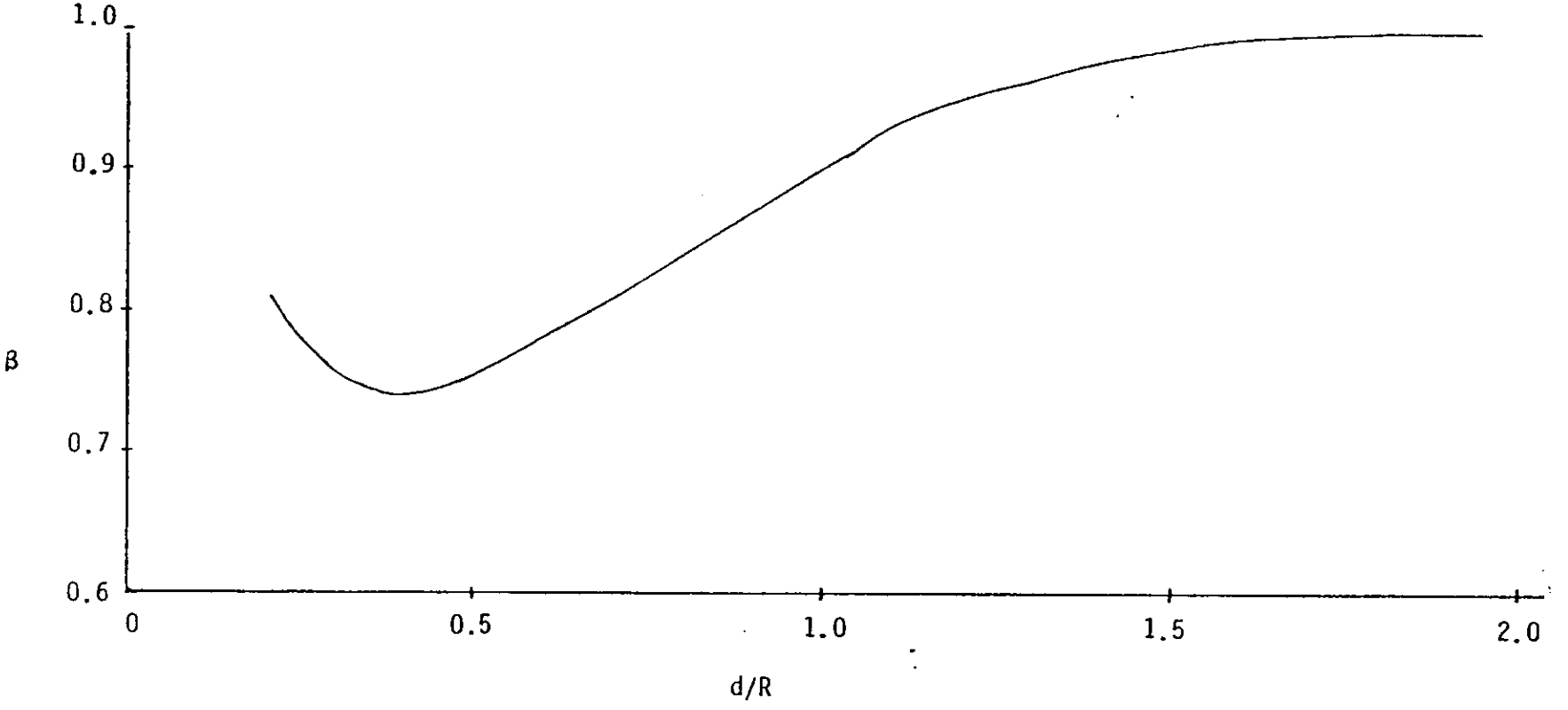

Fig. III-1 Correction curve for calculating dc breakdown (from Ref. [27]).

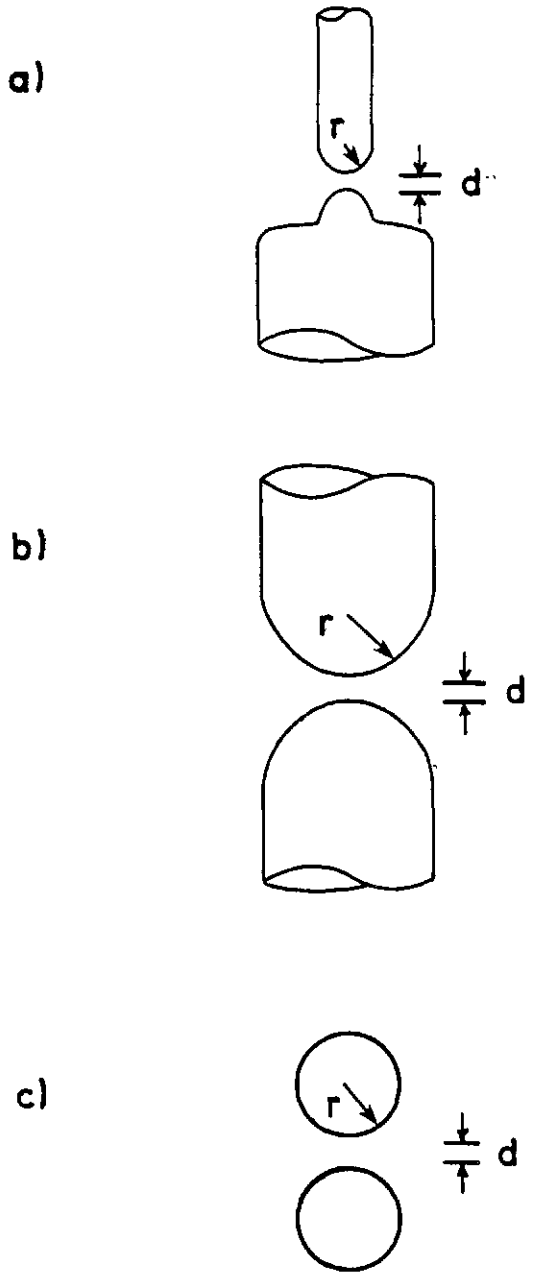

Fig. III-2 Illustrations of electrode geometries, a) nipple-rod electrodes, b) hemispherical electrodes, and c) an idealized sphere gap.

It has been found by analysis of dc breakdown data that both electrode pairs may be represented electrically as a sphere-sphere gap [2]. As shown in Fig. III-2(c), the spheres have a radius r and form a gap d. For an isolated sphere-sphere gap, the field enhancement factor has been analytically determined to be [2]

$$f = \frac{(d/r)^2 + 2(d/r) + 2}{2(d/r + 1)} \quad . \qquad \text{(III-5)}$$

The equivalent radii of the two electrode pairs are known. For the nipple-rod pair the radius is 0.48 cm. For the hemispherical pair the radius is 1.27 cm. Table III-1 gives the field enhancement factor and the geometry correction factor for both the nipple-rod and hemispherical electrodes at different gap spacings as calculated from Eq. (III-5) and Fig. (III-1).

TABLE III-1

FIELD ENHANCEMENT AND GEOMETRY CORRECTION FACTORS

Electrode type	Gap spacing [cm]	f	β
Hemispherical	0.5	1.08	0.74
	1.0	1.25	0.83
Nipple-rod	0.5	1.37	0.90
	1.0	1.84	0.99
	1.5	2.25	1.0

In keeping with the importance of the dc breakdown voltage to the following analysis of pulsed breakdown, extensive dc measurements have been made with both electrode pairs in air and nitrogen [2]. Figure III-3 is a graph of the dc breakdown voltage of the nipple-rod electrodes in air at gap spacings of 0.5 cm and 1.0 cm as a function of pressure. The symbols are experimental measurements and the curves are calculated from Eqs. (III-3) and (III-4) using the parameters in Table III-1. Good agreement is found between experimental data and the semi-empirical calculations.

Similar results are found with nitrogen, as demonstrated by Fig. III-4, for the nipple-rod pair at the same two gap spacings. It should be noted that the calculated curves are the same as those used previously for air, thus there is no appreciable difference between air and nitrogen over this range of pressure (less than 8 atm). Finally, Fig. III-5 contains similar results for the hemispherical electrodes in air at two different gap spacings. Clearly, good agreement is again obtained even though this electrode geometry is substantially different.

Considerable effort has been expended to interpret the dc breakdown characteristics of these electrode pairs, even though they were invariably pulse charged during recovery experiments. This is because the characteristic pulse-charged breakdown voltage of an electrode geometry is intricately tied to its dc breakdown strength. To illustrate this, a model of pulse charged breakdown will now be discussed, along with corresponding experimental results.

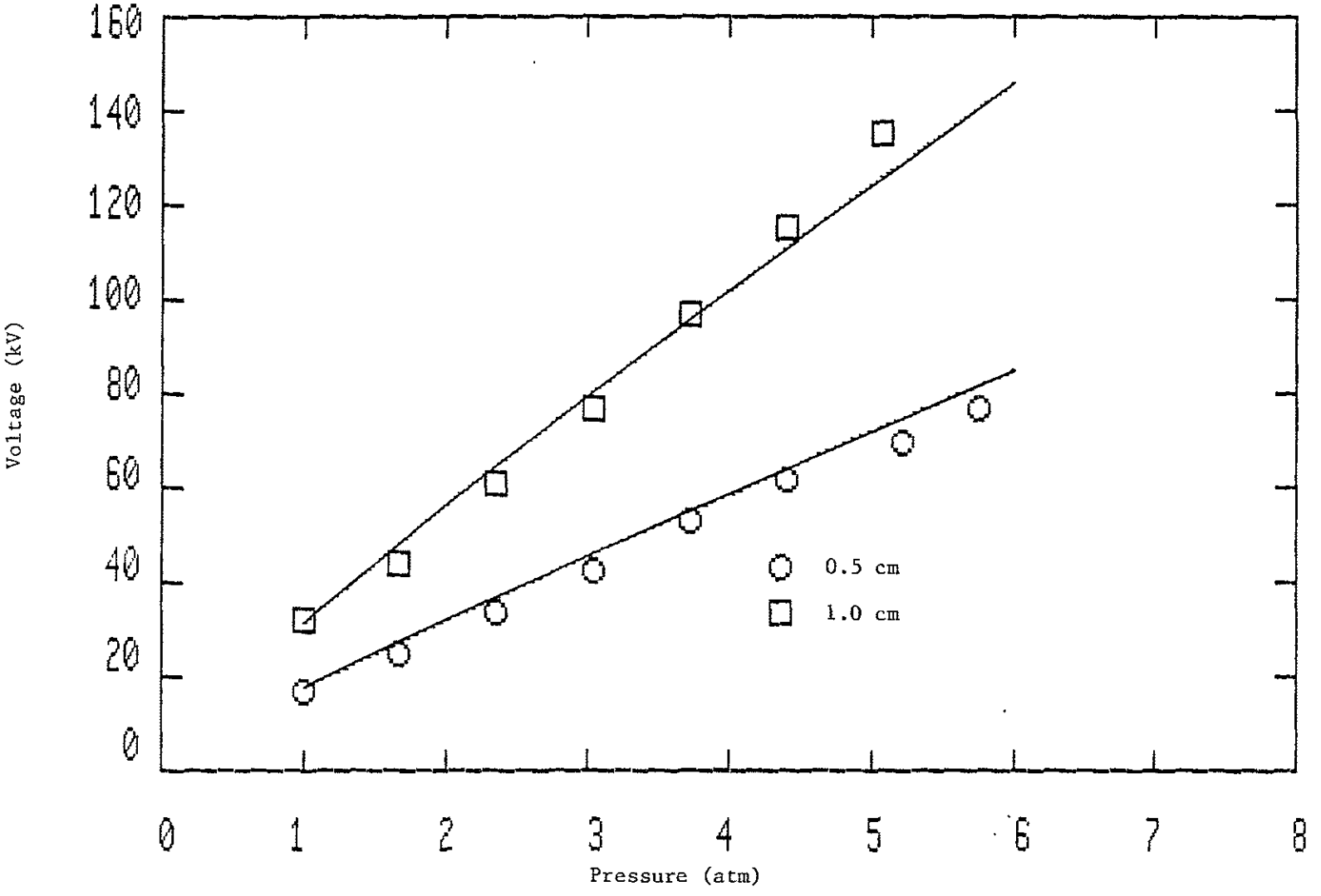

Fig. III-3 DC breakdown of nipple-rod electrodes in air as a function of pressure where symbols are experimental data and curves are theoretical predictions (Reproduced from Ref. [2]).

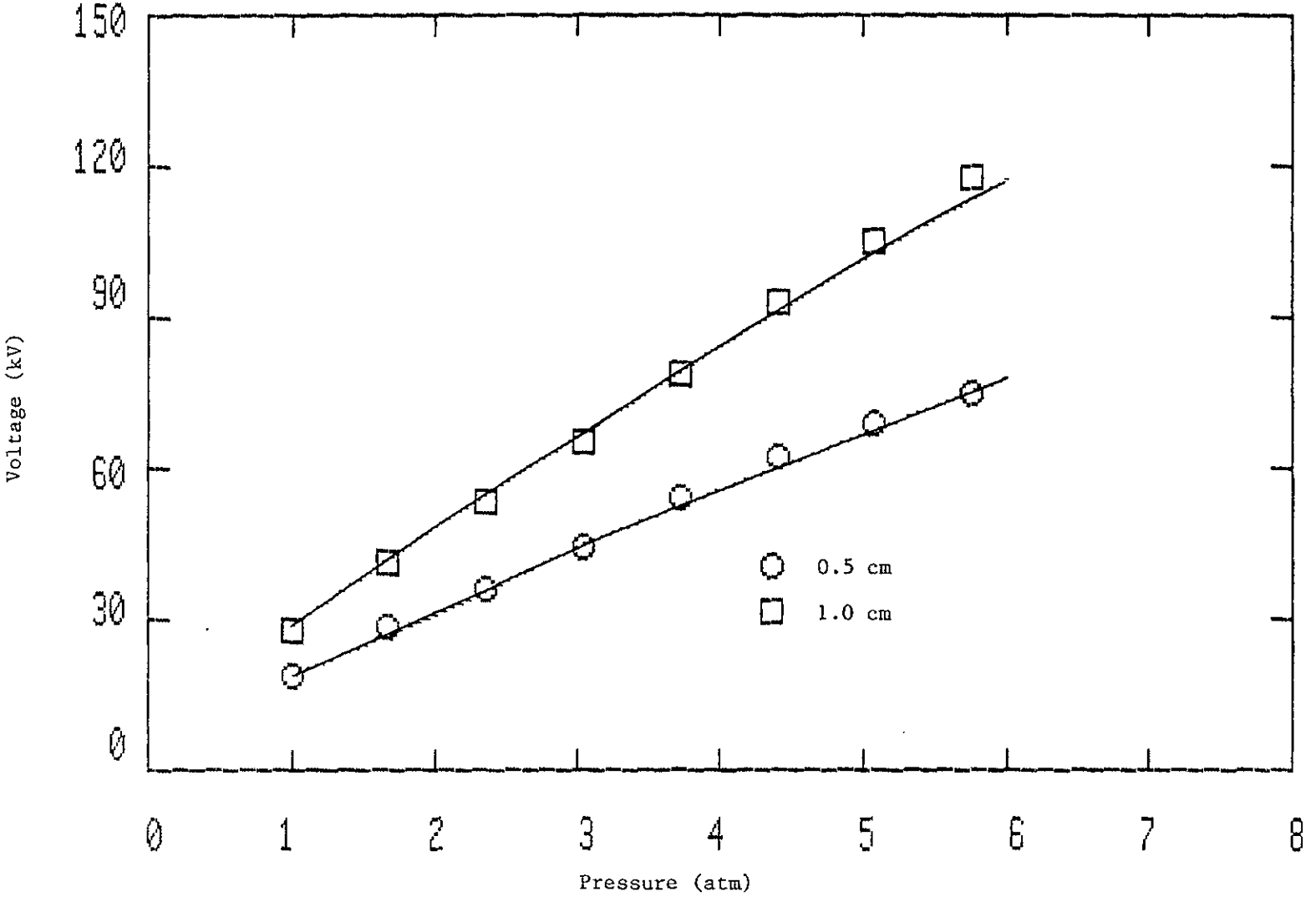

Fig. III-4 DC breakdown of nipple-rod electrodes in nitrogen as a function of pressure where symbols are experimental data and curves are theoretical predictions (Reproduced from Ref [2]).

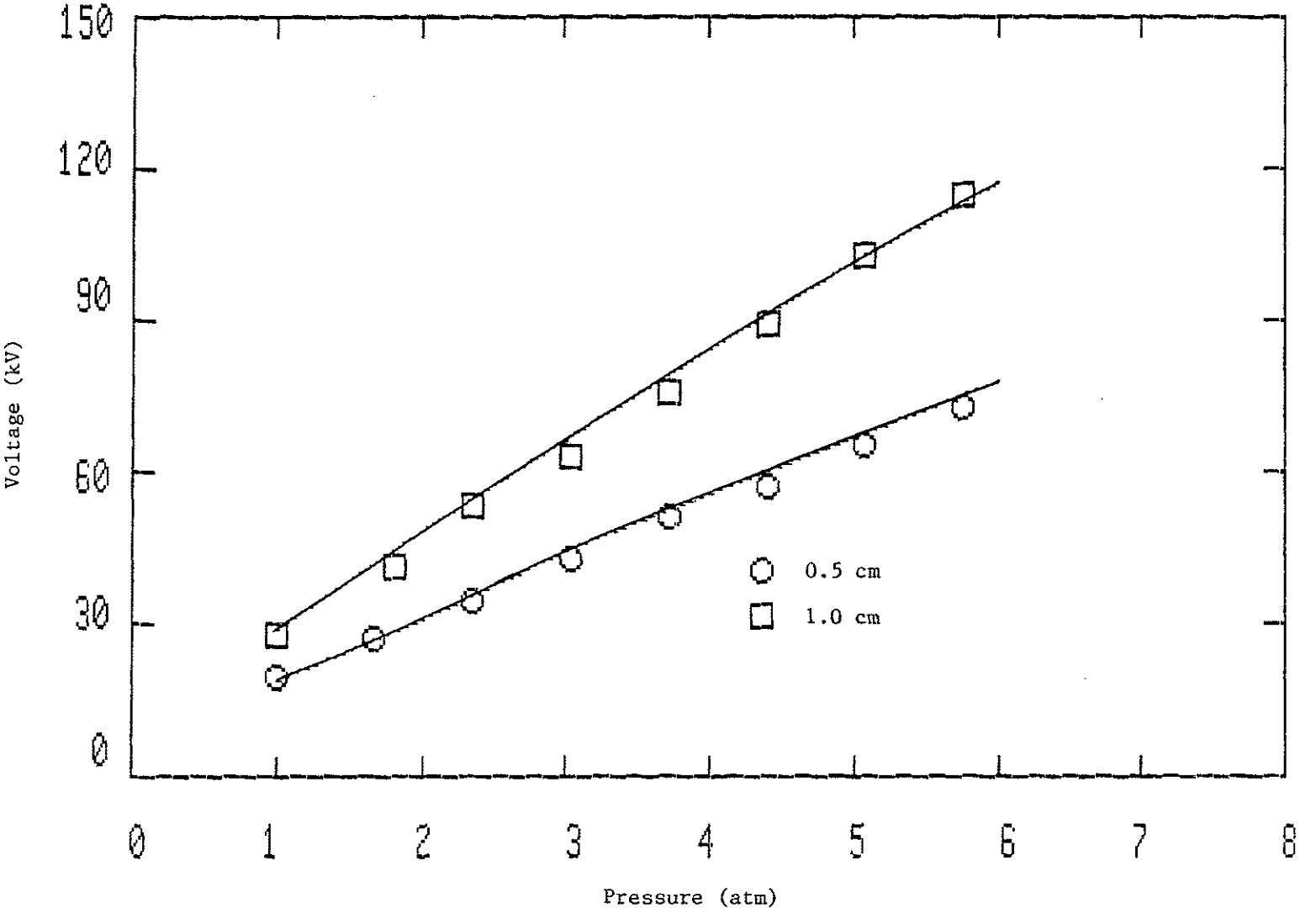

Fig. III-5 DC breakdown of hemispherical electrodes in air as a function of pressure where symbols are experimental data and curves are theoretical predictions (Reproduced from Ref. [2]).

Pulse-Charged Spark Gap Breakdown

When a fast rising voltage pulse is applied to a spark gap, a significant departure from the dc breakdown characteristics occurs. It is well known that the breakdown strength for fast rising square, ramp, sinusoidal, and exponential pulses is considerably higher than for slowly rising or dc voltages [9]. The reason is related to the delay between when an electric field sufficient to break down a gap is applied and when the gap actually breaks down. If the voltage is rising fast enough, then this delay translates into an increase in the voltage across the gap before breakdown occurs. The voltage increase above the static breakdown strength is called overvoltage.

Figure III-6 is an example of the relationship between the pulse-charged breakdown strength and the static strength. These curves are for the nipple-rod electrodes at 1.0 cm in N_2 as a function of pressure. One curve displays the static breakdown voltage while the remaining two curves are for pulse-charged conditions. The voltage pulse was an approximate linear ramp with a rate of rise of about 20 kV/ μs. The lower pulse-charged curve is the breakdown voltage with preionization provided by external UV illumination, while the upper pulse-charged curve is without external UV illumination.

The difference between the two levels of overvoltage illustrates that the delay time consists of two components: the statistical delay and the formative delay. The statistical delay results from a lack of electrons between the electrodes when the voltage is applied thus forcing a delay before the gap may begin to break down. The source of the needed electrons can be cosmic radiation or electrons emitted from the cathode; both processes are random events. Each data point on

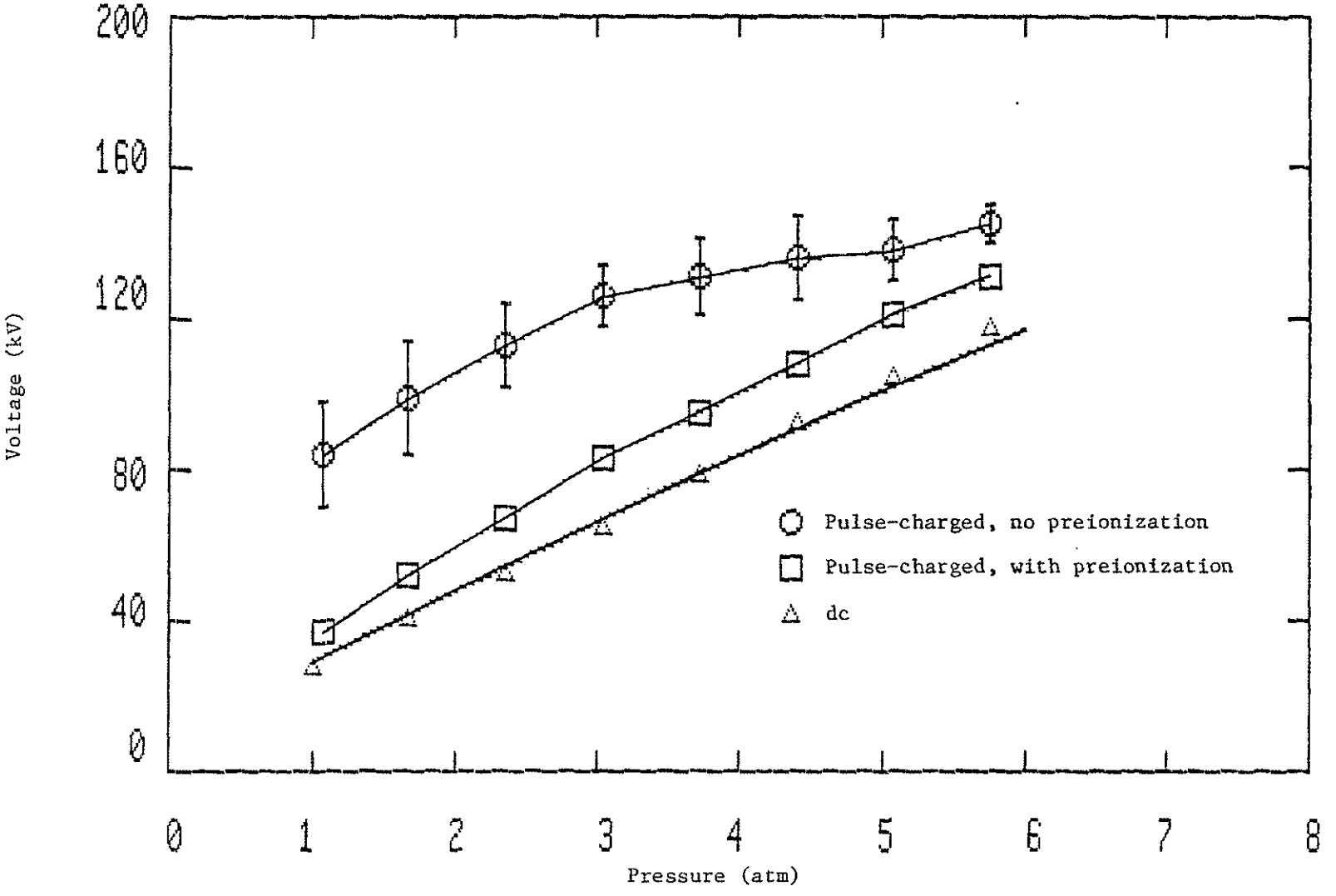

Fig. III-6 Typical pulse-charged and dc breakdown characteristics in N_2 as a function of pressure for nipple-rod electrodes with d = 1.0 cm.

these curves represent the average of 20 pulses and error bars indicating plus and minus one standard deviation are included. The large statistical variation in the highly overvoltaged curve attests to the randomness of the statistical delay.

Statistical delay may be reduced or eliminated by externally applied UV radiation which produces the required electrons prior to the voltage pulse. The resultant curve shown in Fig. III-6 indicates that a time lag still exists because some overvoltage is still present. This delay may be interpreted as the time required for the breakdown to form once a sufficient number of electrons exist in a strong enough electric field. Each data point on this curve is also an average of 20 pulses, but in this case the standard deviation falls within the symbol; therefore, the formative delay is much more deterministic than the statistical delay.

Bad-Gap Operation

Reliable operation of a spark gap with significant statistical overvoltage (in the case of Fig. III-6, greater than 200% at lower pressure) is very difficult. The influence of such variables as humidity, surface condition, and possibly even solar activity further degrades the day to day repeatability. This large uncertainty in the self-breakdown voltage precludes the use of such a switch in virtually all important applications, hence a spark gap operated in this mode is called a "bad gap."

Nevertheless, the shape of the statistically delayed overvoltage curve is interesting as it provides information regarding the pressure dependence of the statistical delay. Referring again to Fig. III-6, it is noted that the statistically overvoltaged curve (upper curve)

initially has a positive slope with pressure that is virtually identical to that of the dc breakdown curve. Above about 3 atmospheres the overvoltage becomes virtually constant with pressure. Finally, as the pressure exceeds 5 atmospheres, the overvoltage once again begins to increase; however, the statistical variation in voltage appears to be decreasing and the curve appears as though it will eventually merge with the curve for the preionized gap.

The overvoltage represented by the statistically delayed curve in Fig. III-6 is actually due to a combination of the statistical delay and the formative delay. If the statistical delay time is to be calculated from the overvoltage curve, then either the formative time must be known or it must be possible to neglect it. Fortunately, it is well known that the formative delay is a strongly decreasing function of overvoltage [9]; therefore, the formative time should be minimized by the large overvoltage caused by the statistical delay. A simple expression for the mean statistical delay results if the formative time is neglected and the rate of rise of the voltage R is constant, such that

$$\bar{\tau} = \frac{\bar{V}_{bk} - V_{dc}}{R} \quad . \qquad \text{(III-6)}$$

The mean statistical delay has been calculated from Eq. (III-6) for the case of the nipple-rod electrodes in N_2 at 1.0 cm and the hemispherical electrodes in air at 1.0 cm. The calculations are displayed in Fig. III-7 versus pressure.

While it should be pointed out that significant error caused by the low number of samples and the neglected formative time (especially above 5 atmospheres) may cloud the results, the curves indicate some

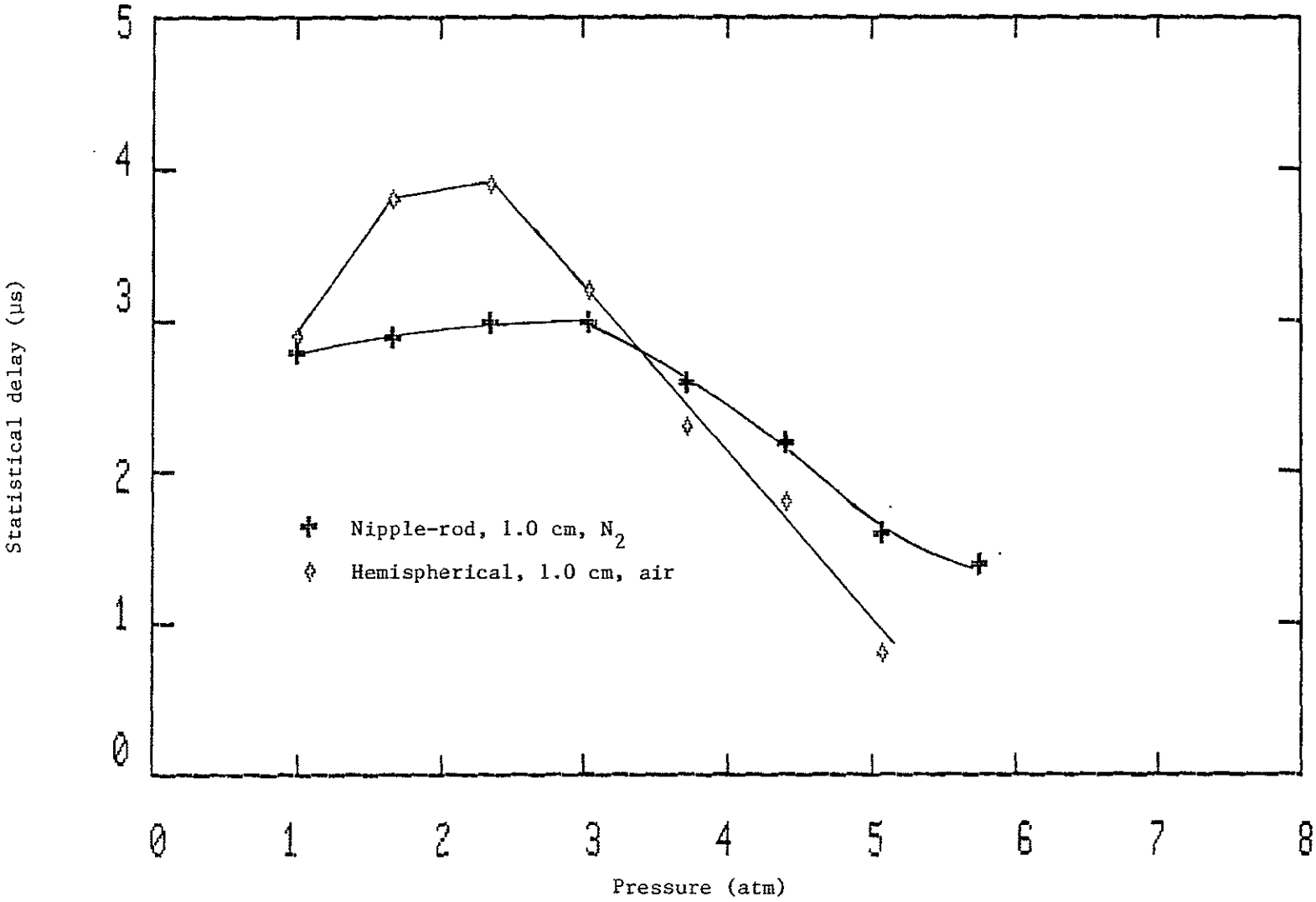

Fig. III-7 Statistical delay versus pressure for two different electrode geometries and gases.

very interesting trends. First, both curves are roughly constant below 3 atmospheres, which accounts for the nearly identical slopes of both the statistically delayed overvoltage curve and the dc curve in this pressure range. This is because the statistical delay is constant with pressure but the dc breakdown strength is increasing, thus the increase in overvoltage is due solely to the increase in the dc breakdown voltage.

For pressure less than 3 atmospheres the hemispherical electrodes suffer the greater mean delay time. In addition, the delay times measured with the hemispherical electrodes seem to start decreasing at a lower pressure (2.5 atm) than those with the nipple-rod electrodes (3 atm); however, this may not be statistically relevant. Finally, both curves are remarkably linear in the range from 3 to 5 atmospheres, the limit of reasonable accuracy. The physical explanation for this functional relationship is not clear at this time. However, a possible mechanism will be suggested based on observations from the literature.

It is known that conditions at the cathode have a significant effect on the statistical delay time. Field emission of electrons at the cathode can be quite significant in pressurized spark gaps because of the influence of microprojections and contaminating surface films [9]. Electric fields on the order of 10^1 to 10^2 kV/cm can reduce the statistical time to microseconds or less. The plateau in delay time at lower pressure may be explained by invoking an "effective surface roughness" that is pressure sensitive [15]. Effective surface roughness is dependent on the electron mean free path (or inversely proportional to pressure), thus electrodes are "rougher" at high pressure, "smoother" at low pressure.

The break point occurs when the characteristic size of the microprojections are on the order of an avalanche length (d_c). At higher pressures, the combination of higher electric fields (breakdown field goes up with pressure) and decreasing mean free path at the cathode makes an avalanche more probable in the vicinity of the projections. A decrease in the mean statistical delay should result. In addition, this model may explain the constant overvoltage observed between 3 and 5 atmospheres since both statistical delay and dc breakdown strength are functions of mean free path, but inversely with respect to each other. Thus, it might be expected that the two effects offset each other equally.

Good-Gap Operation

In contrast to the bad-gap regime, a spark gap operated in the good-gap regime becomes an excellent switch. Operation in the good-gap regime is obtained by introducing a small amount of preionization in the gap prior to the application of a voltage pulse. This preionization reduces or eliminates the statistical delay by creating enough electrons in the vicinity of the cathode that an avalanche is almost certain to start when an appropriate electric field is applied. As a result, the formative delay largely determines the magnitude of the overvoltage and the self-breakdown voltage of the spark gap becomes very deterministic. A spark gap with this characteristic becomes a desirable switch candidate for applications.

As previously mentioned, the formative time is a non-simple function of pressure and overvoltage, among other things. A large body of work has been directed at theoretically understanding the breakdown process (and thus the formative time); however, this work has not

resulted in a reliable means of calculating the formative time based on known conditions in the gap. Fortunately, empirical methods are available.

Specifically, a semi-empirical model of streamer breakdown was offered by T. Martin [15]. While this model has already been mentioned in Chapter II, a brief outline of the model's important points will now be presented. The basic premise of this model is that an anode directed streamer is launched at or near the dc electric field strength of the gap. This streamer, and not the much faster cathode directed streamer, is responsible for the resulting large current rise in the gap as the breakdown occurs. Furthermore, the propagation time of the streamer can be calculated from an empirical equation developed previously by C. Martin at AWRE [28]. Given knowledge of the temporal characteristics of the applied voltage pulse, the overvoltage of the pulse-charged gap can be predicted by attributing the overvoltage to the propagation time of the streamer.

The physical basis of this model is not entirely clear at this time because the particular formulation of the author's streamer mechanism is still a controversial subject. This thesis does not necessarily advocate the mechanism as presented. On the other hand, the method of calculating the overvoltage can be quite useful from an engineering standpoint.

The streamer transit equation developed by C. Martin takes into account overvoltage, pressure, and gap spacing and is transportable to different gases. The equation takes the form

$$E_{\pm}(d\ t_{eff})^{1/6} = K_{\pm}p^{n} \qquad \text{(III-7)}$$

where $E_{\pm}$ is the mean field at breakdown (V_{bk}/d) in kV/cm, t_{eff} is the time in μs during which the field exceeds 0.89 E, p is the pressure in atmospheres, d is the gap spacing in cm, and $K_{\pm}$ and n are gas constants. The $\pm$ signifies that in the original experiments with a point-plane electrode geometry, polarity was also a variable. Table III-2 displays the original values found for these constants in air, freon, and SF_6. While some believe that the polarity effect in such a geometry is indicative of the dependence on the negative streamer for gap closure, it should be noted that polarity is not a strong factor in air as both values for K are the same.

TABLE III-2

EMPIRICAL CONSTANTS FOR STREAMER FORMULA

(from Ref. [28])

	Air	Freon	SF_6
K_+	22	36	44
K_-	22	60	72
n	0.6	0.4	0.4

The total streamer transit time, t_s, can be found by assuming a linearly rising ramp voltage and taking into account the experimental assumption made at AWRE when formulating this equation, namely, that the streamer left the very sharp point of the electrode at t = 0 when the voltage was first applied [15] (i.e., negligible dc breakdown strength). From these two assumptions, t_s is found from Eq. (III-6) to be

$$t_s = t_{eff}/(1-.89) = t_{eff}/.11 \quad . \qquad \text{(III-8)}$$

In order to express t_s in terms of the gap parameters, Eq. (III-8) is substituted into Eq. (III-7) to eliminate t_{eff} such that

$$t_s = d^5(Kp^n/V_{bk})^6/.11 \qquad \text{(III-9)}$$

where V_{bk}/d has also been substituted for E. The best values for K and n have been found from a least squares fit of Eq. (III-9) to three sets of values for t_s. The values were calculated from breakdown data for the nipple-rod electrodes in air at gap spacings of 0.51 cm, 1.0 cm, and 1.5 cm. The calculations were made using Eq. (III-6) as was done with the statistical delay, except V_{bk} was taken from the pulse charged data with UV preionization. With UV preionization it is assumed that the statistical delay is negligible and the overvoltage is entirely due to the streamer transit time (formative delay). The best fit to this data was found when K is 19 and n is 0.9, which is not an unreasonable deviation from the AWRE values. In fact, T. Martin made a comparable alteration of n in order to fit his SF_6 data [15].

Enough information is now available to make calculations for the expected breakdown voltage. In order to calculate V_{bk}, the streamer transit time must be eliminated from Eq. (III-9). Figure III-8 demonstrates that the final breakdown voltage depends on the nature of the applied impulse and t_s. In this case, a linear increase of the voltage above the dc breakdown strength occurs over the time t_s such that

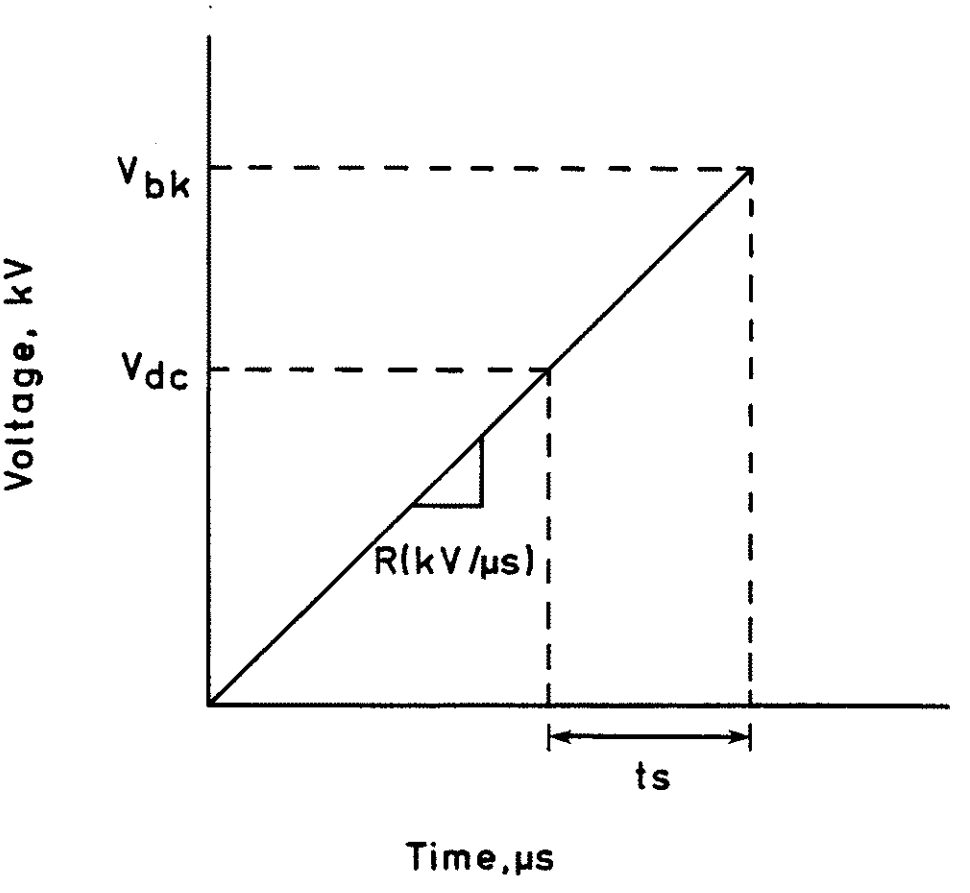

Fig. III-8 Model of pulse-charged breakdown with an applied linear ramp voltage.

$$V_{bk} = R\, t_s + V_{dc} \qquad \text{(III-10)}$$

where R is the rate of rise of the voltage in kV/μs. The combination of Eq. (III-9) and Eq. (III-10) results in a seventh order polynomial in V_{bk} of the form

$$V_{bk}^7 - V_{dc}V_{bk}^6 - C = 0 \ . \qquad \text{(III-11)}$$

In this equation, C contains the gap parameters and the rate of rise of the voltage such that

$$C = Rd^5K^6p^{6n}/.11 \ . \qquad \text{(III-12)}$$

The solution to Eq. (III-11) is easily accomplished numerically using known data for V_{dc}, d, and p. Equation (III-11) has only one real root; therefore, this root is taken as the useful solution. It should be noted that different electrode geometries are accounted for by the inclusion of the dc breakdown voltage; thus, Eq. (III-11) should successfully predict the pulse charged breakdown data for the hemispherical electrodes even though this data was not included in the curve fit.

Solutions for all electrode geometries and conditions used in this study have been calculated and compared with experimental data. The dc breakdown voltage was calculated using the equation previously discussed [Eq. (III-4)] to avoid experimental error. In addition, this allowed the pulse charged breakdown voltage for the nipple-rod electrodes at 1.5 cm to be calculated even though no dc data were available. The results are presented in Figs. III-9, III-10, and III-11.

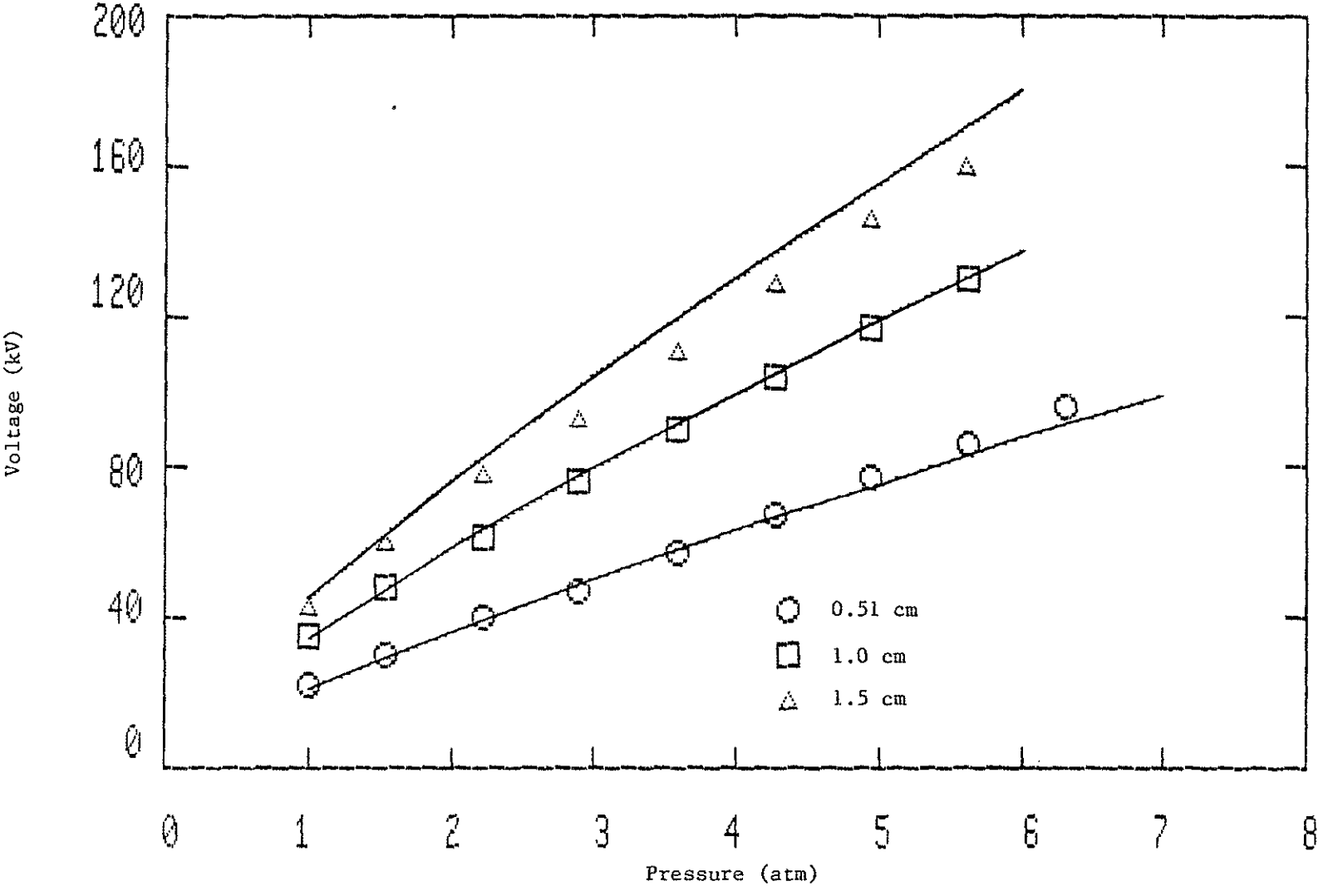

Fig. III-9 Pulse-charged voltage breakdown of gap as a function of pressure with nipple-rod electrodes in air. Symbols are measurements with UV illumination, curves are calculations.

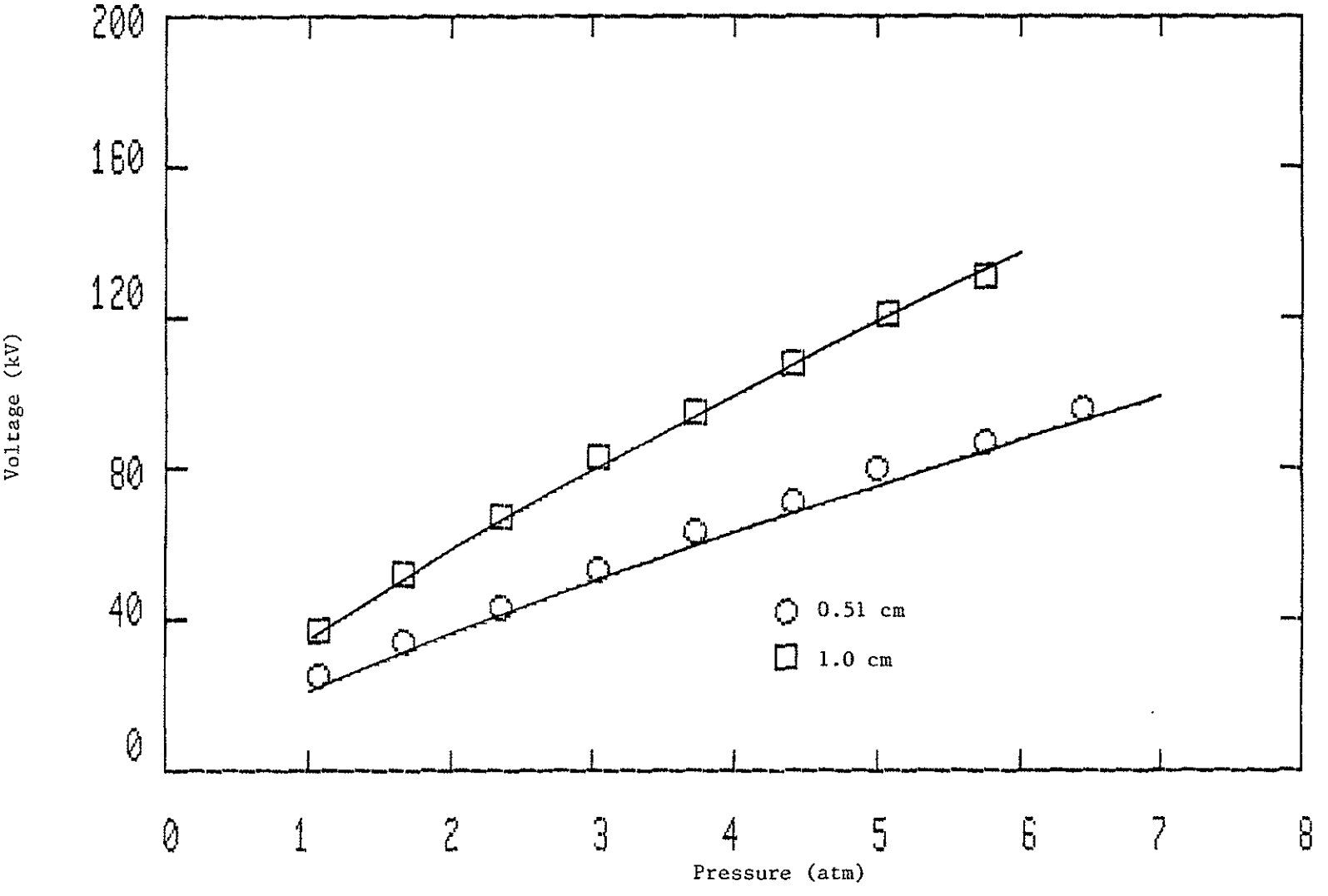

Fig. III-10 Pulse-charged voltage breakdown of gap as a function of pressure with nipple-rod electrodes in nitrogen. Symbols are measurements with UV illuminations, curves are calculations.

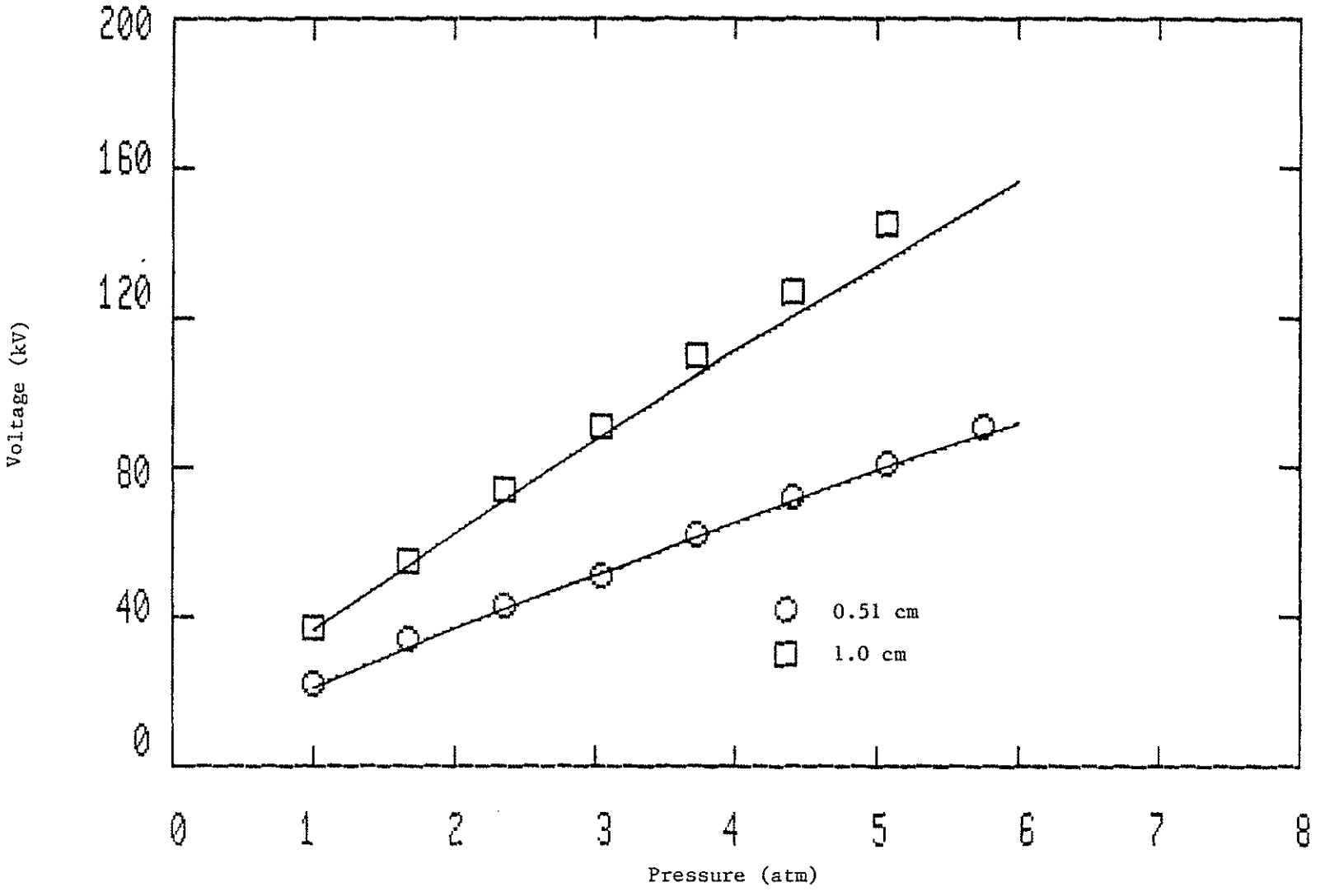

Fig. III-11 Pulse-charged voltage breakdown of gap as a function of pressure with hemispherical electrodes in air. Symbols are measurements with UV illumination, curves are calculations.

Figure III-9 plots pulse-charged breakdown voltage versus pressure in air for the nipple-rod electrodes at three different gap spacings. The symbols are experimental measurements while the curves are calculated. The agreement between the data and the calculations is quite good which indicates that the least squares fit was well correlated. Figure III-10 is similar to Fig. III-9 except that the gas is nitrogen. Again good agreement is evident which indicates that the gas constants are about the same for both air and nitrogen. Finally, Fig. III-11 shows the results obtained in air with the hemispherical electrodes at 0.51 cm and 1.0 cm gap spacings.

Clearly, the calculations fit the data well although the 1.0 cm hemispherical data and the 1.5 cm nipple-rod data indicate some disagreement. However, it should be noted that at the higher gap spacings and pressure the assumption of a linear ramp begins to fail because a larger portion of the charging waveform is used. Since this waveform is actually more like a 1-cosine shape, the rate of rise of the voltage cannot be considered constant over a wide range of voltage, which introduces considerable error. Nevertheless, the calculations are in agreement to within 5% over most of the data.

Operating Regime Transitions

Two distinct operating modes have now been described for the same spark gap. While UV illumination was used to trigger a transition from the bad gap regime to the good gap regime, other techniques also exist. A discontinuous transition is not necessary because smaller levels of preionization will result in reduced but still significant values of statistical delay. This is because the breakdown process is an inherently statistical phenomenon [8]. In other words, without a

substantial number of suitable electrons in the vicinity of the cathode, the numerous electron loss processes will preclude a successful avalanche from forming at least for a period of time. These electron processes include recombination, diffusion, and attachment (negative ion formation). Attachment can be a particularly fast loss mechanism in an electronegative gas such as oxygen (air) and SF_6. Thus, a small level of preionization may reduce the statistical delay, but will not "eliminate" it. A large enough concentration of electrons will ensure that a successful avalanche is certain to form when an appropriate electric field is applied. This condition results in a statistical delay that is substantially less than the formative delay.

An obvious question pertains to the minimal number of electrons required to make the statistical delay insignificant. Good discussions of avalanche statistics are given by Llewellyn-Jones [8] and in Meek and Craggs [9]. The conclusion found for uniform fields is that 10^3 electrons or greater near the cathode virtually ensure that a self-sustained discharge will form at the sparking potential in a typical gas such as hydrogen. It has been shown that UV illumination can generate greater than 10^4 photoelectrons/cm^3 without difficulty [29], and such preionization virtually eliminates any experimentally measured statistical delay. However, UV illumination is not the only mechanism that will produce such densities.

Thermionic emission from metallic surfaces is a widely used method for making available large numbers of free electrons in an electrode region. The most well known application, of course, is in electron vacuum tubes used for amplification. However, the emission does not reach a substantial level until high temperatures are reached. For

example, at temperatures near the melting point for copper (1356 K) the electron emission can be estimated using Richardson's law [4] to be on the order 10^9 electrons/$cm^2 \cdot s$, well above that for cosmic radiation or even field emission [9]. Interestingly enough such temperatures are reached and exceeded in the cathode spot after an arc has formed [17]. Thus it can be assumed that the cathode spot is a source of initial electrons, but that the rate of electron production falls off quickly as the electrodes cool.

Another mechanism effecting the statistical delay involves the metal vapors injected into the gap by the interaction of the arc with the electrodes. Metal vapor jets may form, if the current is high enough, and contribute greatly to electrode erosion [30]. These metallic particulates introduce substantial electric field distortions which result in a larger field emission electron flux and larger local values of α. It can be shown that a particle idealized as a sphere will have a dipole moment induced on its surface by an external electric field. If the external field is approximated as uniform, then the local field is intensified by a factor of three. This distortion intensifies α, thus allowing a smaller number of background electrons to initiate a breakdown, at least until the larger particles have returned to the electrode surface or have been cleared by gas flow.

The effect of these two mechanisms should be to "self-preionize" the spark gap after an initial breakdown has occurred. In other words, these mechanisms should reduce the statistical delay of the second pulse in a fashion similar to UV illumination, provided that enough electrons are created and the presence of impurities (metal vapors) does not disrupt the breakdown process. This "preionization" will only

be significant if the next voltage pulse is applied while the electron emission and field amplification is still substantial. Therefore, it should be possible to detect the waning influence of these mechanisms on the statistical delay by observing a steady increase in the overvoltage as the time between pulses is increased.

Pulse-Charged Recovery

If a two-pulse burst without external irradiation is applied to a relatively smooth, small area spark gap at lower pressure, then the recovery curve will typically appear as shown in Fig. III-12. This curve may be divided into four regions. The first is at short interpulse times and is called the knee of the recovery curve. The knee of the curve represents the recovery of the spark gap to at least its original dc strength. If the second pulse breakdown voltages of several subsequent bursts are averaged, the resulting standard deviation is rather large as indicated by the error bars.

The second region is called the plateau. If the pulses applied to the electrodes have a fast risetime (e.g., microsecond regime) the breakdown voltage of the plateau is found to be slightly above the dc strength of the gap. Thus, the gap is overvoltaged in this region. Throughout the plateau region the breakdown voltage is not a function of the interpulse time and is quite steady, exhibiting a small standard deviation. The plateau may extend for over a decade or more in time, but the breakdown voltage will eventually begin to increase again.

The region where the overvoltage again increases and approaches full recovery is called the transition region. The transition region is less clearly defined because the statistical scatter in the data increases significantly. However, a relatively smooth curve can often

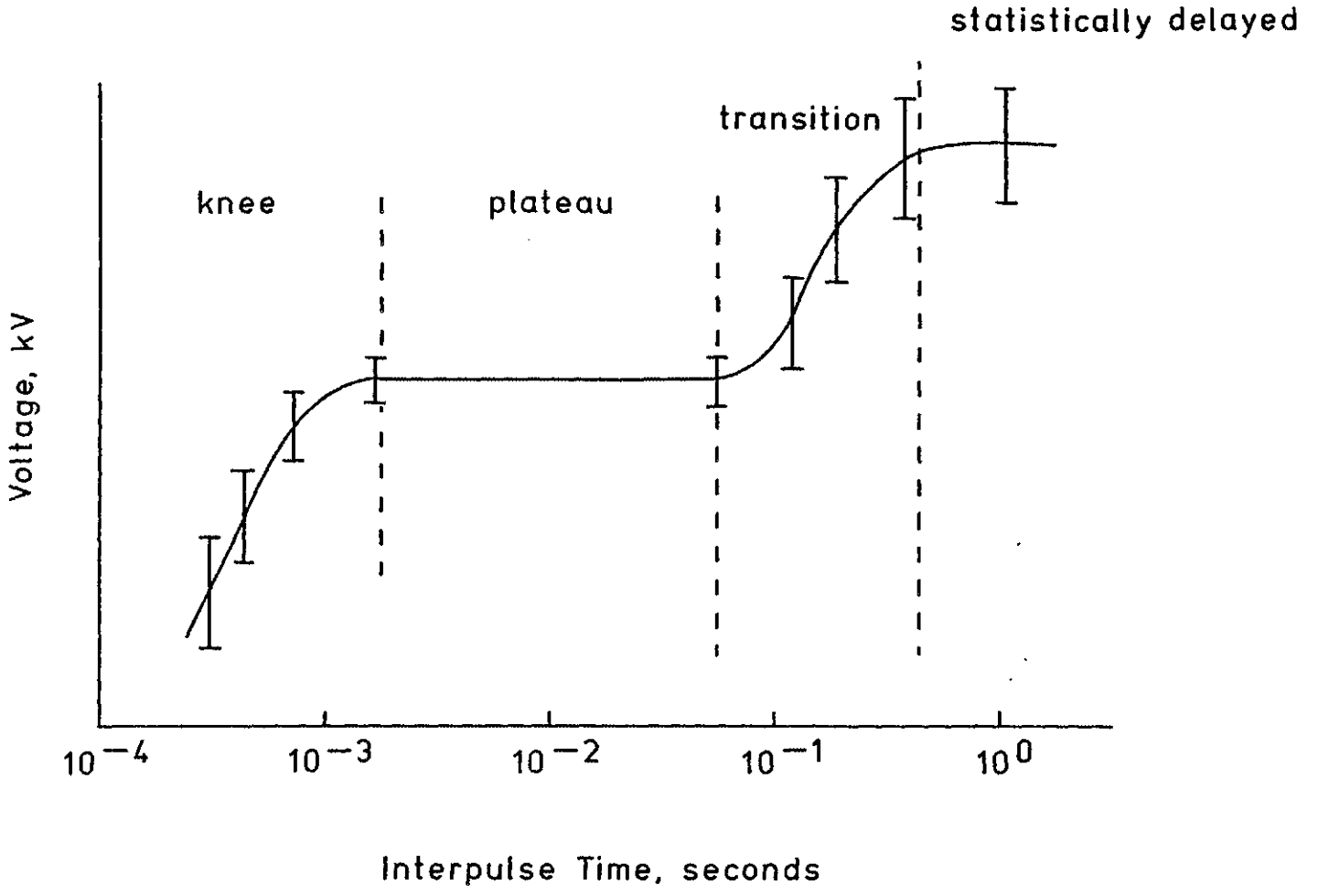

Fig. III-12 The idealized recovery of a pulse-charged spark gap without irradiation. The curve represents the mean value of several second pulse (two-pulse burst) breakdown voltages versus the time between the two pulses.

be drawn through the mean of the breakdown voltages. In this region, the mean breakdown voltage steadily increases with increasing interpulse time, until a new plateau is reached.

The final subdivision is called the statistically overvoltaged region. Reliable operation of the spark gap is difficult in this region because of the large statistical variations in the breakdown voltage. The overvoltage is quite high, being well over 100% at lower pressures. However, the mean breakdown voltage is no longer a function of interpulse time. The amount of time required for the spark gap to reach this region can be very long; for spark gaps with no gas flow, this time may reach into the hundreds of milliseconds or longer.

Significantly, this curve illustrates how the spark gap recovers in two stages. Initial recovery occurs as the knee of the recovery curve transitions to the plateau. Final recovery occurs when the transition region gives way to the statistically overvoltaged region. Extensive experimental support for this model has been obtained at the Gas Flow Switch Laboratory (GFSL) [21], [2] and by others, including Moran and Hairfield [20] in static spark gaps, and at Spectra Technology (formerly Mathematical Sciences Northwest) [25] in gas blown rail gaps. Thus, the experimental evidence indicates that this recovery trend occurs in static as well as gas blown spark gaps. A physical model of the observed recovery process will now be offered that identifies the mechanisms controlling the initial and final recovery of a spark gap.

Model of Initial Recovery

After the current through the spark channel goes to zero, the channel begins to deionize. Deionization occurs very quickly, on the order of tens of microseconds for gases such as air [9]. Thus, the gas makes a rapid transition from a conductor back to a dielectric. In terms of recovery, this deionization causes the gap to recover some of its dielectric strength, but the measured breakdown voltage is still well below the undisturbed dc strength of the gap [17]. This is because the gas in the immediate vicinity of the electrodes is still quite hot, having temperatures in excess of 1500 K [9], [17]. Since the interelectrode region is at pressure equilibrium with the surrounding gas (shock waves having been dissipated), the high temperatures cause the local gas density to be well below ambient. Thus without significant initial space charge, the gap acts in a similar fashion as one operated at a much lower ambient gas density and a much lower self-breakdown voltage.

As time progresses, and in the absence of gas flow, the gas in the interelectrode volume cools by conduction to the electrodes and by turbulent diffusion into the cooler surrounding gas. As the gas cools, the gas density increases and the self-breakdown voltage of the gap increases. However, the turbulent nature of this cooling and the inhomogeniety of the gas density results in an increased statistical scatter of the breakdown voltage (higher standard deviation) on the knee of the recovery curve.

The electrodes, on the other hand, cool at a different rate [17] because of their significantly different heat transfer characteristics. At the surface, portions of the electrodes receive

heat from the gas, while other portions (the cathode spot) may be supplying heat to the gas. In addition, the electrode volume and support structure serve as a large heat sink for cooling the electrodes. This bulk process typically dominates convective processes in the cooling of the electrode surface. The difference in gas and electrode cooling rates results in an initial increase in the self-breakdown voltage, followed by a slower increase to the plateau.

With gas flow, the situation is somewhat different. The volume of hot arc debris is now convected downstream from the electrodes at a rate approximately given by the undisturbed gas velocity. At high velocity, the clearing of the interelectrode region occurs much faster than the gas cooling and dispersion mechanisms, thus it can be said that the interelectrode volume is not cooled, but replaced. The arc debris is no doubt cooled at a higher rate because of the increased mixing that the gas flow induces, but over the times required to clear the gas (10^{-4} to 10^{-3} seconds) the density of this debris does not increase to ambient. The implication with regard to recovery is significant.

Density visualization experiments, such as schlieren photography, clearly indicate that the arc debris does not move downstream in a homogeneous mass, but is elongated and diffused [26]. This can be interpreted by considering the expansion of the arc-generated debris in the background flow field. The shock waves originally created by the arc cause an initial expansion of the debris upstream and downstream. As the shocks weaken, the expansion velocity subsequently decreases. The superposition of the slowing expansion velocity and the steady free-stream gas velocity results in different velocities for different

portions of the original debris. Thus, the debris cloud is extended in the flow axis direction because the downstream portions of the cloud clear the electrodes somewhat faster than the central portion, but the upstream edge is delayed.

In addition, clearing is further delayed by the entrapment of debris in vortices caused by the wake of the electrodes. At high repetition rates, this leaves a hot, low density region of gas adjacent to the downstream edges of the electrodes when the second pulse is applied. In such cases, the spark gap is observed to breakdown through the arc debris even when this breakdown path is considerably longer than the distance between the electrodes, presumably because the integral of the lower density along this path is less than the integral of the higher gas density between the electrodes [18], [19].

In order to quantitatively predict the effect of gas purging on the recovery performance of the gap, a clearing factor is employed. It is often described in the literature as the number of interelectrode volumes that must be purged before complete recovery occurs [5]. A definition that is perhaps closer to the actual physical process uses a ratio of gas velocity, time to recovery, and a characteristic dimension such as

$$CF = U \cdot \tau / L \quad . \qquad \text{(III-13)}$$

Ideally, for a specific electrode configuration, the clearing factor should be constant over velocity; however, this is rarely the case in practice because the clearing factor does not take into account the competing effects of wake turbulence, turbulent diffusion and expansion, and boundary layers [18]. However, by careful selection of

the characteristic dimension, the clearing factor may still be useful, at least over a limited range. It has been found with data previously taken at GFSL that when L is defined to be equal to the electrode radius plus one gap spacing L = r+d, good agreement is found between the time to initial recovery and the calculated τ as a function of U [2].

A more rigorous attempt to calculate the time to initial recovery ("knee" of the recovery curve) must include a thorough description of the relation between the debris cloud, the path length, and the spatially non-uniform electric field because the trade-off between breakdown path length and reduced gas density seems to control the initial recovery process. In other words, the gap breaks down at a reduced voltage by striking through the less dense arc debris, but only if the path length is not too extended. When it is no longer "easier" to breakdown the gap through the debris cloud, the spark returns to the direct path between the electrodes.

A physical model of this process should begin by taking into account the sensitivity of the primary Townsend coefficient on E/N. This technique is already used in the theoretical description of non-uniform spark gaps by making α a function of position because E is spatially dependent [10]. However, in the case of recovery in non-uniform gaps (the case considered here), α becomes an extremely sensitive function of position because now both E and N are spatially dependent. Compounding this complex situation is the problem of relating ionization coefficients to the final breakdown voltage; however, the use of numerical techniques, such as Monte Carlo

calculations, could produce quantitative predictions of the time to initial recovery in a more rigorous theoretical manner.

When the spark location finally returns to the interelectrode region, a discharge forms through gas that is at the same density and temperature as before the first pulse. However, the self-breakdown voltage of this second pulse falls on the plateau of the recovery curve, below that of the first pulse self-breakdown voltage. Measurements have conclusively determined that the plateau occurs at the pulse-charged breakdown voltage exhibited by the gap under the same conditions of pressure and electrode spacing when irradiated with UV illumination (the "good-gap" regime), even if no external irradiation is applied. Thus, for interpulse times corresponding to the plateau region, there is still some memory of the first pulse. This memory is not sufficient to disturb the breakdown process, but it does reduce or eliminate the statistical delay. Eventually, if the interpulse time is long enough the memory of the first pulse finally fades and the statistical delay gradually returns along with the corresponding large overvoltage.

Model of Final Recovery

The transition region, as previously defined, identifies the final recovery of the gap. This occurs when it is no longer probable that the available electron density will cause a breakdown at the minimum electric field. Thus, the spark gap makes a transition from operation in the good-gap regime to operation in the bad-gap regime. Whether this occurs because of a lack of electrons or a reduction in the local electric field is not fully known, but the results of gas flow recovery experiments have shed considerable light.

It is fully expected that a large number of free electrons are available in the spark gap region at times consistent with the knee of the recovery curve, both from incomplete deionization of the spark channel and from thermionic emission at the still hot electrodes. However, as time progresses any free electrons left over from the initial spark and the immediate aftermath are completely removed by recombination, diffusion, and attachment or by convection downstream in the case of gas flow. Nevertheless, the time for final recovery in static spark gaps often extends for hundreds of milliseconds, and in the case of gas flow the time is always much greater than that required to flush the interelectrode volume several times. Therefore, there must be a source of electrons for a time after the gap has been cleared of the first pulse arc debris.

Thermionic emission from the cathode is a likely explanation for the observed final recovery in gas blown spark gaps. The high temperatures at the cathode spot after the arc make it a good source of electrons. Even as the cathode surface cools, sufficient quantities of electrons to be a preionization source should be emitted. It has already been established by previous researchers that in static gaps the electrodes cool more slowly than the gas [17]. On the other hand, increased convection from the electrodes caused by gas flow might be expected to cool the electrodes faster, resulting in the thermal emission of electrons to fall below the critical number in a shorter time. In fact, the time to final recovery has been found to be a decreasing function of velocity; however, preliminary heat transfer calculations have failed to demonstrate convection by gas flow to have a significant cooling effect as compared to conduction through the bulk

material. A more detailed description of these calculations will be given in Chapter VI.

Another possible mechanism for explaining the final recovery time is the entrapment of impurities in slower moving boundary layers near the cathode. The most promising impurities are the metal particulates injected into the gap by the arc because of their capacity to distort the electric field. This hypothesis is difficult to test given the unknown quantities of particulates trapped and the unknown nature of the boundary layers themselves in a relatively complex flow field. However, the velocity of the boundary layers can be approximated by simplified models (e.g., flat plate flow or an equivalent) and it is certain that the boundary layer velocity is smaller but proportional to the undisturbed gas velocity. Thus, a logical approach would be to define a boundary layer clearing factor based on idealized flow dynamics, similar to the clearing factor used for initial recovery.

Since final recovery occurs because of the low probability that breakdown will occur at the minimum field strength, it stands to reason that final recovery to the bad-gap regime can be precluded by applying external irradiation in advance of the second pulse. If both pulses are irradiated, then they will both break down on the plateau even at the longer interpulse times; therefore, the initial recovery of the gap will also correspond to 100% recovery of the first pulse breakdown strength, a desirable attribute from an applications standpoint. It should be noted that for interpulse times shorter than that required to give final recovery, the second pulse will break down on the plateau whether or not irradiation is applied first.

It has been reported in the literature that if recovery is expressed as a percentage of first pulse breakdown strength, the plateau "disappears" as the pressure is increased [20], [21]. This is easily explained by pointing out that the statistically delayed overvoltage decreases with pressure but that the overvoltage caused by the formative delay remains significant. Therefore, the percent difference between good-gap breakdown and bad-gap breakdown decreases. Eventually, as the pressure increases, final recovery is precluded all together and the plateau corresponds to 100% recovery.

CHAPTER IV

EXPERIMENTAL APPARATUS AND PROCEDURES

The goal of this thesis is to study gas flow switches under controlled conditions so as to develop and validate a model of gas-flow-enhanced spark gap recovery. The Gas Flow Switch Laboratory was built at Old Dominion University expressly for this purpose. This chapter presents an overview of the pulsed power system and the gas flow apparatus that constitutes the test facility. Greater detail on the design and performance of the facility can be obtained from the references that will be cited.

The experiments that were conducted in the laboratory had three basic objectives. First, the pulse charged breakdown characteristics of electrode pairs used in the gas flow switch were measured in order to identify the "bad gap" and "good gap" operating regimes. The tests were conducted without gas flow and as a function of pressure. External preionization was provided by a two-pulse UV source in order to eliminate statistical delay. Next, recovery experiments were conducted without gas flow (static) so as to obtain base data on switch recovery performance as well as to demonstrate the similarities between static recovery and gas blown recovery. Again, a comparison was made between no preionization and the application of two-pulse preionization with interesting results. Finally, recovery experiments with gas flow

were performed in the test facility's blowdown wind tunnel over a velocity range of 25 m/s (Mach 0.07) to 360 m/s (Mach 1). Once again, externally applied preionization was used to identify the operating regime of the spark gap.

Switch recovery is measured by producing two-pulse bursts. An initial pulse is applied to the switch which is consequently broken down at a potential V_1. After a precisely controlled time interval, another pulse is applied to the switch and the hold off potential of the switch, V_2, is then recorded. The relative value of V_2 with respect to V_1 gives the recovery of the switch. In order to make such measurements in a controlled manner, a pulsed power system capable of generating two identical pulses is needed. Such a system is available at the Gas Flow Switch Laboratory.

Pulsed Power System

A two-stage resonant charging system for a Blumlein pulse forming line (PFL) creates the two pulses across the switch. Figures IV-1 and IV-2 present a block diagram and a simplified schematic of the system. Referring to Fig. IV-1, the basic components of the system include a dc power supply capable of low-current charging to 15 kV, a two-pulse modulator containing a capacitor bank and an ignitron switch, a switch chassis containing an intermediate storage capacitor and a pair of thyratron switches, a step-up resonant transformer, and a water dielectric Blumlein. The Blumlein is switched to a liquid load by the gas blown spark gap under test. Additional service equipment indicated in Fig. IV-1 includes a water purification system for the Blumlein, a load solution circulation system, and appropriate trigger generators for the switches.

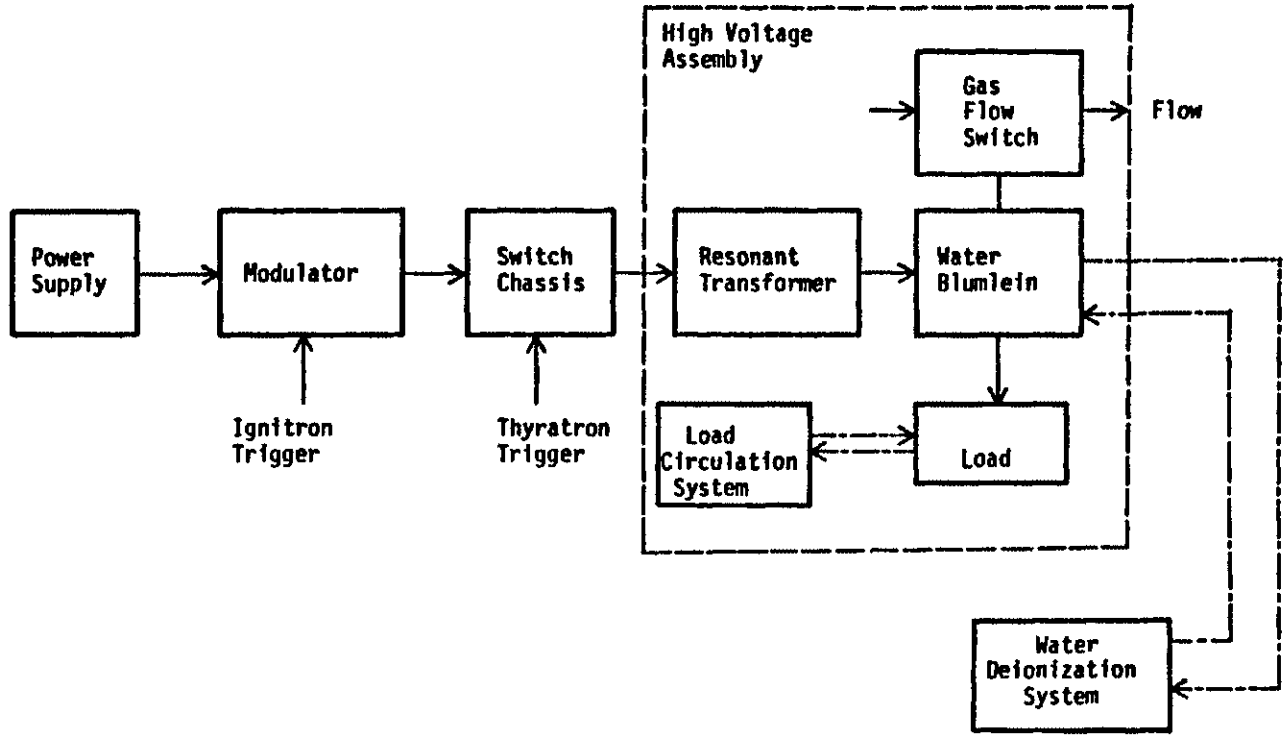

Fig. IV-1 Block diagram of the pulsed power system for the Gas Flow Switch Laboratory (from Ref. [1]).

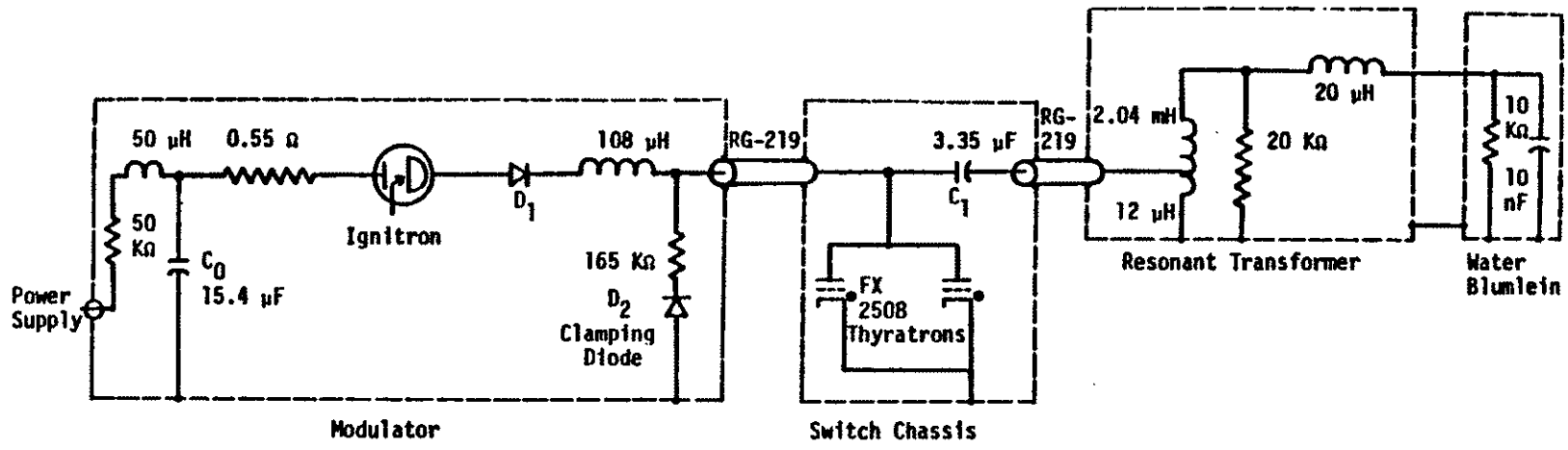

Fig. IV-2 Simplified circuit diagram of the pulsed power system (from Ref. [1]).

Figure IV-2 presents a more detailed schematic diagram of the system. The modulator capacitor bank, C_0, is resistively charged to a voltage as high as 15 kV by the dc power supply. This represents enough energy to form one burst of two pulses. After C_0 is charged, the ignitron is triggered so that the switch chassis capacitor, C_1, is resonantly charged through the 108 μH inductor and the primary of the resonant transformer. Discharging of C_1 is prevented by the diode stack, D_1. This leaves C_1 charged with enough energy to form one pulse. Because of the corresponding voltage gain of the charging process, C_1 is left with up to 20 kV across it.

After the ignitron recovers, the FX2508 hydrogen thyratrons are triggered to begin the next stage of the charging cycle. The resonant transformer, originally designed for the ETA experiment at Lawrence Livermore National Laboratory [31], is tuned so that an off-resonant condition exists between C_1 in the primary circuit and the Blumlein in the secondary circuit. As a result, the secondary voltage peaks just as the primary current goes through a zero, thus allowing the thyratrons to recover. The resonant transformer steps up the voltage by a factor of 13 so that the maximum charging voltage of the Blumlein is 250 kV. This voltage appears directly across the gas blown switch, which is allowed to self break causing a current pulse of up to 50 kA to flow through the switch; a corresponding current of up to 25 kA flows through the load. This completes the formation of the first pulse.

Upon completion of the first pulse, the voltage on C_0 is reduced and the switch chassis capacitor C_1 is left with a 57% voltage reversal. The residual charge remaining in the two capacitors presents

different initial conditions than when the first pulse was formed. However, it can be shown that a second pulse identical to the first is produced when suitable values of C_0 and C_1 are chosen [1]. After a carefully controlled time interval as short as 100 μs, the thyratrons are triggered a second time, and a second Blumlein pulse with better than 3% regulation is produced [32]. This completes a two-pulse burst.

After C_0 is recharged, another burst may be initiated; a burst repetition rate of 0.3 pps is possible. Further specifications of the system are given in Table IV-1. A more detailed discussion of the design, construction, and performance of the pulsed power system is given in Refs. [1] and [32].

Gas Flow Apparatus

The gas flow apparatus consists of two different wind tunnels: a high-pressure, closed-circuit, low-speed tunnel, and a low-pressure, blowdown, high-speed tunnel. The experimental test chamber is designed to mate to either tunnel, thus two complementary sets of parameters (high-pressure, low-speed and low-pressure, high speed) can be studied separately so as to give a relatively complete description of gas flow switching. A substantial quantity of results from both tunnels have previously been reported [18], [21]; however, the most significant results from a spark gap recovery standpoint have occurred in the high-speed, blowdown tunnel. Therefore, this thesis presents gas flow data exclusively from the high-speed tunnel.

The high-speed wind tunnel is of the blowdown variety. That is, compressed air is accelerated into the switch region through an appropriate nozzle, and is then vented directly to the outside. Outside of the laboratory are storage tanks and an air compressor which

TABLE IV-1

GAS FLOW SWITCH LABORATORY

Pulsed Power System Parameters[+]

Maximum Voltage	250 kV
Maximum Switch Current	50 kA
Switch Current Pulsewidth	50 ns
Principal Pulse Forming Network	Water-Filled Coaxial Blumlein
Maximum stored energy	312.5 J
Maximum stored charge	2.5 mC
Pulse Format	Two-Pulse Burst
Minimum interpulse interval	100 μs
Maximum burst rate	0.3 pps
Pulse Regulation	3.2% Max.

[+] From Ref. [1]

are connected to the laboratory facilities by a 20.3 cm (8 in.) diameter pipe. Inside the laboratory, the pipe mates to a control valve and stagnation section, a variable Mach number nozzle section, the experimental test section, and an exhaust assembly. The exhaust assembly consists of a valve, muffler, and vent to the outside. The laboratory portions of this tunnel are illustrated in Fig. IV-3. A brief description of the tunnel's operation and significant components will now be given. A more complete description can be found in Ref. [2].

The tunnel is prepared for operation by pumping the storage tanks to nominally 100 psig with dried and filtered air. When the tanks are sufficiently pressurized, the control valve ahead of the stagnation chamber is opened. The stagnation pressure determines the specific flow velocity and test section pressure out of a range of possible values fixed by the configuration of the nozzle, test section, and exhaust valve. Therefore, special attention is devoted to keeping the stagnation pressure constant. As the storage tanks are depleted by tunnel operation, the storage pressure decreases and the operator must compensate by opening the control valve. Clearly, if the tunnel velocity is high the rate of depletion of the storage tanks is greater, and it becomes more difficult to maintain an exact stagnation pressure. This difficulty translates into an experimental error because of the corresponding fluctuations of both the flow velocity and the interelectrode pressure. Fortunately, the stagnation pressure fluctuations can generally be kept to 5% or less.

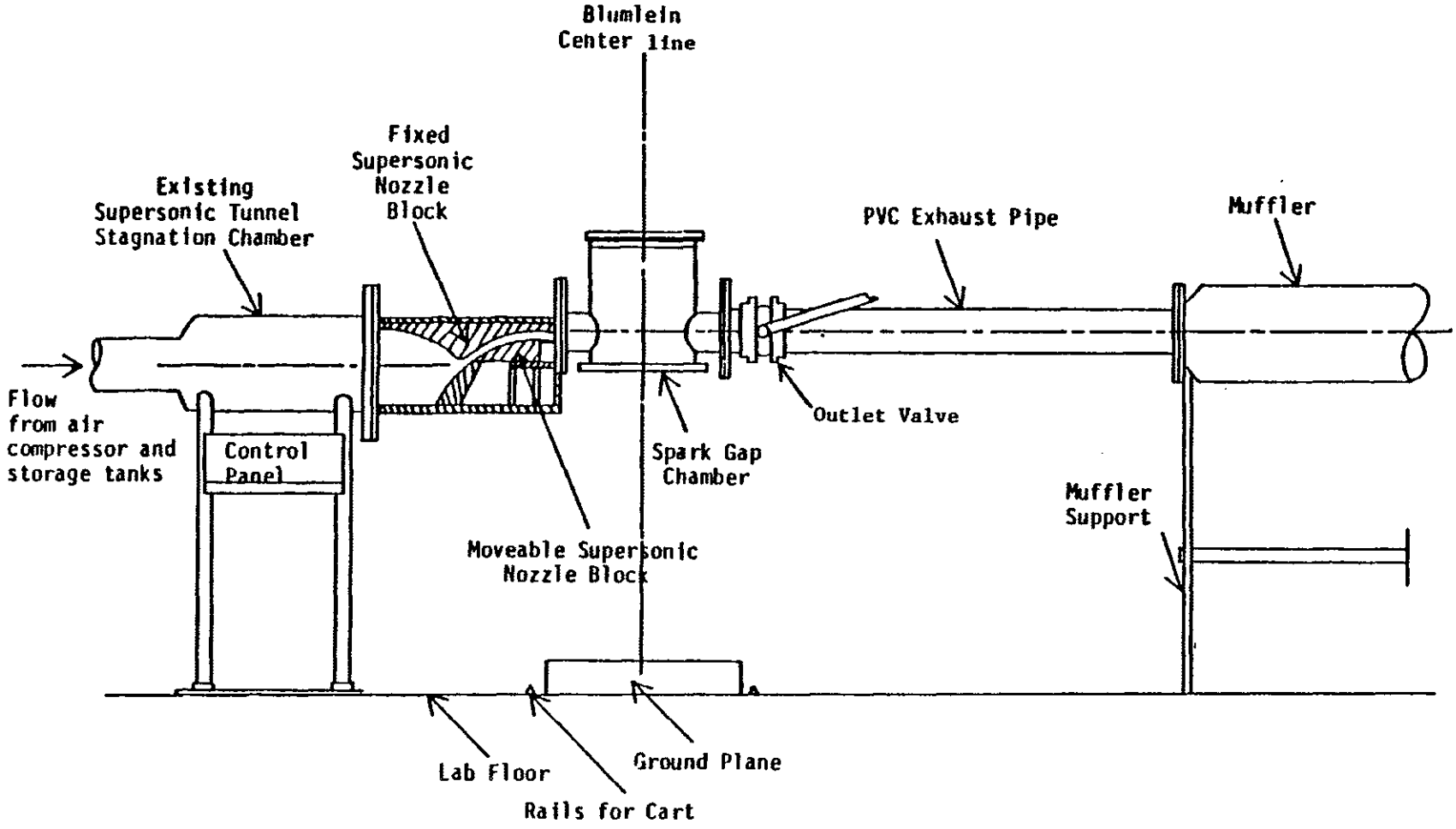

Fig. IV-3 Schematic of the supersonic, blowdown tunnel (from Ref. [2]).

As previously mentioned, the configuration of the other downstream components determines the range of possible flow conditions. The nozzle, just downstream of the stagnation chamber, is designed to produce supersonic velocities at the output that range from Mach 1 (360 m/s) to Mach 2.6 (936 m/s); however, velocities greater than Mach 1.4 have not been measured. The two-dimensional nozzle consists of an upper and a lower block. The upper block is fixed, but the lower block is movable along the flow axis. By moving the lower block with respect to the upper block, the cross-sectional area of the throat is changed, thus allowing a variety of Mach numbers to be achieved. Other parameters that change as the nozzle block is adjusted include the outlet pressure of the nozzle and the rate at which the storage tanks are depleted. The nozzle adjustment can only be done in discrete increments because a different nozzle "spacer" must be used for each nozzle setting in order to bridge the gap between the rear of the lower block and the nozzle outlet flange. This fact allows the nozzle configuration to be reset with good repeatability. Eight different nozzle spacers are available, but only three (#2, #4, and #8) are used routinely because the flow conditions that exist when they are used are well documented [2].

Another important variable that affects the flow conditions is the configuration of the electrodes. For the gas flow recovery experiments, only the electrode pair known as the "nipple-rod electrodes" at gap spacings of 1.0 cm and 1.5 cm was used. Aerodynamically the electrodes are important because their relative size and shape determine the degree the flow is disturbed by channel blockage and turbulence. In this respect, the nipple-rod electrodes are superior to

the other electrode pair known as the "hemispherical electrodes." In addition, good documentation of the interelectrode gas velocity and pressure are available with the nipple-rod electrodes [2].

Finally, the exhaust valve allows a wider range of test section pressures to be achieved at the cost of reduced flow velocity. By partially closing the valve, the flow is constricted and the pressure in the test section rises above the typical slight vacuum that exists when the valve is fully open. This, of course, allows the gas flow switch to be operated at higher voltages because the breakdown strength of the gap is improved. The cost of this pressure increase is decreased flow velocity; however, the valve has a wide range of possible settings which allows compromises between pressure and velocity. Typical velocity ranges are from 25 m/s (valve 20° open) to 525 m/s (valve fully open) and pressures of 60 psig to a few psi below atmospheric pressure, respectively. In addition, it has been noted that partial closing of the exhaust valve stabilizes the desired stagnation pressure, probably because the rate at which the storage tanks are depleted is significantly reduced. Since the valve is of the type that can only be closed in fixed 10° increments, the valve can be reliably reset to a previous setting. Once again, the gas velocity and test section pressure as a function of the exhaust valve setting have been well documented [2].

Switch Configuration

The gas flow switch mates to both the pulsed power system and the blowdown tunnel. The switch housing, which has a rectangular cross section (see Fig. IV-4), is mounted on top of the Blumlein as indicated in Fig. IV-5. The switch housing is contained in a pressure vessel

called the test chamber. The in-line electrodes are mounted vertically, with the bottom electrode connected to the Blumlein and the top electrode mounted to an aluminum plate. The plate is securely held on top of the insulating furane switch housing by eight brass, current return rods. The switch current is conducted from the high-voltage connection penetrating the Blumlein's furane insulator to the Blumlein's outer aluminum conductor which is held at ground potential. The gas flow is directed perpendicular to the electrode axis (as indicated in Fig. IV-4) by a 5.1 cm by 7.6 cm rectangular flow channel so that the interelectrode volume may be swept free of arc debris. The flowing gas is conducted to, and removed from, the switch housing by smoothly contoured flow channels.

Optical access to the spark gap volume is along an axis perpendicular to the electrodes and the flow axis. This access is obtained by two windows mounted on either side of the flow channel (see Fig. IV-4). The windows are designed such that they mount flush with the inside of the flow channel wall so that no appreciable disturbance of the gas flow results. One of the windows is made of fused quartz with a cutoff wavelength below 300 nm so that photons from a UV source located outside of the switch housing may propagate into the spark gap region to produce photoionization.

As has been previously mentioned, two different electrode configurations have been used in this work. They are called the nipple-rod electrode pair and the hemispherical electrode pair. While only the nipple-rod electrodes were used in the gas flow recovery experiments, the hemispherical electrodes gave useful information in the modeling of pulse-charged breakdown characteristics. The

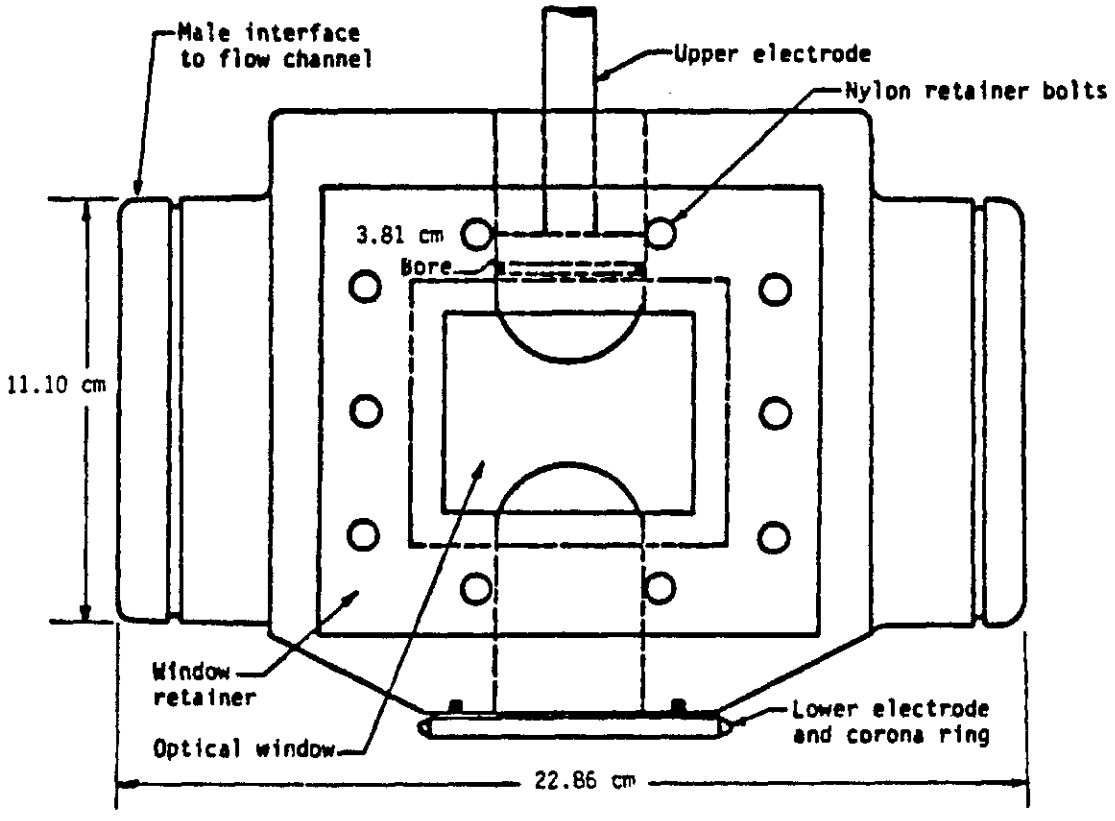

Fig. IV-4 Side view of the switch housing showing the hemispherical electrodes (from Ref. [1]).

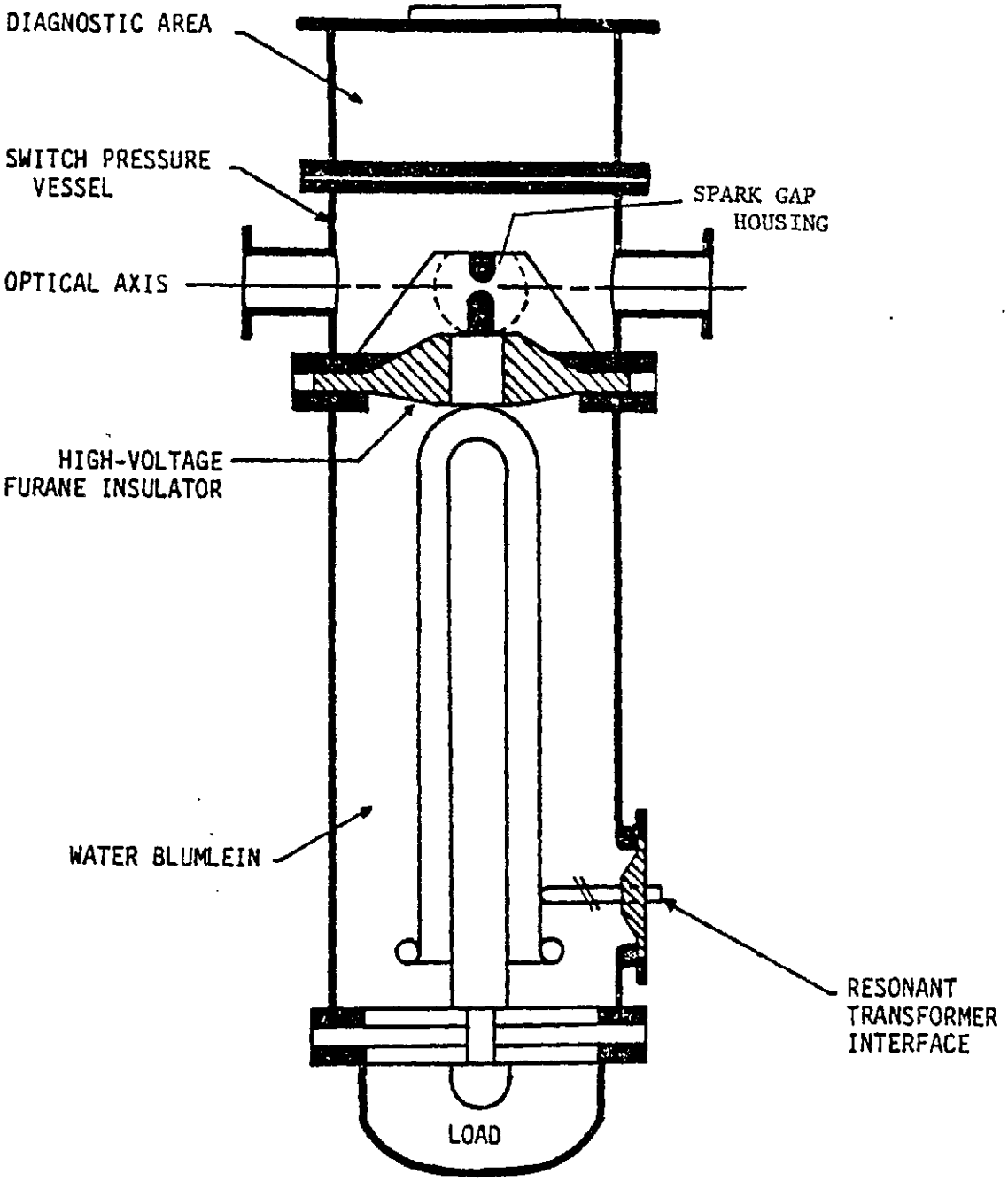

Fig. IV-5 Position of the pressure vessel and switch housing with respect to the water Blumlein (from Ref. [2]).

nipple-rod electrodes consist of a lower electrode that has a 3.81 cm brass body contoured to a nipple with an approximate radius of 0.48 cm and an upper electrode made of a .95 cm diameter brass rod. The rod is set in a 3.81 cm diameter acrylic plug and is rounded on one end with a radius approximately the same as the companion nipple of the bottom electrode. As shown in Fig. IV-6, the lower electrode is rigidly secured to the top of the Blumlein, while the upper electrode is screw mounted into the supporting aluminum plate so that the gap spacing can be adjusted. The nipple of the bottom electrode just extends into the flow channel of the switch housing while the top electrode extends as far into the flow channel as is necessary to obtain the desired gap spacing.

The hemispherical electrodes are mounted in the same manner as the nipple-rod electrode pair; however, both of the hemispherical electrodes are made of 3.81 cm diameter brass rod rounded on the ends to a radius of 1.27 cm as shown in Fig. IV-7. Both the upper and lower electrodes extend into the flow channel; this, coupled with their larger radius, give the hemispherical electrodes less desirable aerodynamic qualities as compared to the nipple-rod electrodes. As a result, the hemispherical electrode pair was not used in the gas flow experiments; however, because the hemispherical electrodes have a smaller field enhancement factor, they were used in the pulsed breakdown experiments.

Two-Pulse Preionizer

The statistical delay was minimized by preionization produced by a radiation source. The device produces two pulses of UV illumination that coincide with the first and second pulses applied to the switch.

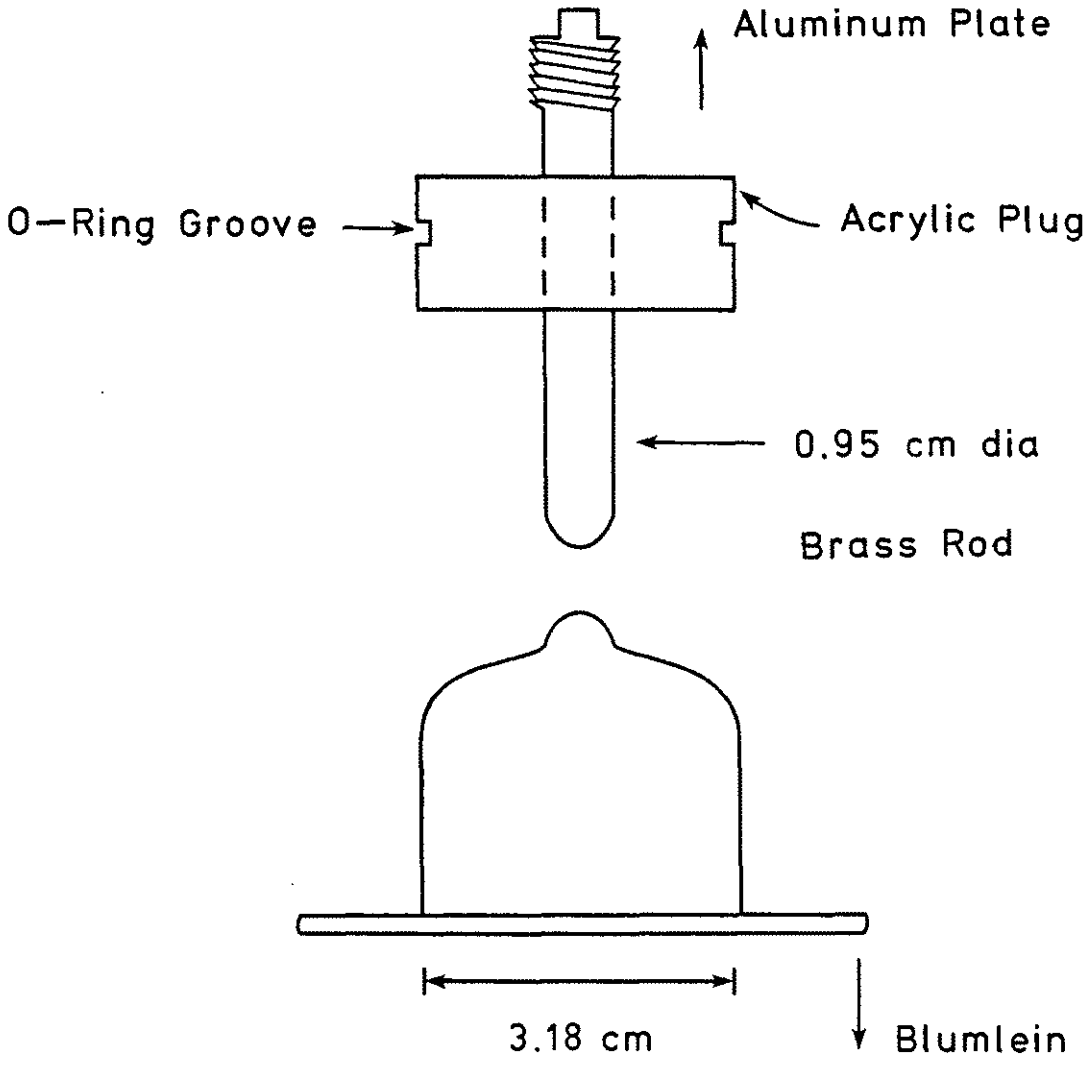

Fig. IV-6 Diagram of the nipple-rod electrodes.

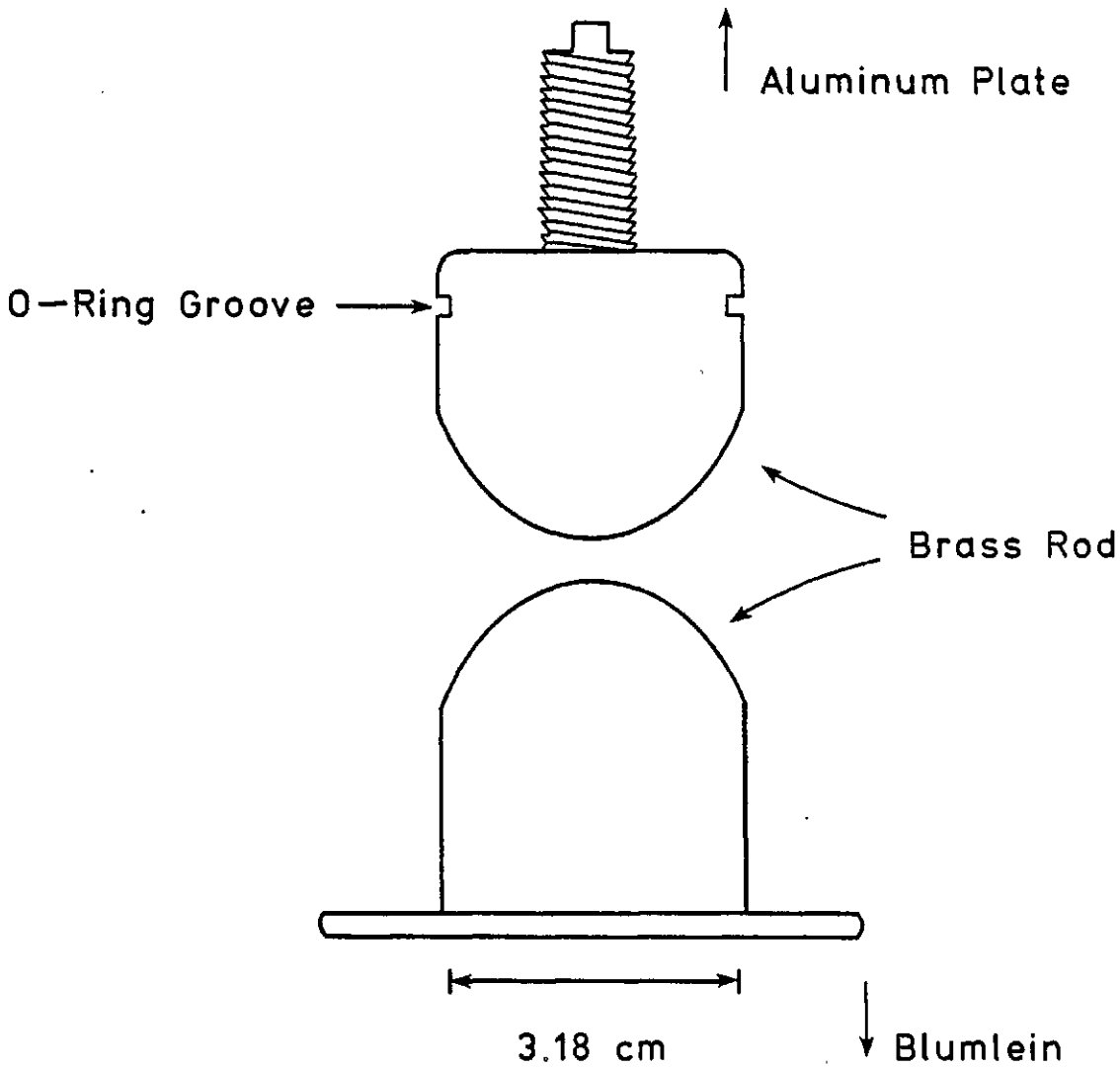

Fig. IV-7 Diagram of the hemispherical electrodes.

The system is capable of producing two almost identical pulses with interpulse spacings as small as 100 μs. In addition, the preionization pulse may be advanced or delayed in time with respect to the switch pulse to ensure that a sufficient level of preionization is available.

Preionizer Operation

Referring to Fig. IV-8, the two-pulse preionizer consists of two identical capacitive discharge systems that feed the two-winding primary of an air-core pulse transformer. The secondary circuit consists of a single winding feeding a center-fire, resistor-type spark plug. To form the initial pulse, one of the capacitive discharge circuits is discharged through its corresponding primary winding which is coupled to the spark plug by the secondary winding. The second pulse is similarly produced. Because the two primary windings are counter wound with respect to each other, they both produce a pulse of the same polarity in the secondary.

The primary circuits are formed by simple RLC networks switched by FX2508 hydrogen thyratrons. The energy storage capacitors are resistively charged by a single dc power supply to about 12 kV with a charging time of approximately 10 seconds. The circuit components have been chosen such that the thyratron currents are slightly overdamped. The first primary winding couples to both the second primary winding and the secondary winding. Because the second primary winding is counter wound with respect to the first primary winding, an opposing potential is induced across it. This negative potential cancels the voltage across the second thyratron, thereby significantly reducing the possibility of sympathetic false triggering of the second thyratron.

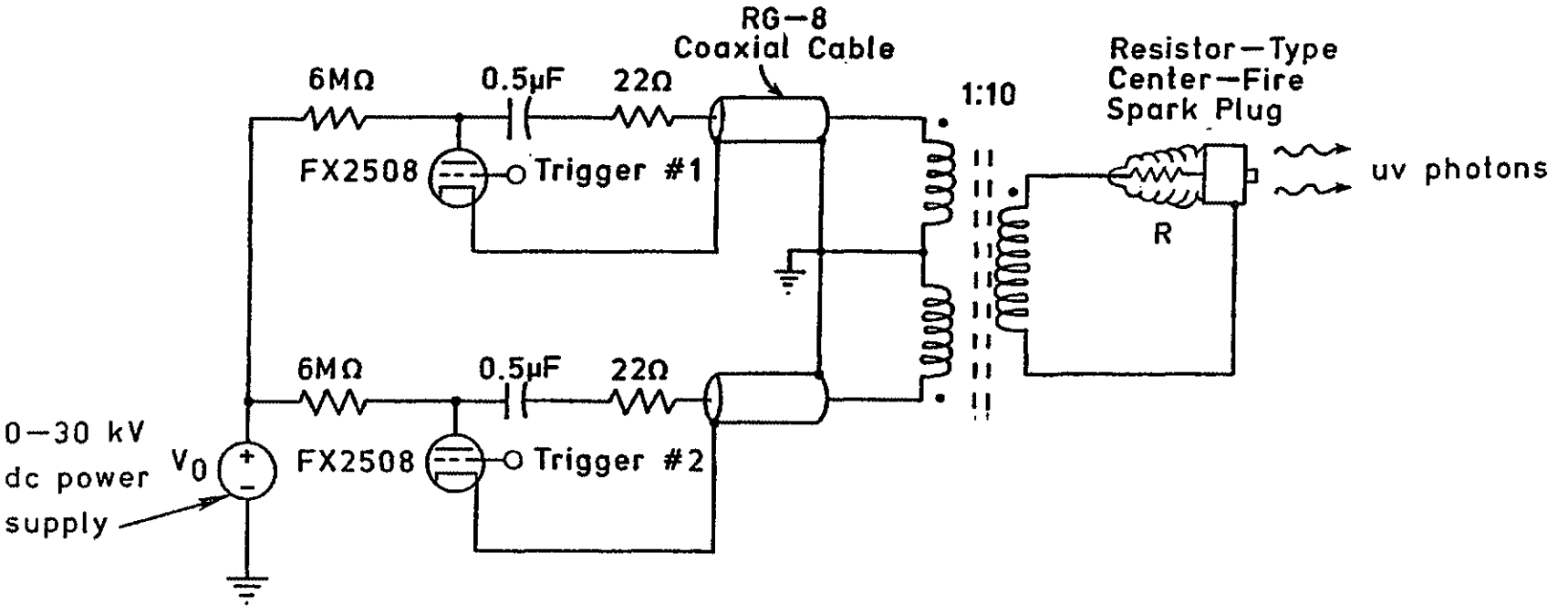

Fig. IV-8 Schematic diagram of the two-pulse preionizer.

In the secondary circuit, the voltage pulse is stepped up by a 1:10 turns ratio; however, because of the low coupling between the primary and the secondary, only a factor of two amplification occurs. When the self-breakdown strength of the spark plug is reached, it breaks down producing a surface arc of approximately 2 mm in length. The arc produces radiation over a broad spectrum, including the soft and hard UV. The spark plug assembly is located in the test chamber and is mounted behind a quartz window (see Fig. IV-9) so that the spark plug may illuminate the electrodes without disturbing the gas flow inside of the switch housing. All other equipment, including the pulse transformer, is positioned outside of the test chamber; electrical connection to the spark plug is provided by a pressure sealed electrical connection penetrating the test chamber bulkhead.

Preionizer Performance

Figures IV-10 and IV-11 are oscilloscope photographs of the first pulse primary current for a test chamber pressure of 0 psig and 50 psig, respectively. At $p = 0$ psig, the primary current peaks at about 560 A, and the spark plug pressure has very little effect on the primary circuit. In addition, there is an absence of distortion in the primary current waveform due to the breakdown of the plug in the secondary which is a result of the low coupling between the two windings. Figure IV-12 demonstrates the excellent regulation of the two primary current pulses at an interpulse spacing of 100 μs. The percent difference between the two waveforms is less than 1%. Comparable results are obtainable at longer interpulse spacings as well. The primary winding voltage peaks at about 12 kV. Both the

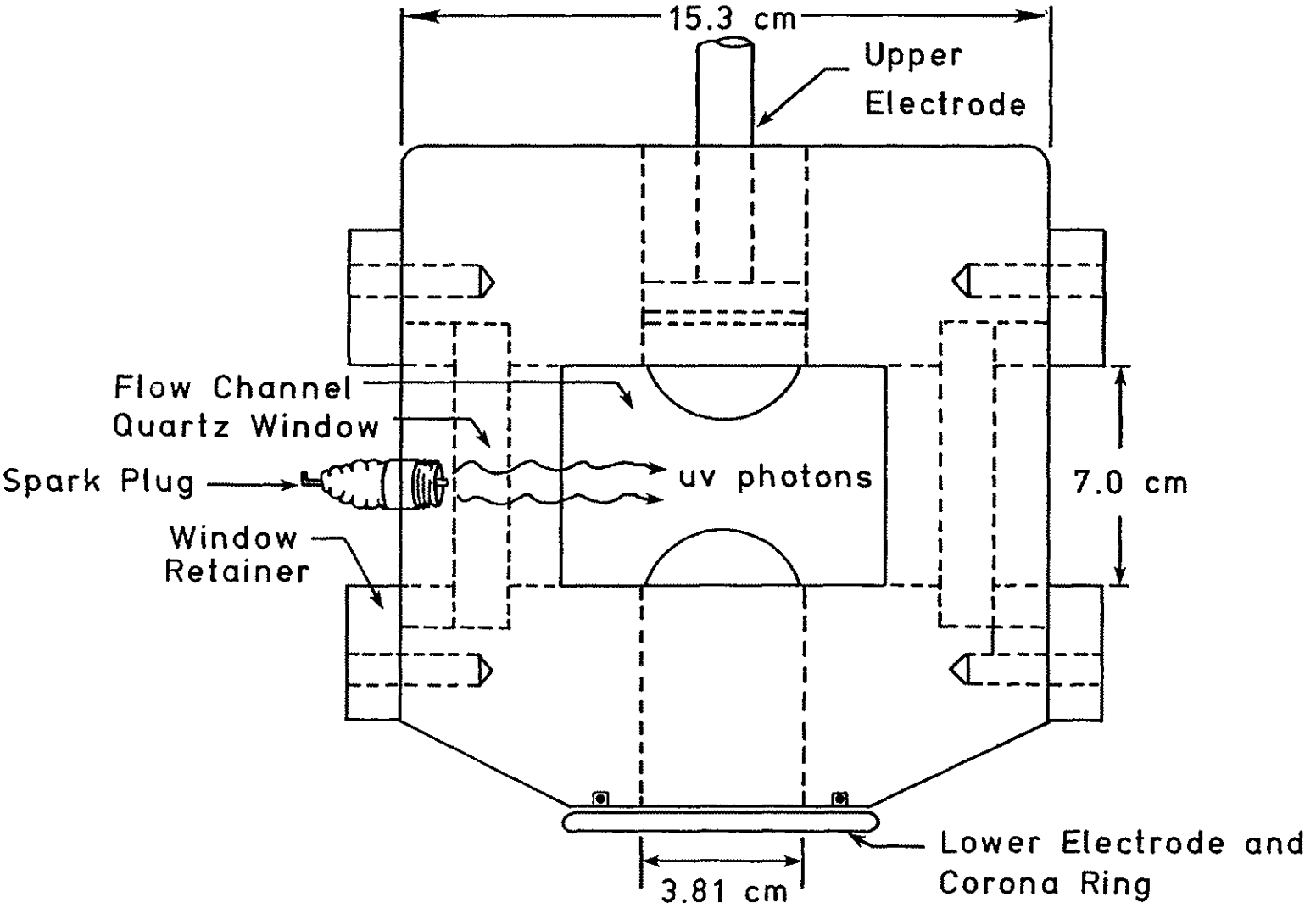

Fig. IV-9 End view of switch housing showing spark plug position.

100 A/div

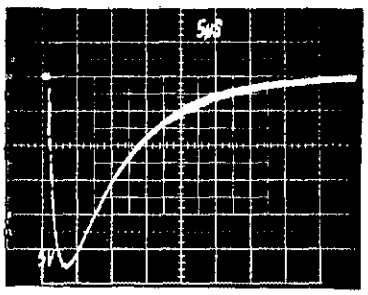

5 μs/div

Fig. IV-10 Oscilloscope photograph of primary current at p = 0 psig.

100 A/div

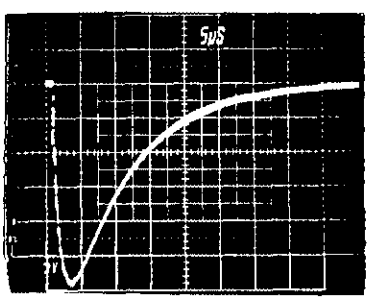

5 μs/div

Fig. IV-11 Primary current at p = 50 psig.

current and voltage waveforms are predictable using a simple RLC network model, attesting to the low coupling between the windings.

The secondary voltage rapidly rises until the breakdown strength of the spark plug is reached, then the secondary voltage collapses to the arc maintenance potential. As expected, the breakdown strength of the spark plug is a function of pressure: the peak voltage at a pressure of 0 psig is 4.4 kV, while the peak voltage at 50 psig is 10.4 kV. The secondary current, after breakdown, was reliably measured using a commercial current transformer. Figures IV-13 and IV-14 demonstrate the secondary current at two different pressures. In contrast to the secondary voltage, the current shows no noticeable dependence on pressure. This is because the secondary current is primarily controlled by the large leakage inductance of the pulse transformer secondary and the spark plug resistance, not the low-impedance arc itself.

This current is also overdamped and has a peak value of 60 A, a risetime of 1 μs, and a pulsewidth of 24 μs. Again, the secondary current has excellent regulation, even at short interpulse spacings as demonstrated by Fig. IV-15. In this oscilloscope photograph, two virtually identical current pulses separated by 100 μs are shown. From this photograph, it is concluded that both voltage pulses applied to the gas flow switch are accompanied by equal doses of UV illumination regardless of the repetition rate of the switch.

The illumination intensity of the spark has been measured using a photomultiplier tube. Figure IV-16 is a photograph illustrating the total light output of the spark at atmospheric pressure versus time. Clearly the temporal character of the light intensity is very similar

100 A/div

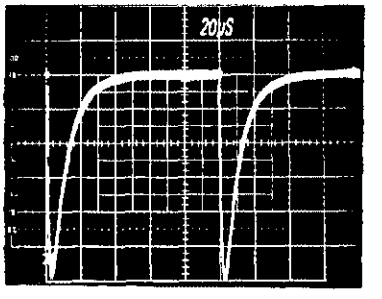

20 µs/div

Fig. IV-12 Primary current regulation for an interpulse time of 100 µs.

20 A/div

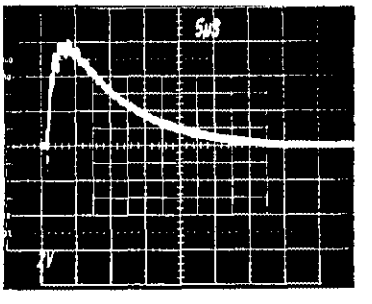

5 µs/div

Fig. IV-13 Secondary current at p = 0 psig.

20 A/div

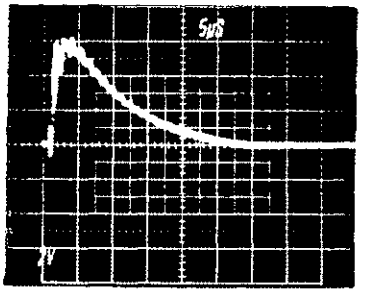

5 μs/div

Fig. IV-14 Secondary current at p = 50 psig.

20 A/div

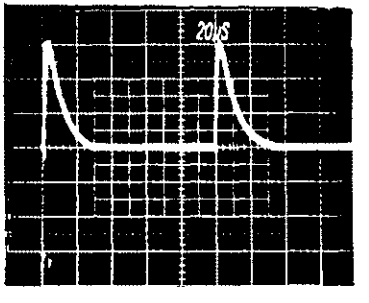

20 μs/div

Fig. IV-15 Secondary current regulation for an interpulse time of 100 μs.

Arbitrary scale

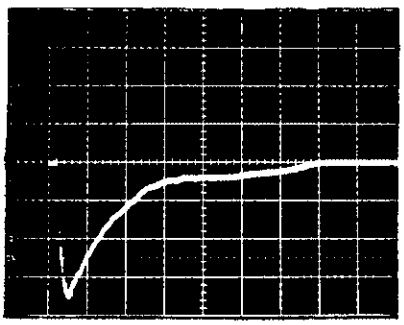

5 μs/div

Fig. IV-16 Illumination intensity of spark at p = 0 psig.

to that of the spark current. The light intensity has a sharper peak but the risetimes and pulse widths are virtually identical. The tail of the light intensity is not exponential but somewhat flattened due to the recombination radiation from the deionizing spark channel. The spectrum of the light has not been measured, but the response of the tube corresponds to a S-11 spectrum encompassing only the visible and soft UV.

The spectral response of the bare spark depends on gas and current density [29] as well as pressure. Since UV photons are emitted only by molecules excited to the higher energy states, it is expected that the UV component of the spark emission is significant only during the hotter, high-current phase of conduction, falling off rapidly as the current diminishes. This correlates well with the observation that the best preionizer performance was obtained when the preionizer and the switch chassis thyratrons were triggered at the same time. After the switch chassis thyratrons are triggered, the switch voltage reaches breakdown strength in about 2 to 5 μs, which brackets the peak in the light intensity as illustrated in Fig. IV-16.

It is well established that the UV component of the spectrum is most responsible for photoelectron production. However, the actual ionization process is probably not one-photon ionization of the major gas components. This is because the ionization cross sections of the major components of air are too small in the soft UV (200 nm to 400 nm) [33]. Since it was found that reduction of the statistical delay occurred when the spark illumination was conducted through a quartz window with a cutoff wavelength just above 200 nm but did not occur when the illumination was conducted through an acrylic window

capable of visible light transmission only, it is concluded that this soft UV spectrum is responsible for the photoelectron production. In fact, this observation has been made by other researchers who have shown that photoelectron production is most likely a result of photoionization of organic impurities in the gas [29].

Diagnostics

The switch voltage was monitored on a storage oscilloscope through a resistive voltage divider connected to the output (secondary) of the resonant transformer. The output of the resonant transformer is connected to the middle conductor of the Blumlein which is in turn connected directly to the switch. Since the breakdown voltage of the switch is taken as the maximum charging voltage before it collapses, only the relatively slow charging waveform needed to be monitored. The risetime of the resistive divider is adequate for this purpose.

The complete charging waveform is best described as a skewed, 1-cosine curve that goes through a negative peak first and then through a larger positive peak [1]. However, it was desired to have a linear rising ramp voltage for theoretical reasons; therefore, the charging voltage was selected adequately large so that the switch broke down on the first part of the curve, which approximates a ramp voltage. A typical voltage waveform as measured using the resistive divider is shown in Fig. IV-17. This particular photograph indicates a breakdown voltage (the peak value) of 91 kV and a rate of rise of the voltage of approximately 23 kV/μs.

The switch current was not monitored continuously during these experiments because it has been found that recovery is not a strong function of spark current. However, the switch current has been

measured using a fast Rogowski current probe [2]. Figure IV-18 shows a typical switch current waveform measured using the Rogowski probe. Although an ideal Blumlein current waveform should be a square pulse, this curve is clearly more like a second order underdamped response. This discrepancy is a consequence of the large stray inductance of the Blumlein high voltage insulator that mates the Blumlein to the bottom electrode of the switch [2].

During the static breakdown tests, pressure was measured either with an MKS Baritron pressure transducer or a diaphragm pressure gauge calibrated with the MKS transducer. Combined experimental and measurement error was never more than $\pm$ 0.5 psig. The stagnation and test section pressures during the gas flow experiments were measured using good quality diaphragm pressure gauges; however, the experimental error caused by the depletion of the storage tanks was typically $\pm$ 2 psig, except for pressures below atmospheric which were measured somewhat better. Finally, most measurements were made with air, but those measurements made in nitrogen were preceded by an evacuation of the test chamber to about 5 torr to remove the air. The chamber was then filled to the desired pressure, as measured using the MKS Baritron transducer, with commercial grade nitrogen.

22.5 kV/div

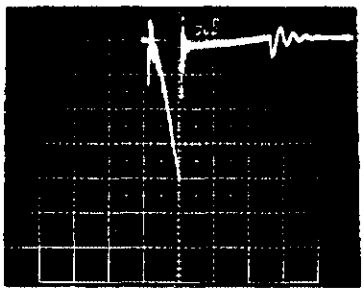

5 μs/div

Fig. IV-17 Blumlein switch voltage as measured with resonant transformer resistive probe.

9.6 kA/div

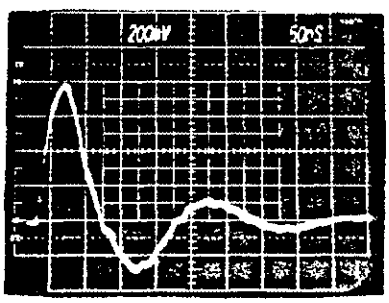

50 ns/div

Fig. IV-18 Switch current as measured with Rogowski probe.

CHAPTER V

RECOVERY RESULTS

In this chapter the results of static and gas flow two-pulse recovery experiments will be presented. The nipple-rod electrodes were used exclusively in all of these measurements because the flow conditions (gas velocity and pressure) are best known with this electrode pair. In addition, the nipple-rod electrodes result in the least flow blockage and turbulence; therefore, the highest gas velocities can be achieved. Gas flow results were acquired over a representative range of velocities from 25 m/s to 360 m/s.

For each combination of velocity, gap spacing, and pressure the effect of preionization will be demonstrated by presenting recovery results with and without two-pulse UV illumination. When available, the static dc and pulse-charged breakdown voltage under the same conditions of pressure and gap spacing will be indicated to illustrate the relationship between the recovery and breakdown characteristics of the spark gap.

Static Recovery Results

Figures V-1 and V-2 demonstrate recovery for a 1.0 cm gap with no gas flow (static) at a pressure of 48 psig in air. Figure V-1 is without preionizing UV illumination while Fig. V-2 is with preionization. Both the first pulse and the second pulse breakdown

voltage are indicated on these graphs. Each data point in both figures is an average of 20 pulses, thus the mean value is indicated by a symbol and plus/minus one standard deviation is indicated by the error bars.

The second pulse recovery curve in Fig. V-1 is similar to the idealized curve shown in Fig. III-12. The four different domains are clearly illustrated in the second pulse data. For example, the knee of the recovery curve is easily identifiable. The knee always has a definitive slope indicating a continuous recovery mechanism (cooling) but large standard deviations resulting from the turbulent nature of this recovery.

For this data, initial recovery occurs for an interpulse time of about 5 ms after which the distinctive plateau begins. In this region the breakdown voltage is very deterministic and stable at about 104 kV. As indicated on the graph, this voltage matches the breakdown voltage reported in Chapter III for this electrode configuration and pressure when preionization is applied first. Clearly the plateau represents recovery to the good-gap regime.

At about 40 ms, the standard deviation and the mean breakdown voltage for the second pulse in Fig. V-1 begins to increase again. The first pulse breakdown voltage represents the statistically delayed regime ranging between 120 kV and 150 kV, in agreement with the expected value indicated. It is evident that the second pulse breakdown voltage, within statistical scatter, increases toward this range and eventually reaches it. For times greater than 100 ms, the second pulse is indistinguishable from the first pulse, thus final recovery has occurred.

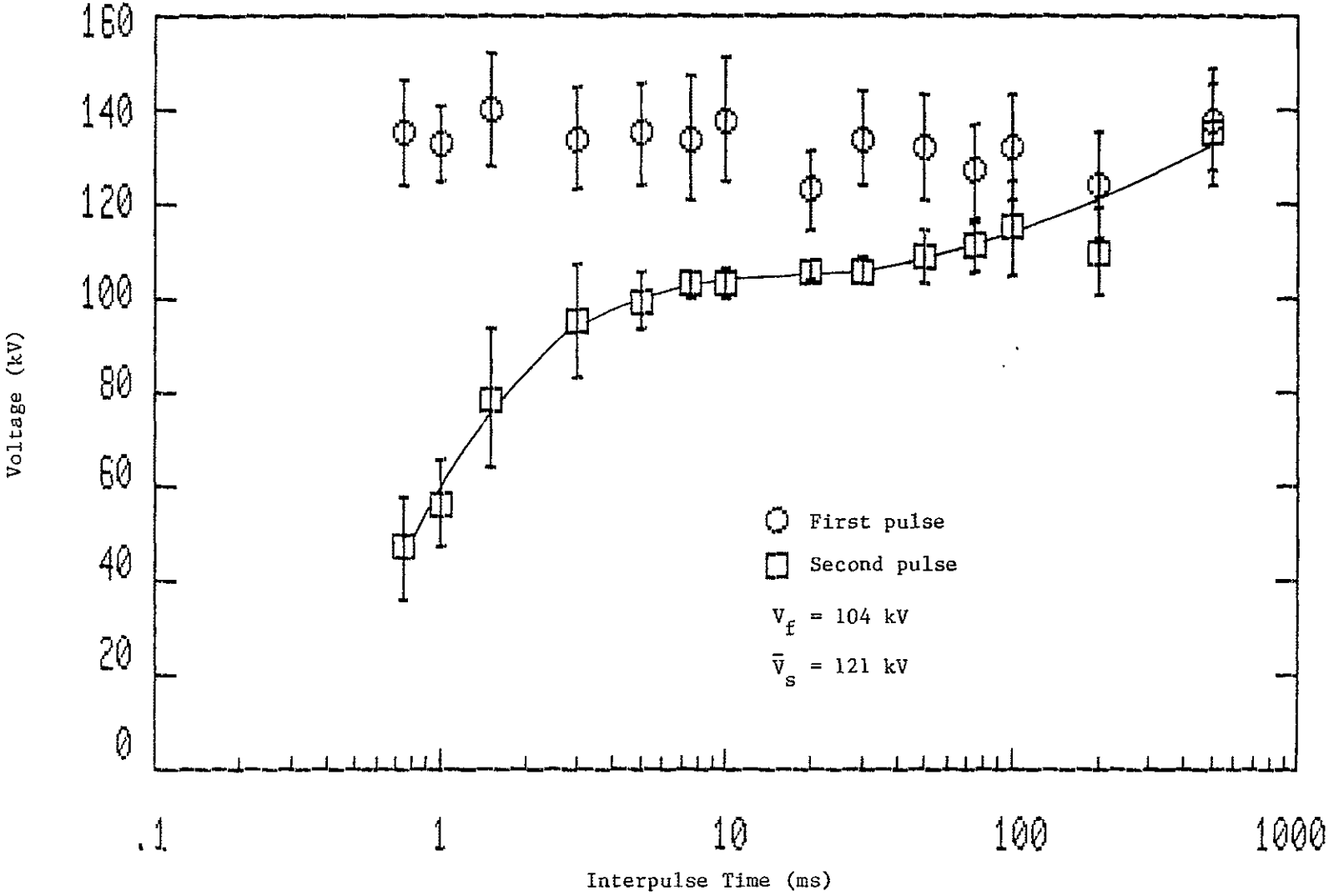

Fig. V-1 Static recovery of the nipple-rod electrodes without preionization, d = 1.0 cm, air, p = 48 psig. V_f is the formatively delayed breakdown voltage at this pressure and gap spacing (from Chapter III) while $\bar{V}_s$ is the corresponding statistically delayed breakdown voltage.

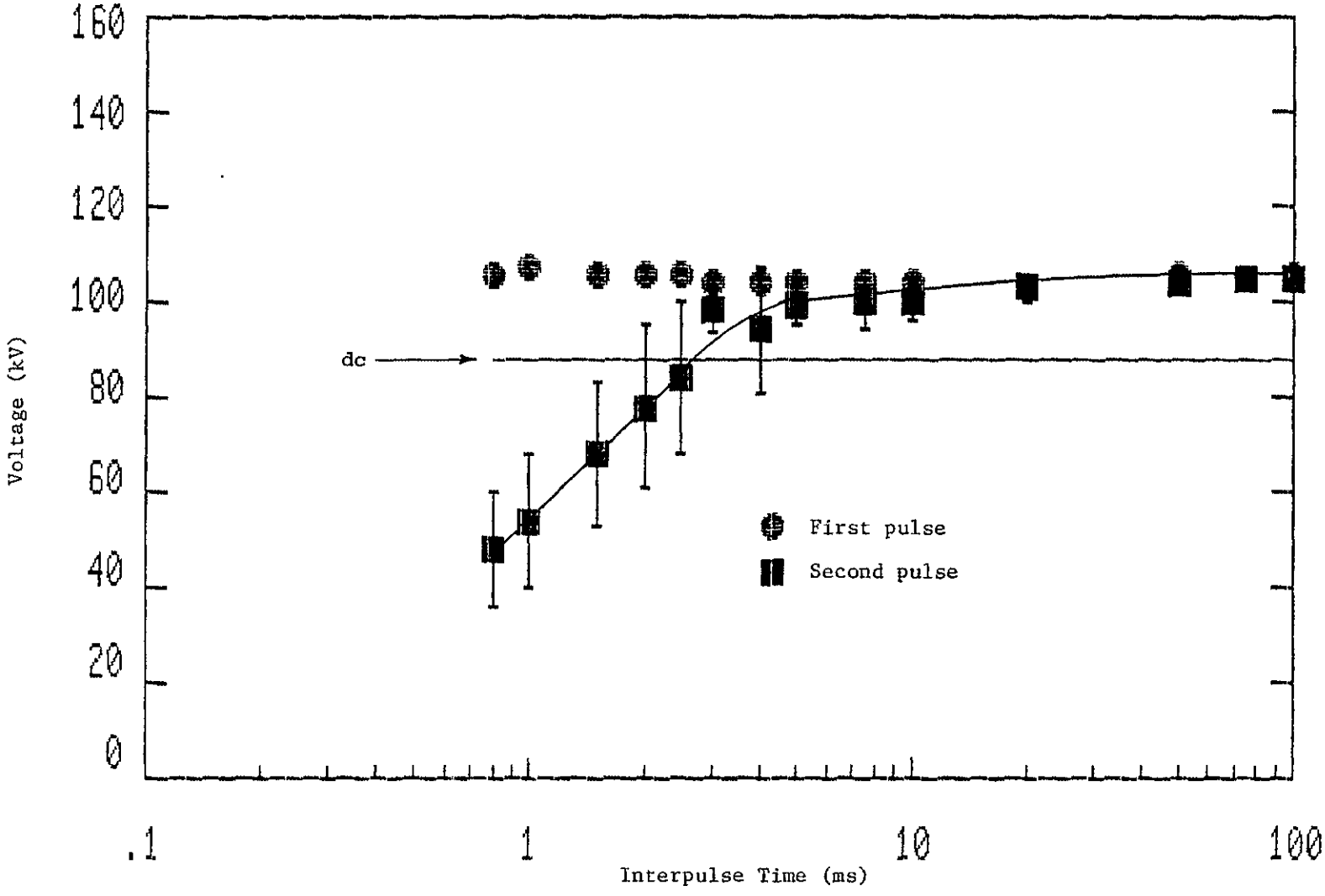

Fig. V-2 Static recovery of the nipple-rod electrodes with preionization, d = 1.0 cm, air, p = 48 psig.

Figure V-2 demonstrates recovery for this same electrode configuration and pressure but with UV illumination applied before both the first and second pulses. The knee of the curve is virtually unaffected by the preionization, and the initial recovery and plateau occur as in Fig. V-1. One may note that the plateau does not occur at the dc strength of the gap which is consistent with the previously described pulse-charged breakdown model. However, the first pulse now breaks down at the level given by the plateau and exhibits the same characteristic stability. As a result, the transition region has been eliminated because initial recovery now corresponds to 100% recovery of the gap's breakdown strength. In addition, the coincidence of the plateau with the breakdown levels produced with external preionization supports the assumption that mechanisms for self preionization are equivalent in effect to external mechanisms (UV illumination).

Gas-Flow Recovery Results

When gas flow is introduced into the spark gap, results qualitatively similar to the static recovery data are obtained. This finding is quite significant because it indicates that clearing the major portion of the spark gap volume does not suppress the mechanism responsible for the plateau. However, the characteristic times required to obtain both initial and final recovery are functions of the free stream gas velocity, as should be noted in the following results.

The recovery results for a gas-blown, 1.0 cm nipple-rod gap with air velocities of 25 m/s (Mach 0.08), 85 m/s (Mach 0.24), and 225 m/s (Mach 0.62) are presented in Figures V-3 through V-8, respectively. In these figures, the data points represent an average of the breakdown voltages of 10 pulses. Figures V-3, V-5, and V-7 indicate the recovery

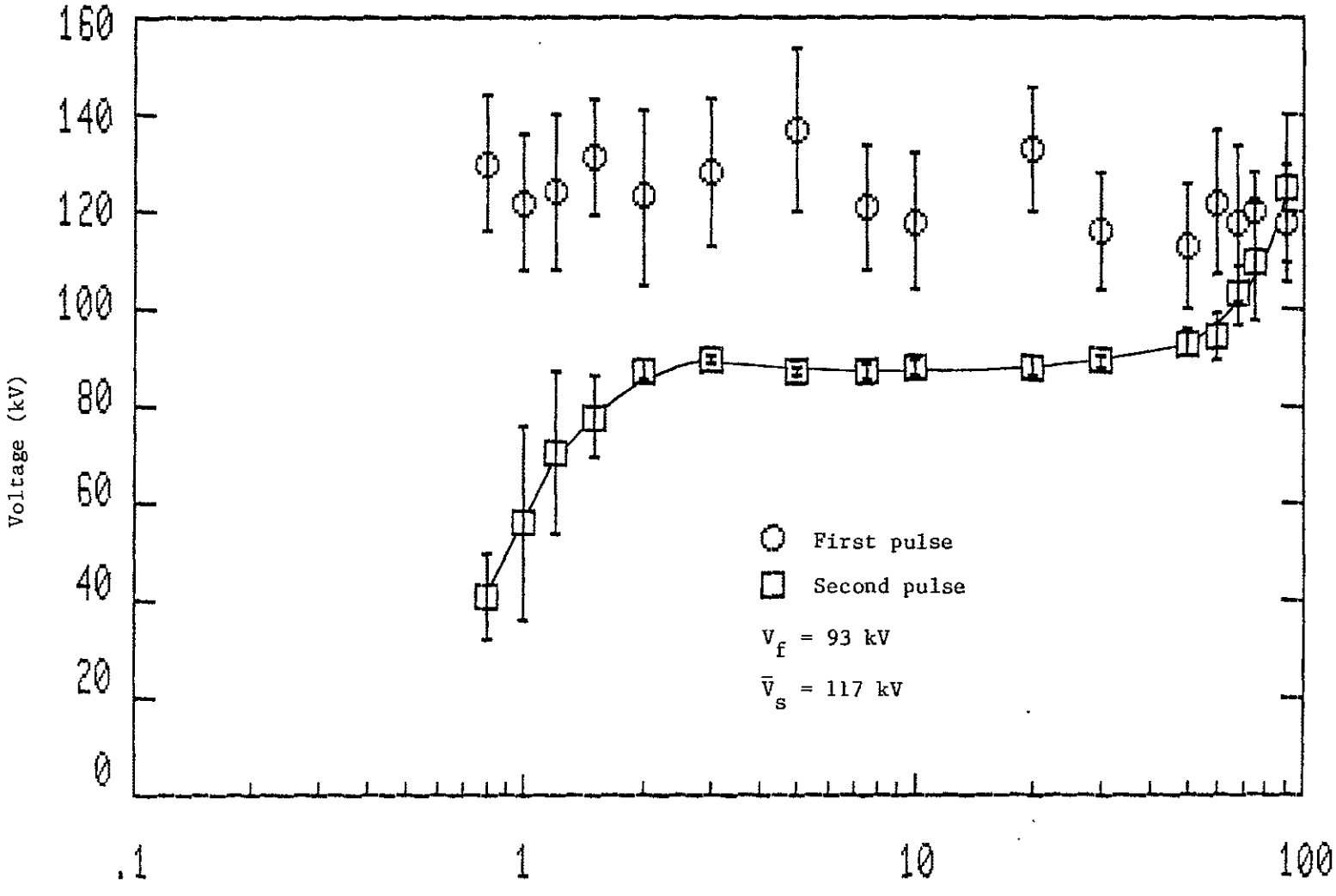

Fig. V-3 Gas-flow recovery of the nipple-rod electrodes without preionization, U = 25 m/s (Mach 0.08), d = 1.0 cm, air, p = 40 psig, Spacer #2, p_{stag} = 41 psig, valve 20° open.

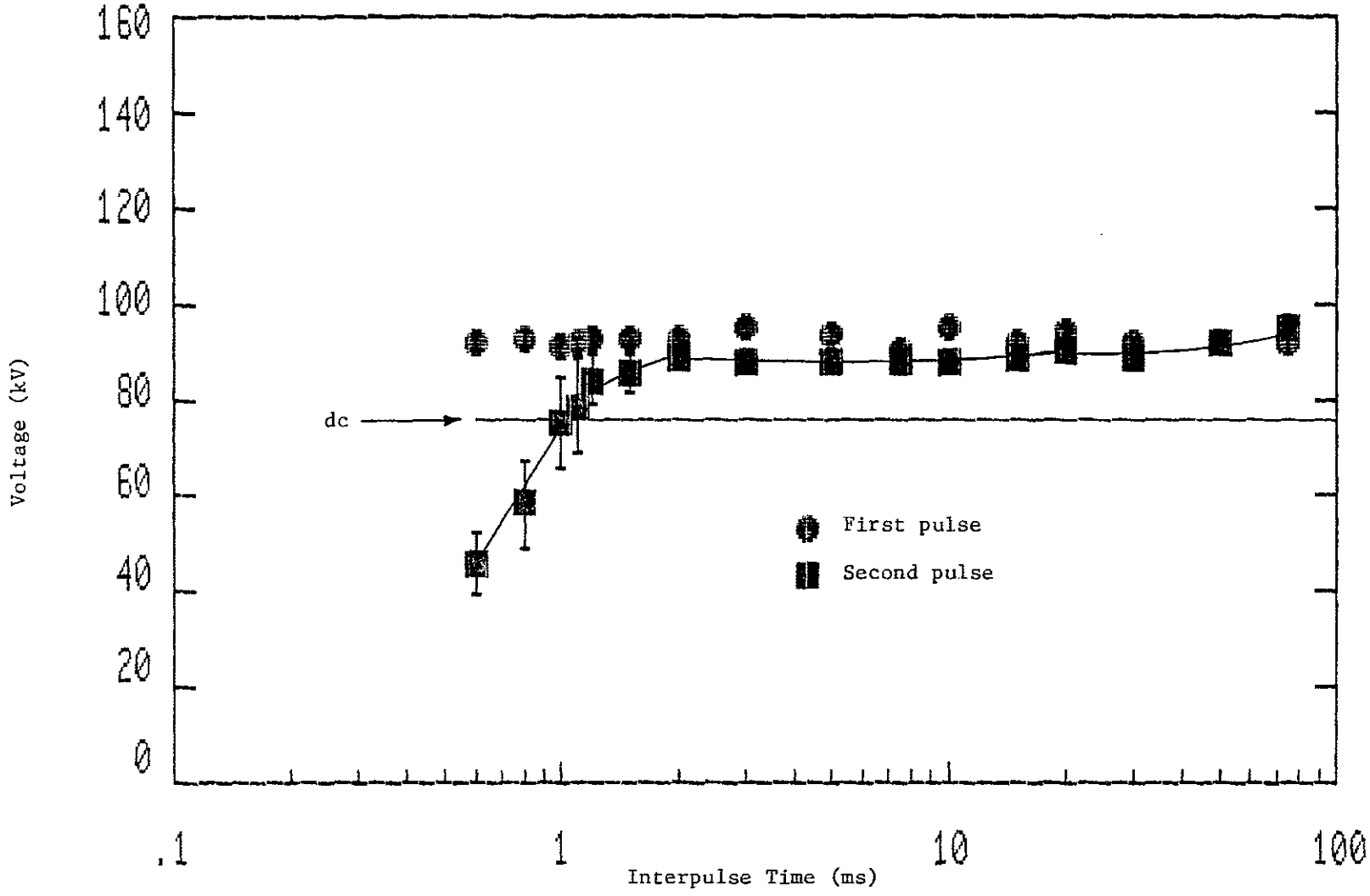

Fig. V-4 Gas-flow recovery of the nipple-rod electrodes with preionization, U = 25 m/s, d = 1.0 cm, air, p = 40 psig, Spacer #2, p_{stag} = 41 psig, valve 20° open.

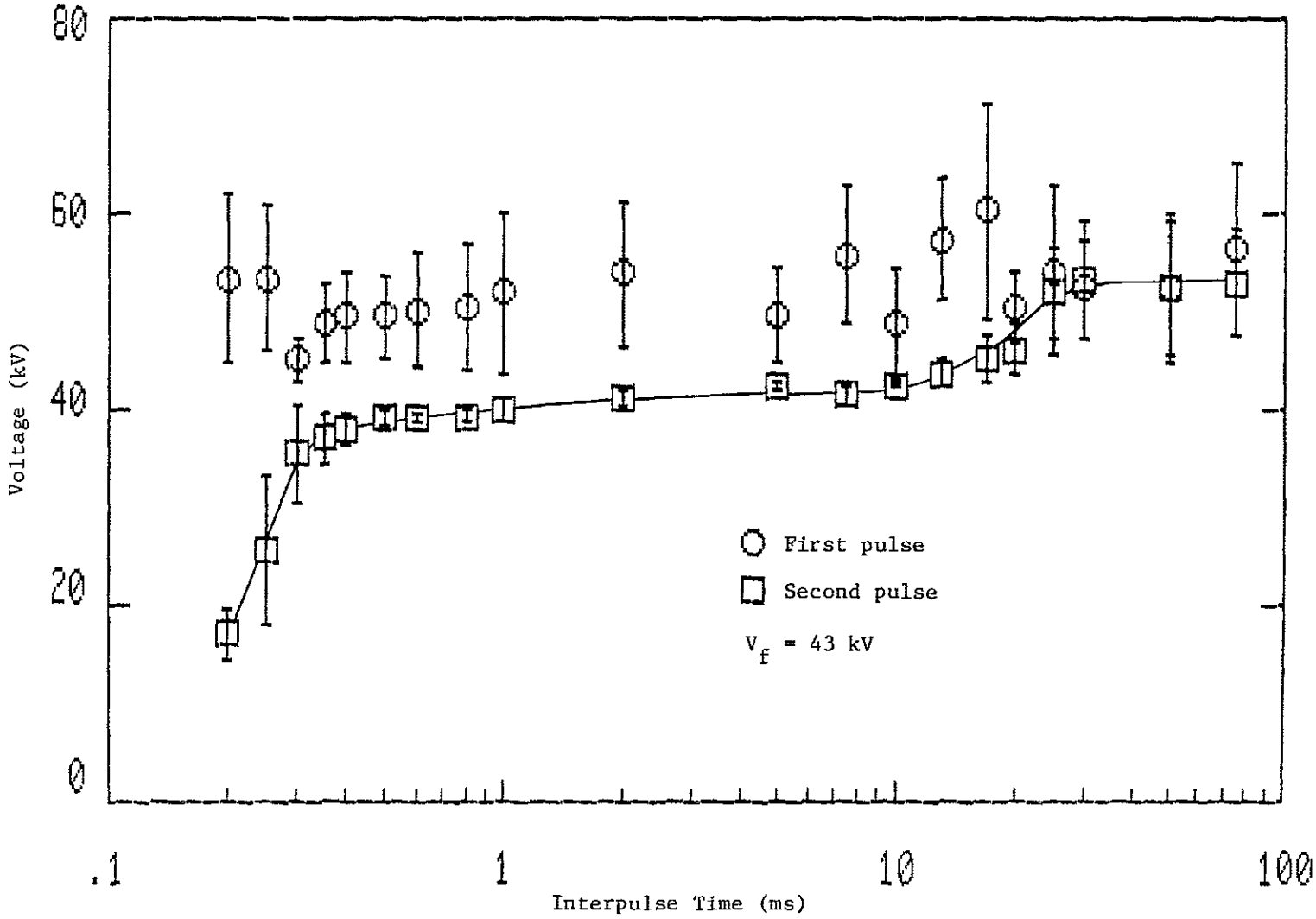

Fig. V-5 Gas-flow recovery of the nipple-rod electrodes without preionization, U = 85 m/s (Mach 0.24), d = 1.0 cm, air, p = 5 psig, Spacer #2, p_{stag} = 33 psig, valve 30° open.

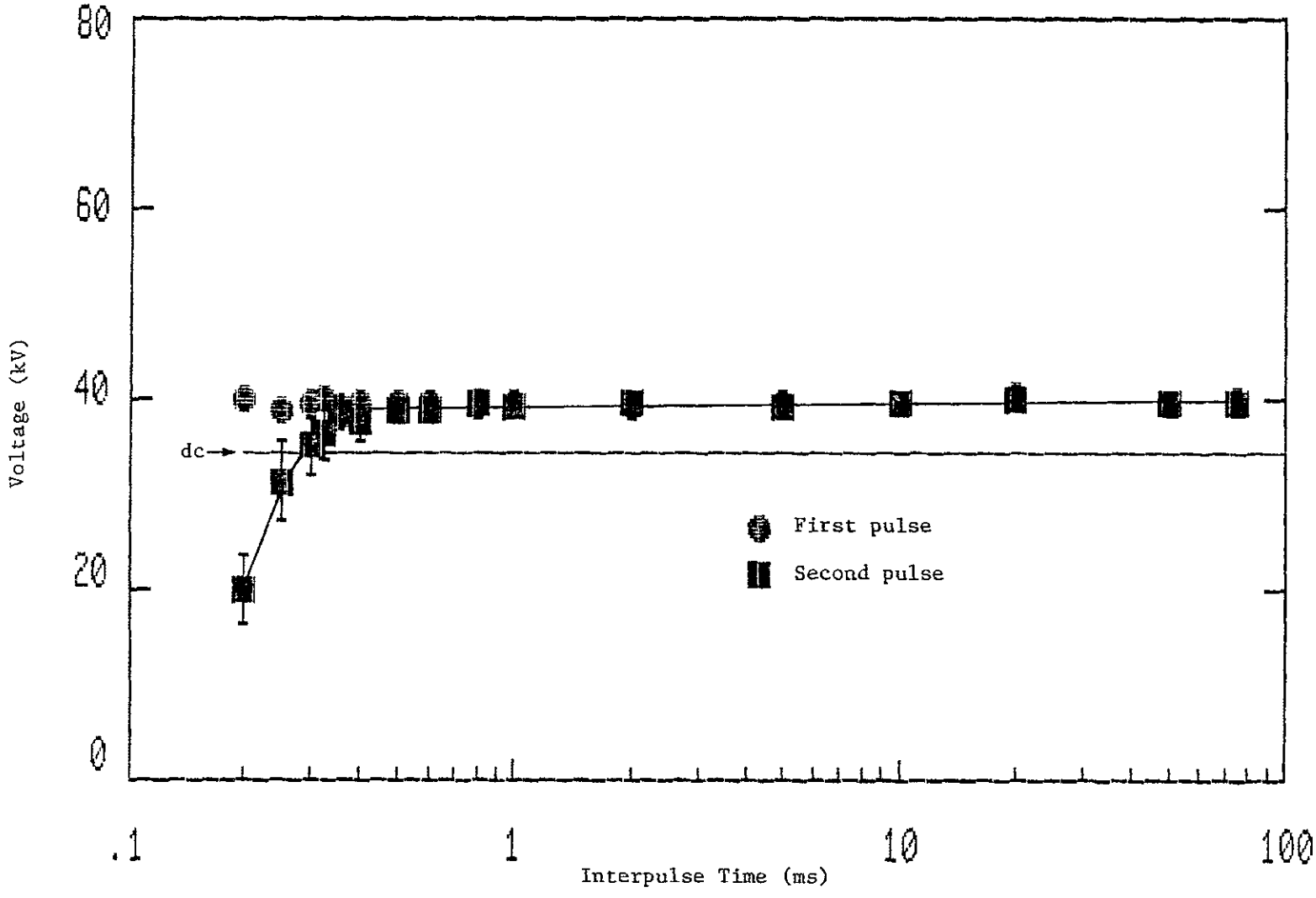

Fig. V-6 Gas-flow recovery of the nipple-rod electrodes with preionization, U = 85 m/s, d = 1.0 cm, p = 5 psig, Spacer #2, p_{stag} = 33 psig, valve 30° open.

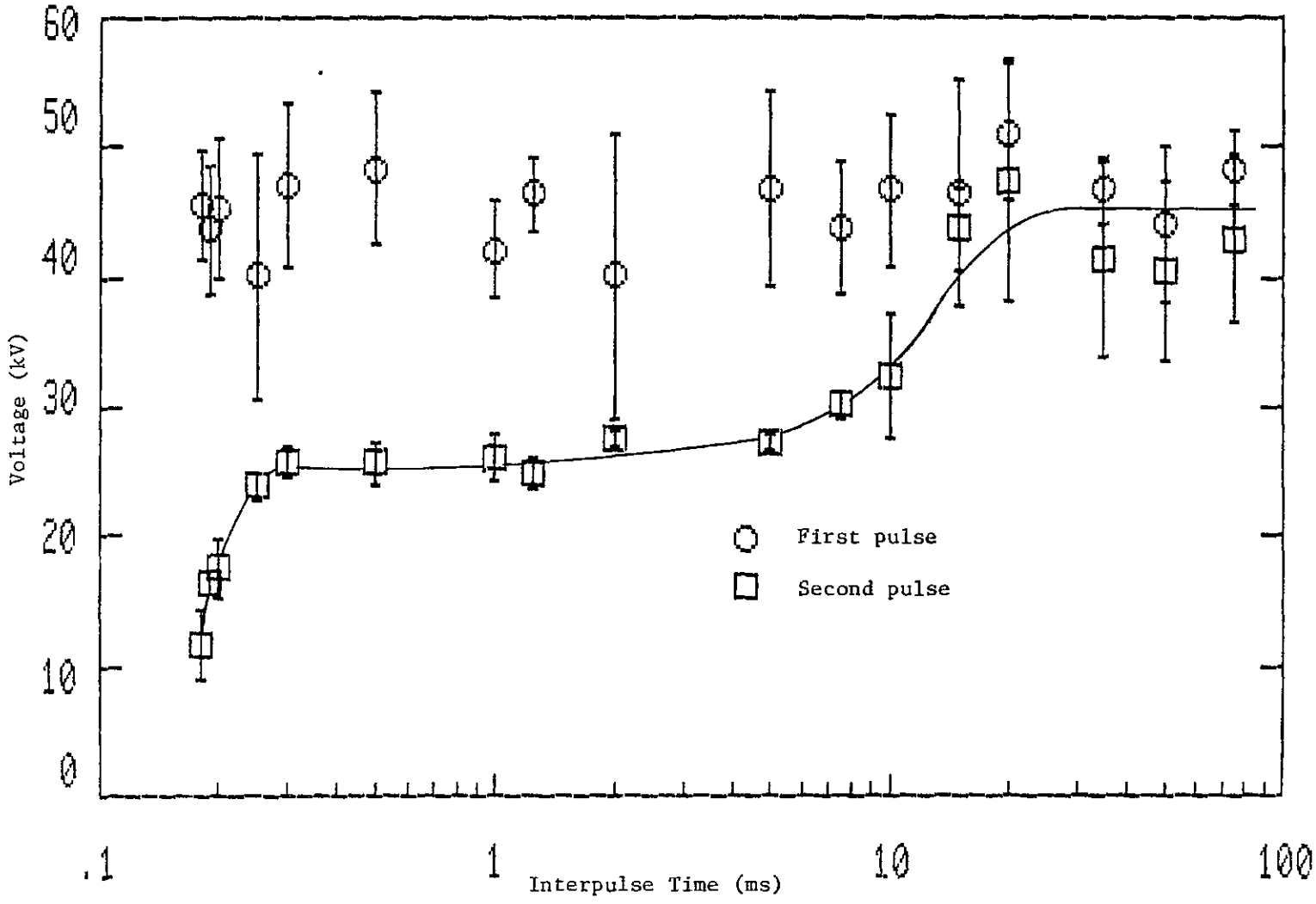

Fig. V-7 Gas flow recovery of the nipple-rod electrodes without preionization, U = 225 m/s (Mach 0.62), d = 1.0 cm, air, p = -1.7 psig, Spacer #4, p_{stag} = 20 psig, valve 90° open.

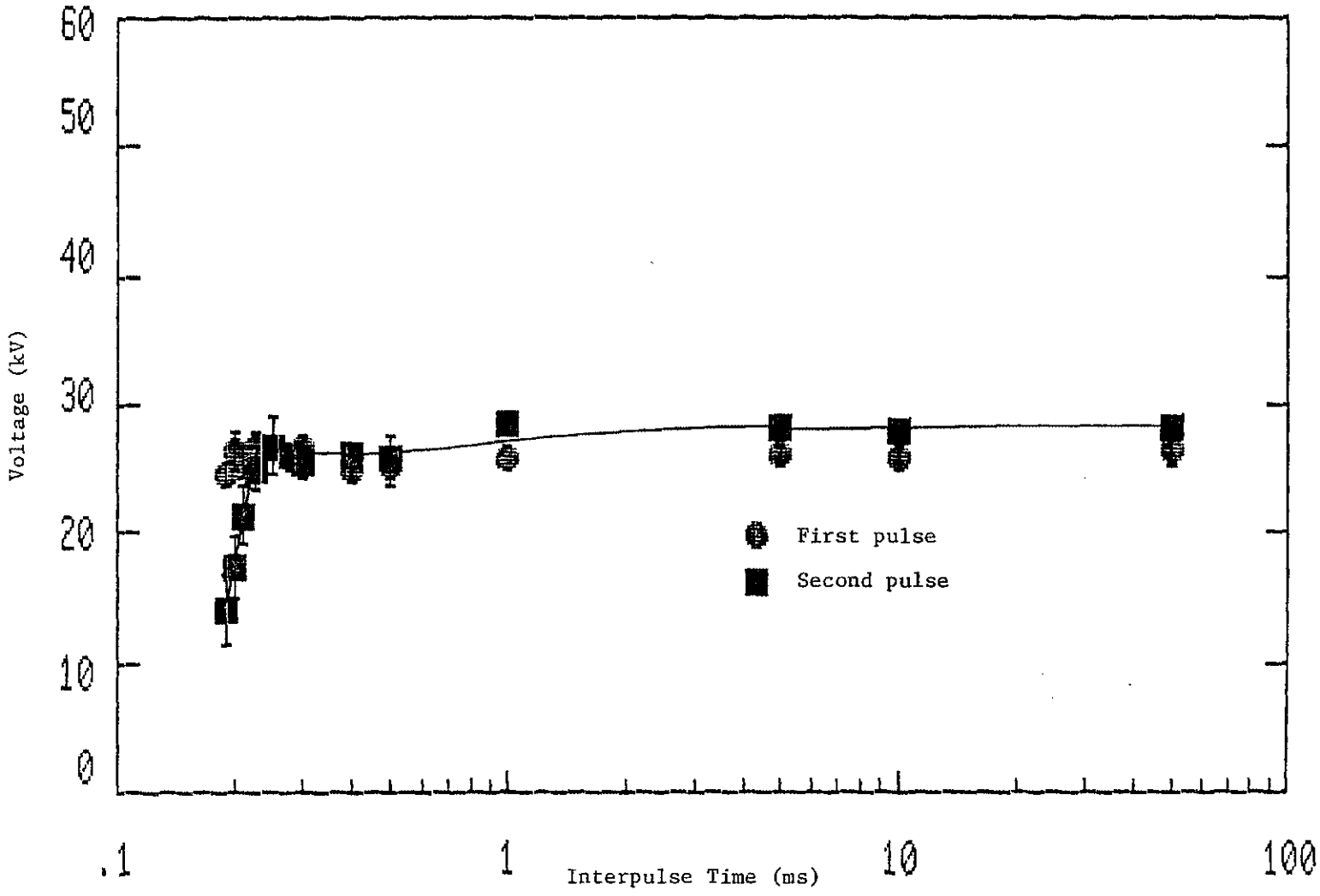

Fig. V-8 Gas-flow recovery of the nipple-rod electrodes with preionization, U = 225 m/s, d = 1.0 cm, air p = -1.7 psig, Spacer #4, p_{stag} = 20 psig, valve 90° open.

of the gap without external preionization. As the velocity increases, the time to initial recovery decreases from approximately 2 ms to 300 μs, an order of magnitude improvement over the static recovery case. The time to final recovery also decreases from 80 ms to approximately 15 ms.

The level of the plateaus have excellent correlation with the static breakdown voltages of irradiated gaps under similar conditions of pressure and gap spacing. The statistically delayed data for the first pulse have magnitudes somewhat different from the magnitudes previously given; however, the variation of the statistical delay under differing conditions of electrode roughness and gas purity does not allow good repeatability. Nevertheless, the characteristic scatter and enhanced overvoltage of statistically delayed breakdown is evident in the first pulse breakdown data and the second pulse breakdown data after final recovery.

Figures V-4, V-6, and V-8 demonstrate recovery when two-pulse preionization is used. In every case, the first pulse overvoltage is reduced to the level of the plateau, and final recovery is thus precluded. The magnitude of the breakdown voltage on the knee of the curve is not significantly affected by this preionization, and the standard deviation is only slightly reduced, indicating that the source of the scatter is not statistical delay, but turbulent conditions.

The final set of recovery data was obtained for a gap spacing of 1.5 cm, a velocity of 360 m/s (Mach 1.0), and a pressure of 10 psig. The data points are presented in Figs. V-9 and V-10. The acquisition of this data was difficult because the rapid depletion of the wind tunnel's storage tanks caused by the high gas velocity made variations

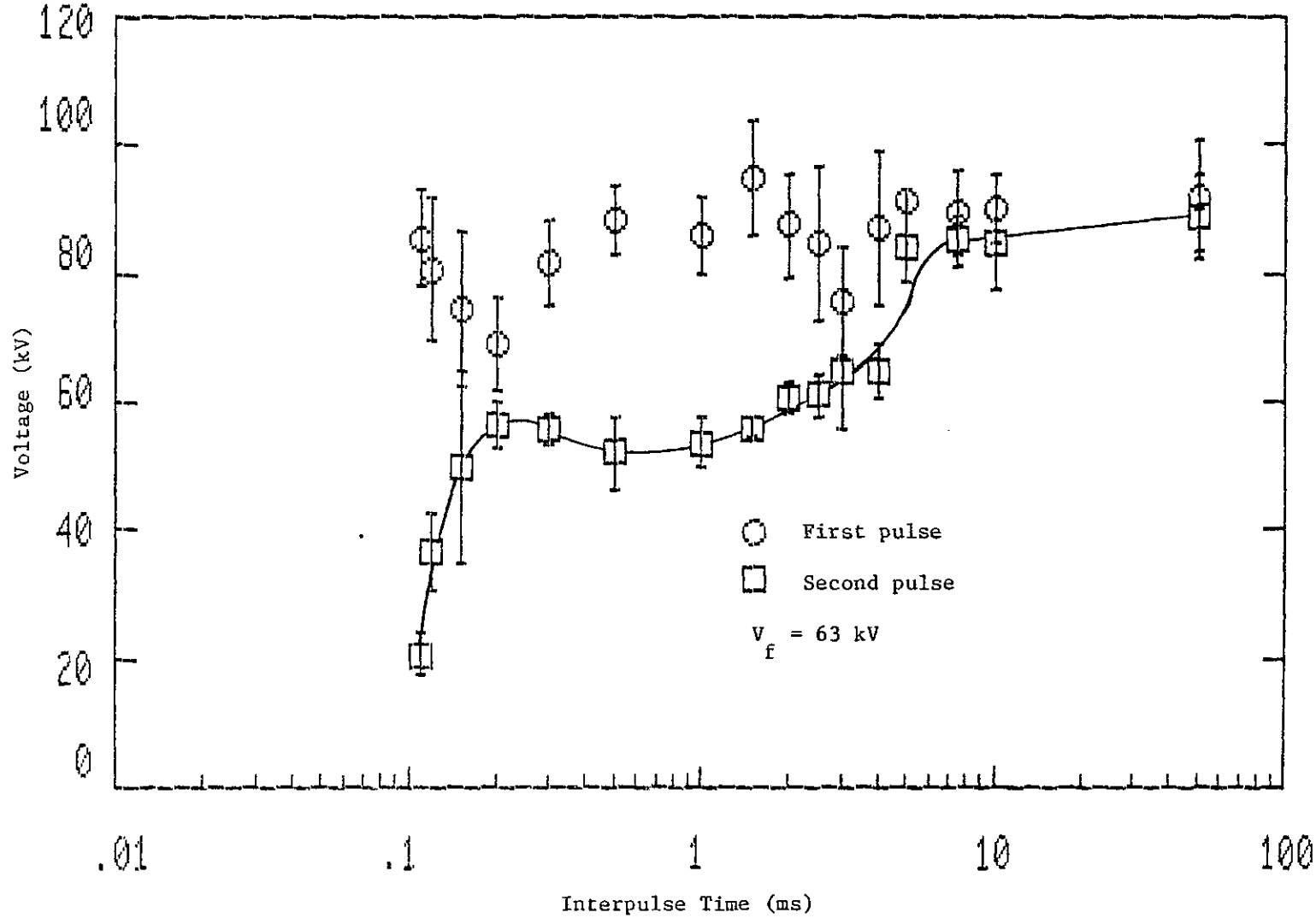

Fig. V-9 Gas-flow recovery of the nipple-rod electrodes without preionization, U = 360 m/s (Mach 1.0), d = 1.5 cm, air, p = 10 psig, Spacer #8, p_{stag} = 45 psig, valve 90° open.

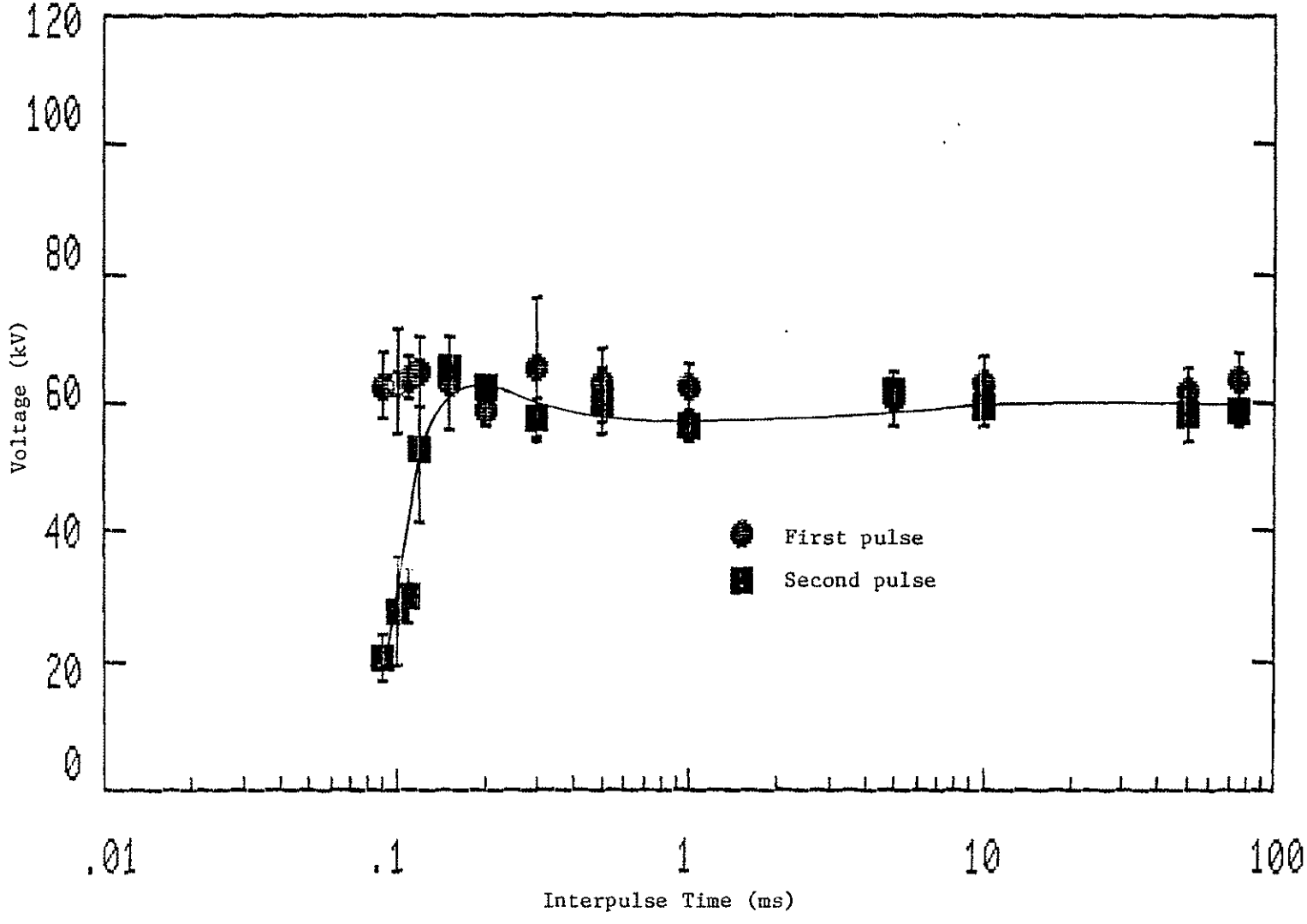

Fig. V-10 Gas-flow recovery of the nipple-rod electrodes with preionization, U = 360 m/s, d = 1.5 cm, air, p = 10 psig, Spacer #8, p_{stag} = 45 psig, valve 90° open.

in pressure and velocity unavoidable. Each data point for this set represents five pulses, and this small sample combined with the experimental error makes the calculated standard deviations unreliable. However, the magnitudes are not as suspect because the averaging process tends to eliminate the experimental fluctuations.

The trends exhibited by all previous results are mirrored in Fig. V-9 as well. Again, the plateau coincides with the pulse-charged breakdown voltage obtained with preionization and final recovery causes the second pulse to return to the statistically delayed regime. This final recovery now occurs at an interpulse time of approximately 5 ms.

Figure V-10 demonstrates that final recovery is again precluded by application of appropriate UV illumination before both pulses. The knee corresponds to 100% recovery of the gap's breakdown strength, which occurs almost in a step fashion as 100 μs is exceeded. Such impressive recovery represents more than an order-of-magnitude improvement as compared to static recovery. The steepness of the slope at the knee is a direct consequence of the high speed clearing of the arc debris.

Without external preionization the characteristic two-stage recovery described in Chapter III has now been shown to exist over a wide range of velocities and pressures. A clue to the explanation for this recovery phenomenon can be found in the velocity dependence of both the initial and final recovery times. This dependence will be considered further in the next chapter.

CHAPTER VI

ANALYSIS OF RECOVERY RESULTS

The results of Chapter V clearly demonstrate the velocity dependence of both initial and final recovery. In this chapter, an attempt is made to reconcile the velocity dependence of recovery with the model described in Chapter III through the use of a simplified mathematical analysis. This analysis is not a substitute for rigorous theoretical calculations; however, it may shed light on the substance of this phenomenon and could point the way to more thorough work later. Particular attention will be devoted to the effects of gas flow on the timing and slope of the recovery curve knee as well as the effects of gas-flow induced electrode cooling and clearing on the time to final recovery.

Initial Recovery

Initial recovery in a gas-blown spark gap occurs when the hot gas created by the arc (arc debris) is convected sufficiently far downstream that the path requiring the least breakdown voltage is once again directly between the electrodes. This description, along with suitable simplifying assumptions, leads to the clearing factor concept previously described. The clearing factor, which is defined in Chapter III as

$$CF = U \cdot \tau/(r+d) \quad , \qquad \text{(VI-1)}$$

implies that the arc debris moves downstream in a homogeneous mass at a uniform velocity and that the maximum distance which the arc will travel to discharge through this debris is a constant for a given spark gap geometry. Clearly this assumption is valid only in the most extreme case of non-turbulent flow and then only when the slower-moving boundary layers are insignificant. Nevertheless, the ability of a properly defined clearing factor to predict recovery times was shown by Molen and Kuhlman [1] and will be further substantiated here.

Equation (VI-1) can be written in the form of a straight line by using logarithms such that

$$\log \tau = \log [CF \cdot (r+d)] - \log U \quad . \qquad \text{(VI-2)}$$

The time to initial recovery has been estimated from the gas flow data presented in Chapter V and is displayed on a log-log scale versus velocity in Fig. VI-1. A linear curve fit has been made to the data and is indicated on the graph as a straight line. The slope of the line is -0.82, which is not an unreasonable deviation from the inverse proportionality implied by Eq. (VI-2). The value of CF is found from the y-intercept to be about 1.6, which is roughly equivalent to the data in Ref. [2].

Further information may be obtained by analysis of the slope of the recovery knee. It can be seen from the recovery curves in Chapter V that the slope of the knee becomes progressively steeper as the velocity increases. This is a natural consequence of the model of gas flow recovery as presented because the rate at which the spark gap

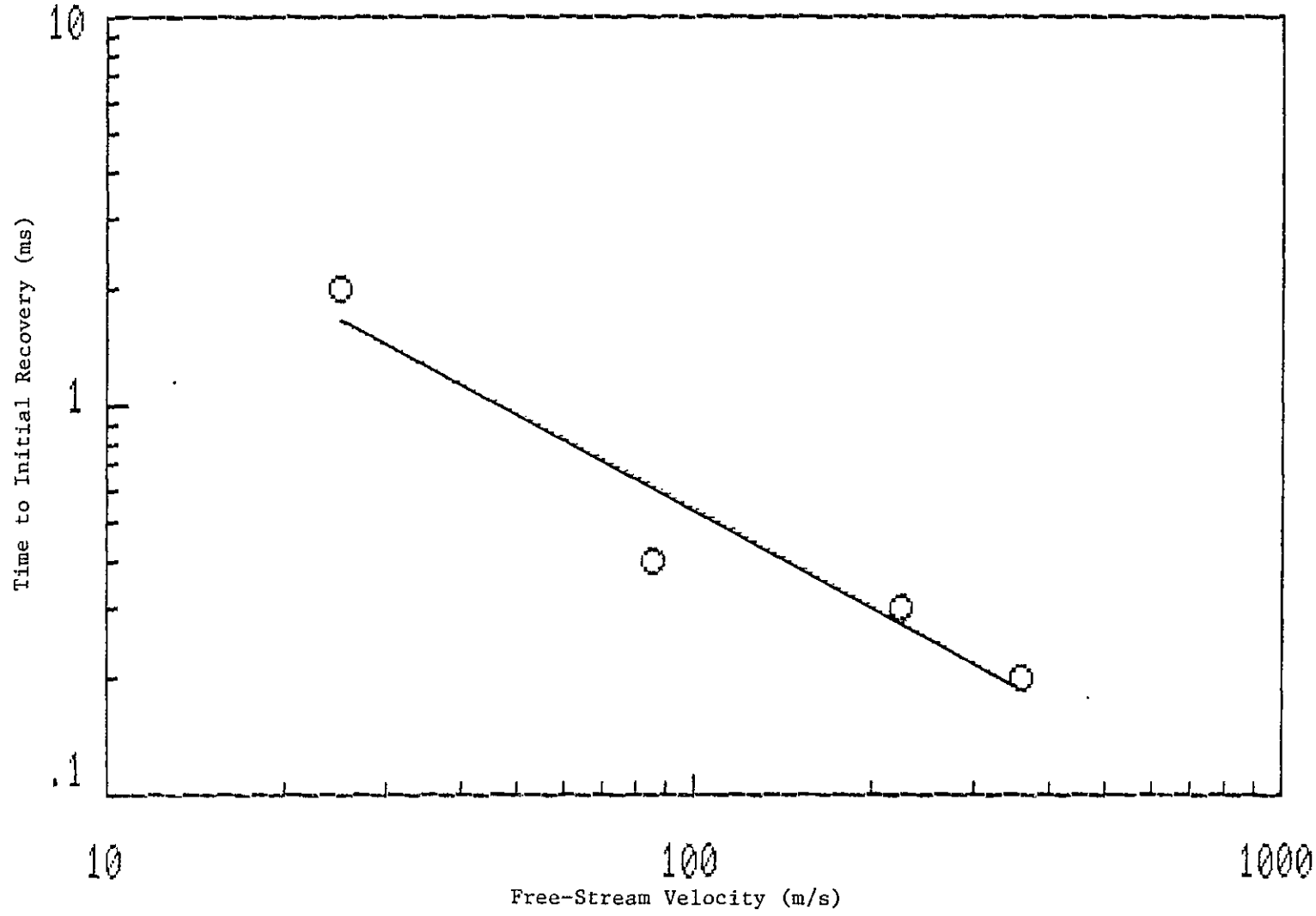

Fig. VI-1 Initial recovery versus free-stream gas velocity. The symbols are experimental data while the line is a least-squares fit.

recovers is dependent on the rate at which the path length is increasing. An illustration of this point is provided in the following simplified model.

The breakdown strength of a spark gap during initial recovery can be characterized as the product of two functions, one dependent on the gas density, N, and the other dependent on the breakdown path length, s. The breakdown voltage is expressed as this product plus a constant such that

$$V_{bk} = f(N) \cdot g(s) + V_o \quad . \qquad \text{(VI-3)}$$

A static spark gap is controlled by the thermal recovery of the gas density while the path length remains constant, thus f(N) is an implicit function of time and g(s) is a constant. On the other hand, the idealized view of gas flow required for the clearing factor calculations implies that the gas density of the arc debris changes little during the short time required for recovery, but the path length increases considerably, thus f(N) is now a constant and g(s) becomes an implicit function of time. It should be noted that for very low velocities or turbulent flow, both functions are time dependent.

The path length is derived from the model shown in Fig. VI-2 in which s is a rectangular path (an approximation of the "C" shape observed in schlieren photographs) that projects downstream from the electrodes and then across the gap through the upstream edge of the arc debris. Thus the path length is $s = 2U\ t + d$, assuming the debris is moving at the free-stream velocity. In such a case it can be shown that the derivative of the breakdown voltage is given by

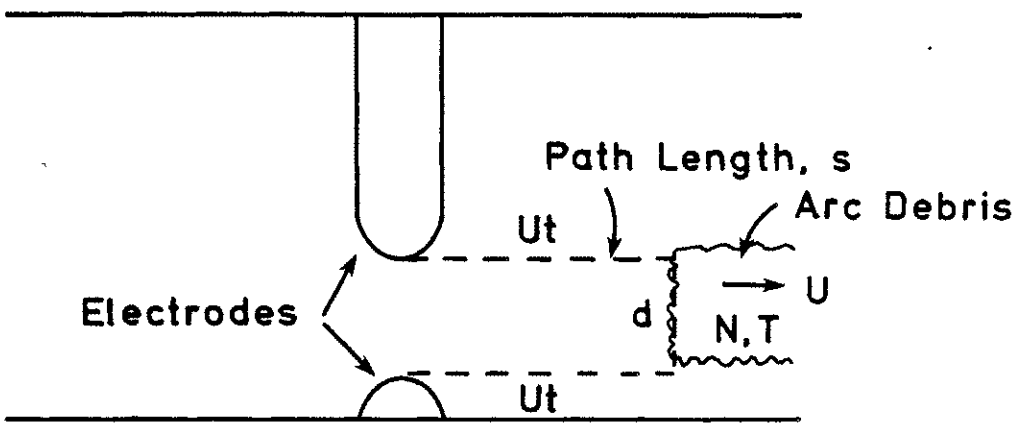

Fig. VI-2 Arc debris clearing model where s is approximated as a rectangular path.

$$dV_{bk}/dt = 2U\ f(N)\ [\partial g(s)/\partial s] \quad . \qquad \text{(VI-4)}$$

Equation (VI-4) illustrates the velocity dependence of the recovery knee slope. An expression for g(s) is obtainable empirically; however, little benefit is expected from such an exercise.

Final Recovery

The time to final recovery also exhibits a marked velocity dependence. It was noted in Chapter III that the production of electrons can be attributed to either a process at the electrodes (thermionic emission) or in the boundary layer near the electrodes (impurity trapping). Both processes can, in principle, be velocity dependent; therefore, two simple calculations have been made and compared with experimental data so as to identify the most likely source of these electrons.

In order to test the thermionic emission hypothesis, a heat transfer calculation was made with the specific goal of calculating the velocity dependence in the temperature decay of the cathode spot region. To do this, the electrode conditions were simplified to allow an analytical expression for the temperature decay. The model assumes that the cathode is a flat plate with a steady stream of gas flow. The plate is heated instantaneously at one spot (point source) and is then cooled by conduction into the electrode and by convection to the moving gas (see Fig. VI-3). The effects of phase changes at the electrodes and flow perturbations have been neglected.

In a simple system such as this an analytical expression can be readily found. Carslaw and Jaeger [34] provide the following Green's

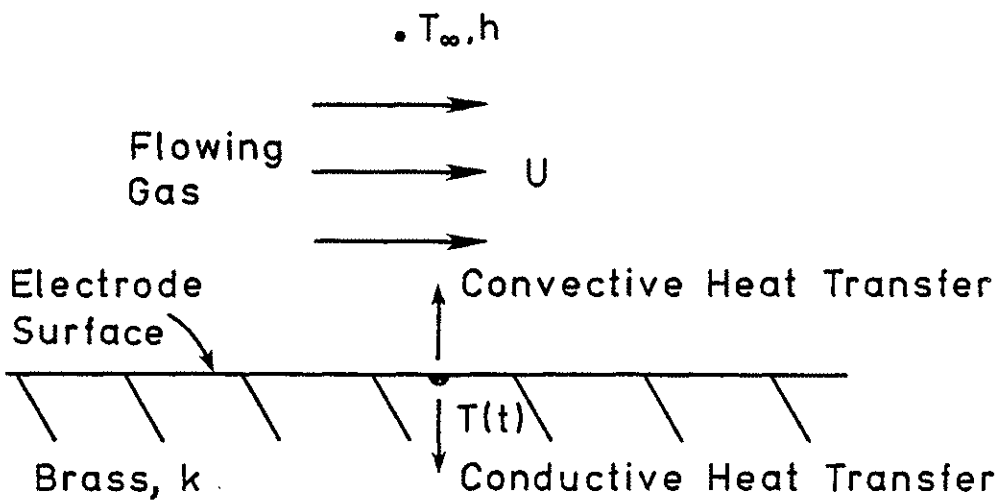

Fig. VI-3 Simplified model of electrode cooling after arc extinction and initial recovery.

function solution for a semi-infinite slab heated initially by a point source:

$$T^* = \frac{1}{4(\pi\kappa t)^{3/2}} - \frac{1}{4\pi\kappa t}\,\mathrm{erfc}[(h/k)\sqrt{\kappa t}]\,\exp[(h/k)^2\kappa t] \quad . \quad \text{(VI-5)}$$

The variable T^* is the temperature per unit volume, κ is the diffusivity of the electrode material (brass), h is the convection coefficient, k is the conduction coefficient of brass, and t is time.

The convection coefficient is a sensitive function of velocity and can be difficult to calculate. Semi-empirical formulae are available [35] for calculating h that are reasonably accurate over the range of velocities used here. Unfortunately, no significant change of the temperature history was found with increasing flow velocity over the time interval of interest for the range of values calculated for h. This result suggests that electrode cooling is dominated by conduction through the solid, even at the highest velocities obtained in the tunnel. While the shortcomings of this calculation are evident (e.g., simplified geometry, neglect of phase changes), the absence of even a trend casts doubt on the thermionic mechanism.

The second mechanism can be approached by considering a boundary layer clearing factor that describes the velocity dependence of final recovery in terms of boundary layer volume replacement. One approach to an analysis begins with the same geometry as that used in the above thermal calculations. Figure VI-4 presents the boundary layer model to be used. The electrode is once again a flat plate and, as a first order approximation, the "no-slip" boundary layer is considered to be

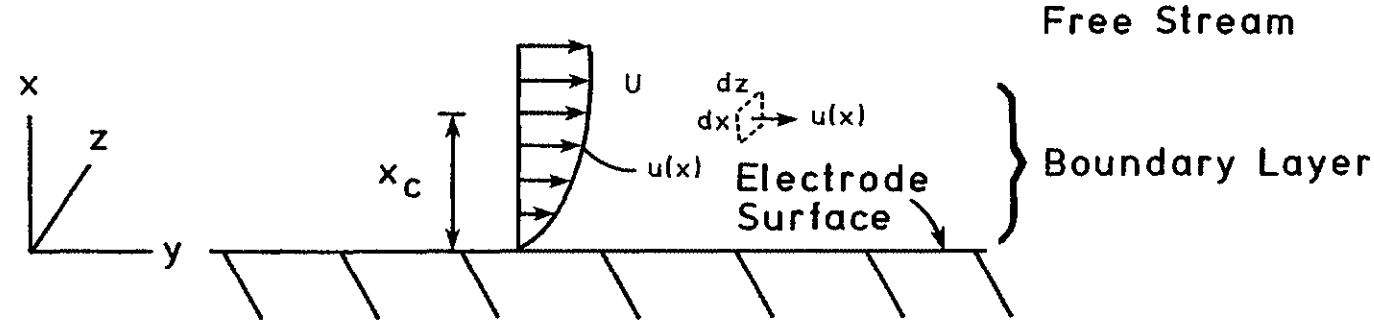

Fig. VI-4 One-dimensional boundary layer model used for the boundary layer clearing factor calculation.

one-dimensional. Near the surface, the local velocity assumes some velocity profile, u(x). The differential volume flow rate is written in terms of a differential area moving at the specified velocity as

$$d\bar{v} = u(x)\ dA = u(x)\ dx\ dz \quad , \tag{VI-6}$$

and the volume flow rate is found by integrating over the width w and thickness x_c of the boundary layer such that

$$\bar{v} = \int_0^{x_c}\int_0^{w} u(x)\ dx\ dz \quad . \tag{VI-7}$$

A Reynolds number calculation indicates that laminar flow can be expected over the velocity range used here. This, coupled with a fundamental interest in only a portion of the boundary layer near the cathode (rather than a complete boundary layer analysis), implies that the velocity profile can be treated in one-dimension as being proportional to x raised to a power. For an order of magnitude calculation, a parabolic profile given by

$$u(x) = \eta x^2 \tag{VI-8}$$

is assumed, where η is a proportionality constant. Completing the integration and using the boundary condition $u(x_c) = U = \eta\ x_c^2$ (U is the free-stream velocity) leads to an expression for the volume flow rate as

$$\bar{v} = w\ U\ x_c/3 \quad . \tag{VI-9}$$

If the boundary layer volume is given by $L \cdot w \cdot x_c$, where L is the characteristic length of the plate, then the average time required to purge the equivalent of one boundary layer volume is given by

$$t_p = v/\bar{v} = 3L/U \quad . \tag{VI-10}$$

Equation (VI-10) can be used to normalize the final recovery time, t_r. The normalized time, $t^* = t_r/t_p$, is written as

$$t^* = U \cdot t_r/3L \quad . \tag{VI-11}$$

By analogy to the relation associated with initial recovery, Eq. (VI-11) can be interpreted as a boundary layer clearing factor. If the time to final recovery is indeed associated with the clearing of impurities from the boundary layer, then Eq. (VI-11) suggests that t_r is inversely proportional to velocity. It should be noted that a change in the exponent of the velocity profile changes the constant in Eq. (VI-11), but not the inverse relationship with velocity.

The recovery curves in Chapter V provide data on the velocity dependence of t_r. Unfortunately, the scatter of the breakdown voltage data in the statistically delayed region precludes exact measurement of t_r; however, a related time constant proportional to t_r can be identified. It is here taken as the time required to recover 50% of the overvoltage due to statistical delay. This value is more easily determined because the transition region above the plateau is fairly well defined.

Figure VI-5 is a log-log plot of 50% recovery versus free-stream velocity. The symbols, which represent experimental data, clearly demonstrate a linear trend; therefore, a linear least squares fit of the data has been made resulting in the line indicated on the graph. The calculated slope of this line is -0.98, which gives strong support to a 1/U relationship between final recovery and velocity. If a parabolic profile is assumed, then the clearing factor, t^*, is calculated from the y-intercept to be 55. This large clearing factor can be shown to be consistent with the boundary layer clearing model if it is assumed that only a thin layer of impurities very near the cathode is responsible for the reduction of the statistical delay, a hypothesis clearly compatible with breakdown physics.

Gas Blown vs. Static Recovery

In this analysis, only recovery with gas flow has been discussed. However, the recovery characteristics of static gaps, both initial and final, are clearly similar. In the case of initial recovery, different recovery processes produce similar results. For example, in a gas-blown spark gap the sparking potential increases when the path length between the electrodes and the low-density arc debris increases. For a static gap, the sparking potential increases as the gas density in the vicinity of the electrodes is increased by cooling. A transition between the two processes occurs when the free-stream velocity balances the turbulent spreading velocity of the arc debris. Such a transition is confirmed by the experimental observation that gas purging below a certain velocity threshold does not significantly

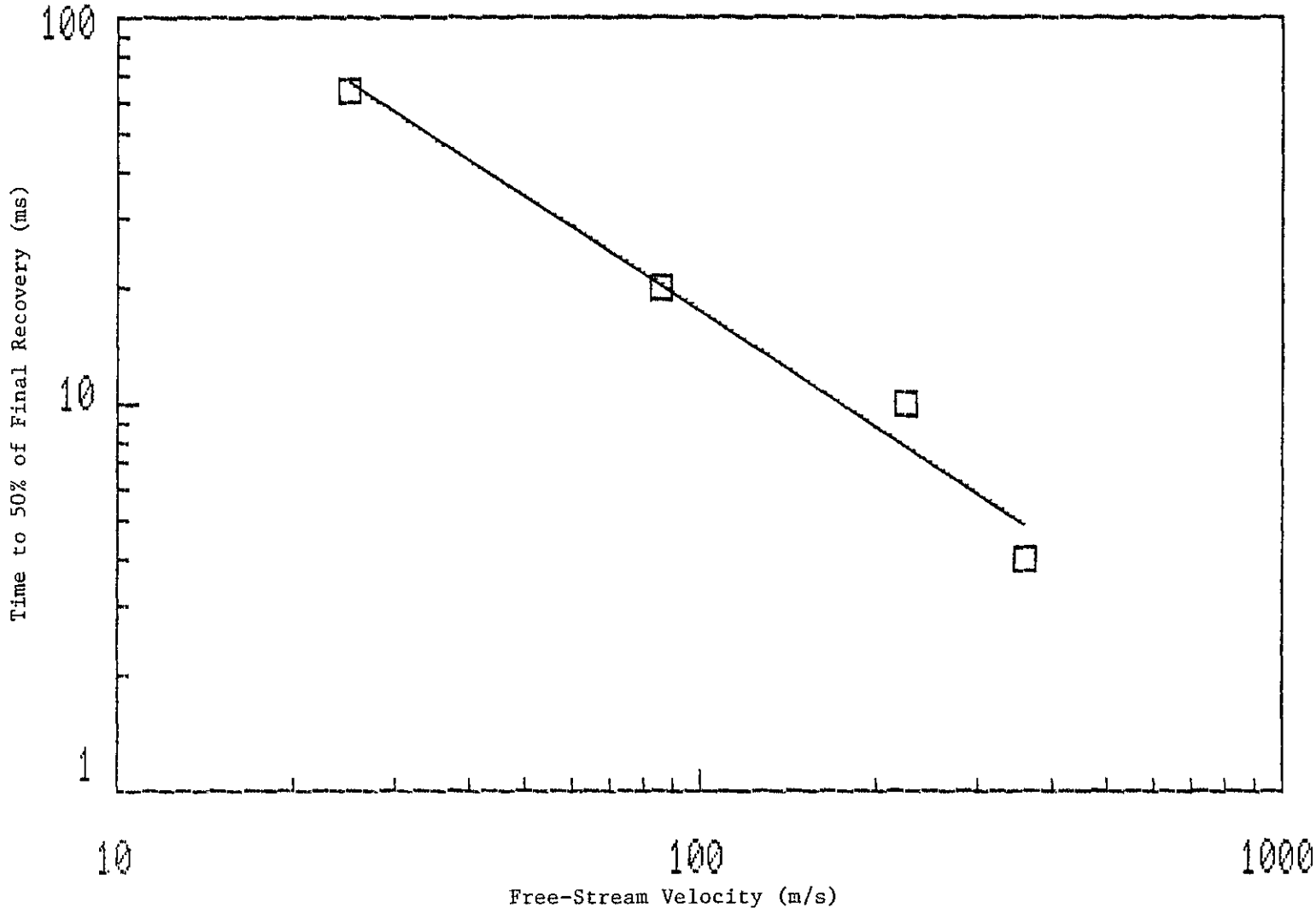

Fig. VI-5 Final recovery versus free-stream gas velocity. The symbols are experimental data while the line is a least-squares fit.

improve spark gap recovery [36]. Thus, turbulent diffusion will dominate the recovery process until a critical gas velocity is exceeded [26].

CHAPTER VII

CONCLUSIONS

The genesis for this work was the need to explain the plateau observed in the recovery curves of pulse-charged gas flow switches. This has been done by correlating the breakdown characteristics of the spark gap with its recovery characteristics under various conditions of static and gas flow operation. As a result, a two-stage recovery model has been proposed that fits the experimental observations within the established framework of breakdown physics.

The conclusions that result from this work are primarily based on correlations between different observed phenomena. The breakdown characteristics of the spark gaps studied here have been explained in context with generally accepted observations made by others. For example, the geometry and pressure dependence of the dc breakdown strength of the non-uniform spark gaps used here was successfully interpreted by empirical equations developed by C. Martin. Then, the pulse-charged breakdown characteristics were derived by considering the voltage increase across a spark gap during the pre-breakdown formative and statistical delays.

The curious recovery curves generated in two-pulse recovery experiments were found to be closely correlated with the breakdown characteristics previously described. Initial recovery to the plateau

is linked to the recovery of the pulse-charged breakdown strength of a preionized spark gap, while final recovery returns the spark gap to the full overvoltage characterized by a statistically delayed gap. The substantial difference in the time required to obtain these two distinct levels adequately explains the anomalous plateau. In addition, the mechanisms that are responsible for these observations have been discussed and simple models have been supported by experiment.

This study has integrated the above observations and models into an overall model of spark gap recovery that is briefly summarized here. Initial recovery in high pressure spark gaps is known to be controlled by the stabilization in gas density caused by either cooling, as in static gaps, or replacement, as in gas-blown gaps. Since breakdown in the gap is a bulk process, small deposits of residual ionization tend to serve as preionization for the next pulse. This small residual electron density, whether continually produced by the cooling cathode spot or by a thin layer of easily ionized impurities trapped in a boundary layer, spoils the large overvoltage attributed to statistical delay. This fact is impressively demonstrated by the 100% recovery of the gas flow switch attained at a repetition rate of 10 kHz when a small amount of photoionization was introduced before both the first and second pulses. The observed plateau clearly demonstrates that these electron sources require a substantially greater amount of time to decay than that required to obtain initial recovery, resulting in the two separate transitions observed.

The ability to investigate the velocity dependence of final recovery has provided important clues to the most probable source of these free electrons. It has been shown that the amount of time

required to obtain final recovery is inversely proportional to gas velocity. How this relates to possible electron emission mechanisms was the subject of two simple calculations. The first was a heat transfer analysis that did not predict the proper dependence, while a rough estimate of boundary layer effects was more successful. This result implies that a gas process near the electrodes and not a bulk process dominates final recovery. More detailed measurements of temperature and flow parameters, coupled with more detailed calculations, are necessary to resolve this question.

Specifically, further recommended work is as follows. First, a suspected oversimplification in the geometry used for the heat transfer calculations was made. In place of a semi-infinite flat plate, a finite cylinder would be more appropriate. In addition, experimental measurements of localized temperature distributions would be very helpful in assessing the effect of velocity on the electrode temperature history. However, the size of the electrodes and the good conduction properties of brass suggest that electrode cooling is, in all probability, conduction dominated.

In order to understand better the transition between the "good-gap" regime and the "bad-gap" regime (the plateau and the statistically delayed region), a quantitative model should be developed to unify the effects of electrode surface roughness, pressure, field enhancement, and impurities on the statistical delay. The importance of such work to practical switch development cannot be overemphasized, as evidenced by the interest shown for such work at universities and national laboratories over the past few years. The fact that a statistically

unreliable switch can be made deterministic merely by increasing the repetition rate is truly an interesting concept.

Finally, improved modeling of initial recovery will allow research data on gas flow switches to be scaled to the needs of applications. It is not recommended that the clearing factor model be relied on for accurate assessments of the performance of large-scale switches. Instead, a model of gas flow recovery should be developed that includes the spatial dependence of both the electric field and the arc debris gas density. With a proper investigation, it should be possible to optimize electrode design so as to reduce the limitations imposed by surface tracking and turbulent wakes. Such optimization may allow initial recovery to be a stronger function of velocity, rather than the mere inverse proportionality provided by the clearing factor model.

LIST OF REFERENCES

[1] D. M. Barrett, "A 250-kV Two-Pulse Modulator for the Gas Flow Switch Test Facility," Master Thesis, Old Dominion University, Norfolk, VA, 1984.

[2] G. M. Molen and J. M. Kuhlman, "Investigation of Gas Flow Switches," Final Report on NSWC contract N60921-81-C-A221, Old Dominion University Research Foundation, Norfolk, VA 1985.

[3] A. H. Guenther and M. Kristiansen, "Guest Editorial," IEEE Trans. Plasma Sci., Vol. PS-10, p. 217, 1982.

[4] J. D. Cobine, Gaseous Conductors. New York: Dover, 1958.

[5] G. M. Molen and H. J. Carper, (ed.), "Thermal and Gas Dynamic Effects," group report, Proc. of the DoD Workshop on Repetitive, High Power, Gas Spark Gaps, pp. 217-262, Jan. 1983, Durango, CO.

[6] T. R. Burkes, J. P. Craig, M. O. Hagler, M. Kristiansen, and W. M. Portnoy, "A Review of High-Power Switch Technology," IEEE Trans. Electron Dev., Vol. ED-26, pp. 1401-1411, 1979.

[7] J. M. Kuhlman, "Survey of Gas Flow and Heat Transfer Effects on Performance of Gas Spark Gaps," Proceedings of the DoD Workshop on Repetitive, High Power, Gas Spark Gaps, pp. 85-153, Jan. 1983, Durango, CO.

[8] E. E. Kunhardt and L. H. Luessen, (ed.), Electrical Breakdown and Discharges in Gases, NATO ASI series Vol. 89a. New York: Plenum Press, 1983, pp. 1-71.

[9] J. M. Meek and J. D. Craggs, (ed.), Electrical Breakdown in Gases. New York: Wiley, 1978.

[10] E. Nasser, Fundamentals of Gaseous Ionization and Plasma Electronics. New York: Wiley, 1971, pp. 264-268.

[11] E. E. Kunhardt, "Electrical Breakdown of Gases: The Prebreakdown Stage," IEEE Trans. Plasma Sci., Vol. PS-8, pp. 130-138, 1980.

[12] E. E. Kunhardt and W. W. Byszewski, "Development of Overvoltage Breakdown at High Gas Pressure," Phys. Rev. A, Vol. 21, pp. 2069-2077, 1980.

[13] W. J. Sarjeant, (ed.), "High Voltage/Pulse Power Technology," Los Alamos Scientific Laboratory, Los Alamos, NM, Lecture Six, p. 11, Oct. 1980.

[14] G. Carrara and L. Thione, "Switching Surge Strength Of Large Air Gaps: A Physical Approach," IEEE Trans. Power Appar. Sys., Vol. PAS-95, pp. 512-524, 1976.

[15] T. H. Martin, "Pulse Charged Gas Breakdown," Proc. Fifth IEEE Pulsed Power Conf., IEEE Pub. No. 85C2121-2, pp. 74-83, 1985.

[16] G. A. Farrall and J. D. Cobine, "Recovery Strength Measurements in Arcs from Atmospheric Pressure to Vacuum," IEEE Trans. Power Apparatus System, Vol. PAS-86, pp. 927-932, 1967.

[17] H. Edels, D. Whittaker, K. G. Evans, and A. B. Shaw, "Experiments and Theory on Arc Reignition by Spark Breakdown," Proc. IEEE, Vol. 112, pp. 2343-2352, 1965.

[18] J. M. Kuhlman and G. M. Molen, "Performance of High-Power Gas-Flow Spark Gaps," Proc. AIAA 23rd Aerospace Sciences Meeting, Reno, NV, 1985.

[19] G. M. Molen, E. G. Ruf, J. M. Kuhlman, and J. S. Bernardes, "Gas-Flow Switch Recovery Experiments," Proc. Fourth IEEE Pulsed Power Conf., IEEE Pub. No. 83CH1908-3, pp. 166-169, Albuquerque, NM, June 1983.

[20] S. Moran and S. Hairfield, "High Pressure Spark Gap Recovery After Overvolted Breakdown," Proc. Fifth IEEE Pulse Power Conf., IEEE Pub. No. 85C2121-2, pp. 473-476, Arlington, VA, June 1985.

[21] G. M. Molen, J. M. Kuhlman, S. H. Nam, and E. G. Ruf, "A 250-kV Gas-Flow Spark Gap," Proc. Fifth IEEE Pulsed Power Conf., IEEE Pub. No. 85C2121-2, pp. 465-468, Arlington, VA, June 1985.

[22] D. C. Rabe, "Supersonic Spark Gap Switch," U. S. Air Force invention disclosure AD-D002 626, 1976.

[23] A. Faltens, L. L. Reginato, R. H. A. Chesterman, E. G. Cook, T. Yokota, and W. Dexter, "High Repetition Rate Burst-Mode Spark Gap," IEEE Trans. Electron Dev., ED-26, pp. 1411-1413, Oct. 1979.

[24] R. Litte and R. Limpaecher, "An Application of a High Energy Spark Gap in a Repetitive Mode," Proc. of the Fifth IEEE Pulsed Power Conf., IEEE Pub. No. 85C2121-2, pp. 477-480, Arlington, VA, June 1985.

[25] "Flow Technology for High PRF Rail Gap Switches," Final Report to Los Alamos Scientific Laboratory, by Spectra Technology (Formerly Mathematical Sciences Northwest), Bellevue, WA, 1982.

[26] J. M. Kuhlman, G. M. Molen, S. Srinivasan, S. H. Nam, and S. N. Tiwari, "Arc-Generated Flow Phenomena in Repetitively Pulsed Gas-Flow Spark Gaps," IEEE Trans. Plasma Sci., Vol. PS-14, pp. 228-233, June 1986.

[27] J. C. Martin, "DC Breakdown Voltages of Non-Uniform Gaps in Air," Dielectric Strength Notes, AWRE, Aldermaston, England, Note 16, June 1970.

[28] J. C. Martin, "Nanosecond Pulse Techniques," AWRE Rept. No. SSWA/JCM/704/49, Aldermaston, England, April 1970.

[29] R. V. Babcock, I. Liberman, and W. D. Partlow, "Volume Ultraviolet Preionization from Bare Sparks," IEEE J. Quantum Electron., Vol. QE-12, pp. 29-34, Jan. 1976.

[30] A. L. Donaldson, D. Garcia, M. Kristiansen, and A. Watson, "A Gap Distance Threshold in Electrode Erosion in High Current, High Energy Spark Gaps," Proc. of the Seventeenth Power Modulator Symposium, Seattle, WA, June 1986.

[31] E. G. Cook and L. L. Reginato, "Off-Resonant Transformer Charging for 250-kV Water Blumlein," IEEE Trans. Electron Dev., Vol. ED-26, pp. 1512-1517, Oct. 1979.

[32] D. M. Barrett, H. C. Kirbie, and G. M. Molen, "A 250-kV, 10-kHz Two-Pulse Modulator," Proc. of the Fourth IEEE Pulsed Power Conf., IEEE Pub. No. 83CH1908-3, pp. 255-258, Albuquerque, NM, June 1983.

[33] N. Wainfan, W. C. Walker, and G. L. Weissler, "Photoionization Cross Sections in O_2, N_2, CO_2, A, H_2O, H_2, and CH_4," Phys. Rev., Vol. 99, pp. 542-549, July 1955.

[34] Carslaw and Jaeger, Conduction of Heat in Solids. London: Oxford University Press, 1959, pp. 370-371.

[35] F. White, Heat Transfer. Reading, MA: Addison-Wesley, 1984, p. 307.

[36] R. J. Pederson, M. A. Borger, and H. J. Carper, "Effects of Flow Velocity and Electrode Divergence Angle on the Performance of a Repetitively Pulsed, Gas-Blown Spark Gap Switch," Proc. IEEE 16th Power Modulator Symp., IEEE Pub. No. 84CH2056-0, pp. 48-53, Washington, D.C., June 1984.